

# **Flight path optimization for noise reduction in the vicinity of airports**

**André Santos de Sousa**

Thesis to obtain the Master of Science Degree in  
**Aerospace Engineering**

Supervisors: Prof. João Manuel Gonçalves de Sousa Oliveira  
Prof. António José Nobre Martins Aguiar

## **Examination Committee**

Chairperson: Prof. Fernando José Parracho Lau  
Supervisor: Prof. João Manuel Gonçalves de Sousa Oliveira  
Members of the Committee: Prof. Pedro da Graça Tavares Alvares Serrão

**June 2015**



## Acknowledgements

This dissertation represents the end of a remarkable and unique journey and the support and courage given by several people were fundamental to the conclusion of my engineering degree.

Firstly, I would like to gratefully acknowledge my advisors, Professor João Oliveira and Professor António Aguiar, for the opportunity of working with them. Since the first day, their continuous support and advice were invaluable for the development and conclusion of this thesis.

I would also like to thank all the support and love given by my family, in particular by my parents, Filomena and António, who raised me the man I am today and who continuously encouraged me to expand my horizons allowing me to pursue my dreams.

It is also important to address my younger brother Pedro, for his unconditional support and for promptly answering my countless requests for advice.

Additionally, and because five years is a long trip, I could not forget the person who accompanied closely this journey, my dear friend Rita. During the last five years, you continuously gave your best, twenty-four-seven, to make my day a better one. Words cannot express my gratitude for your friendship and for making me a better and wiser person.

This appreciation would not be complete if I didn't mention my longtime friends Afonso, Cristina, Miguel, Natacha and Pedro, to whom I acknowledge the tireless friendship, their promptness in helping me through challenging moments and their effusiveness in celebrating my achievements.

Furthermore, and as recent friendships are as important as the longer ones, I would also like to thank my friend Marina for the boost in energy and confidence and for filling my days with her contagious happiness and kindness.

Last but not least, I would like to acknowledge all my friends from the aviation world, in particular my friends António, Carlos, Catarina, Miguel, Nuno and Vítor. Thank you for your incredible support and for your valuable insights during my Masters degree and also for sharing with me your passion for aviation.



## Abstract

In recent years, aviation noise has become a growing concern. Due to an expected increase of commercial air traffic, accompanied by an amplified public environmental awareness, aviation regulators are now required to review existing legislation and demand to both aircraft manufacturers and operators the commitment to noise reduction campaigns in their fields of activity. These policies lead to the development of increasingly accurate noise prediction tools that include more complex sound propagation models and that simultaneously allow real-time computations in an operational environment.

This dissertation presents a model adequate for sound propagation over a flat surface with realistic atmospheric conditions. The model is a hybrid combination of two physics-based sound propagation schemes: the parabolic equation and the ray model.

As the program developed in this thesis is oriented towards aviation noise, a method of defining the aircraft power spectrum was adopted and several empirical correlations were included in order to model source directivity. With this procedure, the hybrid model may represent complex sound sources moving along specified flight paths.

The numerical methods were validated using benchmark test cases created for different meteorological environments. The program was applied to different airport scenarios by resorting to realistic flight parameters and the coherent results obtained confirmed the suitability of the hybrid model to study aircraft noise in the vicinity of airports.

**Keywords:** sound propagation, aviation noise, hybrid model, noise reduction.



## Resumo

Nos últimos anos, o ruído aeronáutico tornou-se uma preocupação crescente. Devido a um esperado crescimento de tráfego comercial, o qual é acompanhado por uma mais abrangente consciência ambiental das populações, é requerido às autoridades aeronáuticas a revisão da legislação vigente e a promoção junto dos fabricantes e das companhias aéreas de ações de minimização de ruído nas respectivas áreas de atividade. Estas políticas resultam no desenvolvimento de ferramentas mais precisas de previsão de ruído, as quais incluem mecanismos de propagação de som mais complexos e que simultaneamente permitem previsões em tempo real em ambientes operacionais.

Esta dissertação apresenta um modelo adequado para a propagação de som sobre uma superfície plana em condições meteorológicas realistas. Este modelo envolve uma combinação de dois esquemas de propagação de som: o método de equações parabólicas e o modelo de raios sonoros.

Como o problema desenvolvido é orientado para o ruído aeronáutico, foi adotado um método de definição do espectro de potência sonora de aeronaves e foram incluídas múltiplas correlações empíricas que modelam a diretividade sonora da fonte. Com este procedimento, o modelo híbrido pode representar fontes sonoras complexas que se movem ao longo de trajetórias específicas.

Os métodos numéricos foram validados utilizando resultados de referência para diferentes condições meteorológicas. O programa foi aplicado a diferentes cenários envolvendo parâmetros de voo realistas e a consistência dos resultados obtidos permite confirmar a adequabilidade do modelo híbrido ao estudo de ruído aeronáutico nas imediações de aeroportos.

**Palavras Chave:** propagação de som, ruído aeronáutico, modelo híbrido, redução de ruído.



# Contents

Acknowledgements .....	i
Abstract.....	iii
Resumo.....	v
Contents.....	vii
List of Figures.....	xi
List of Tables.....	xiii
List of Acronyms and Symbols .....	xv
1 Introduction .....	1
1.1 Motivation .....	1
1.2 Outdoor Sound Propagation.....	1
1.2.1 Atmospheric acoustics.....	1
1.2.2 Geometrical spreading .....	4
1.2.3 Atmospheric absorption.....	4
1.2.4 Ground interaction .....	6
1.2.5 Atmospheric refraction.....	8
1.3 State of the Art in Aviation Noise.....	10
1.3.1 Aviation oriented computational tools.....	10
1.3.2 Numerical propagation models.....	11
1.3.3 Aviation noise metrics.....	14
1.4 Research Objectives and Outline .....	16
2 Green's Function Parabolic Equation Method (GFPE).....	17
2.1 Theoretical Formulation.....	17
2.1.1 Inhomogeneous Helmholtz equation.....	17
2.1.2 Kirchhoff-Helmholtz integral equation.....	18
2.1.3 General Green's function method.....	20
2.1.4 Constant sound speed profile.....	21
2.1.5 Non-constant sound speed profile.....	22
2.2 Numerical Implementation.....	23

2.2.1	Starting field.....	24
2.2.2	Discretization of the Fourier integrals.....	25
2.2.3	Fast Fourier Transform (FFT).....	26
2.2.4	Artificial absorption layer.....	26
2.2.5	Alternate refraction factor.....	27
3	Ray Model.....	29
3.1	Theoretical Formulation.....	29
3.1.1	Snell's Law.....	29
3.1.2	Constant sound speed profile.....	30
3.1.3	Non-constant sound speed profile.....	31
3.1.4	Ground interaction.....	31
3.2	Numerical Implementation.....	32
4	Hybrid Numerical Model.....	35
4.1	Propagation models limitations.....	35
4.1.1	GFPE model.....	35
4.1.2	Two ray model.....	35
4.2	Model combination.....	35
5	Aircraft as a Noise Source.....	37
5.1	Sound Power Spectrum.....	37
5.1.1	Noise Power Distance (NPD) results.....	37
5.1.2	Reverse engineering from NPD values.....	38
5.2	Aircraft Attitude Corrections.....	39
5.2.1	Lateral directivity.....	39
5.2.2	Longitudinal directivity.....	40
6	Program Description.....	41
6.1	User interface.....	41
6.2	Input parameters.....	41
6.2.1	Aircraft parameters.....	42
6.2.2	Airport parameters.....	42
6.2.3	Numerical parameters.....	43
6.2.4	Trajectory parameters.....	44

6.3	Simulation calculations .....	45
6.3.1	Program workflow .....	45
6.3.2	Code performance optimization.....	47
6.4	Output Parameters .....	48
7	Analysis and Results .....	49
7.1	Benchmark test cases .....	49
7.2	Propagation models validation .....	52
7.2.1	GFPE Validation .....	52
7.2.2	Two Ray Model Validation .....	56
7.3	Hybrid model validation .....	58
8	Program application to aircraft trajectories .....	65
8.1	Simulated airport scenario: case studies.....	65
8.1.1	Reference conditions .....	65
8.1.2	Aircraft trajectories.....	66
8.1.3	Simulation results .....	68
8.2	Review of noise abatement procedures .....	75
9	Conclusions and future developments.....	79
10	References .....	81
A.	Benchmark case studies results .....	85
B.	Position of the receivers for the airport case studies.....	89



## List of Figures

Figure 1.1 - Illustration of frequency scales: narrow band, 1/3-octave band and octave band scale. (Salomons, 2001). .....	3
Figure 1.2 - Example of a typical evolution of the absorption coefficient as a function of the source frequency (Salomons, 2001). .....	6
Figure 1.3 - Illustration of reflection of sound waves on a ground surface (Salomons, 2001). .....	7
Figure 1.4 - Direct ray and reflected ray in a downward refracting atmosphere (left) and upward refracting atmosphere (right) (Salomons, 2001). .....	9
Figure 1.5 - Representation of a layered atmosphere for the FFP model (Salomons, 2001). .....	11
Figure 1.6 - Two dimensional numerical grid used in the PE models (Salomons, 2001). .....	12
Figure 1.7 - Representation of the angular limitation of PE schemes (Oliveira, 2012). .....	12
Figure 1.8 - Level time history of a noise event (European Civil Aviation Conference, 2005a). .....	15
Figure 2.1 – Geometry for the two dimensional Kirchhoff-Helmholtz equation (Salomons, 2001). .....	19
Figure 3.1 – Refracted ray from a monopole source to a receiver in the same atmosphere (Salomons, 2001). .....	30
Figure 3.2 – Oblique reflection of a sound wave by a flat ground surface (Salomons, 2001). .....	31
Figure 3.3 – Geometry of the two ray model with a source and receiver above a ground surface (Salomons, 2001). .....	32
Figure 5.1 - Aircraft sound emission coordinates (Butikofer, 2006). .....	39
Figure 5.2 - Directivity functions for departing flights (Butikofer, 2006). .....	40
Figure 7.1 - Transmission loss up to 200 m (left figures) and up to 2 km (right figures) with parameters from test case 1. ....	53
Figure 7.2 - Transmission loss up to 200 m (left figures) and up to 2 km (right figures) with parameters from test case 2. ....	54
Figure 7.3 - Transmission loss up to 200 m (left figures) and up to 2 km (right figures) with parameters from test case 3. ....	55
Figure 7.4 - Relative SPL as a function of range for a receiver height of 50 m. ....	56
Figure 7.5 - Relative SPL as a function of elevation angle for receiver range of 400 m. ....	57
Figure 7.6 - 1/3-octave band spectra of the relative SPL computed with the GFPE method and the two ray model for a homogeneous atmosphere. ....	58
Figure 7.7 - Transmission loss along a line of constant elevation angle for a wave frequency of 10 Hz (top figures), 100 Hz (middle figures) and 1000 Hz (bottom figures) and for a non-refracting atmosphere. ....	60
Figure 7.8 - Transmission loss along a line of constant elevation angle for a wave frequency of 10 Hz (top figures), 100 Hz (middle figures) and 1000 Hz (bottom figures) and for a downward refracting atmosphere. ....	61

Figure 7.9 - Transmission loss along a line of constant elevation angle for a wave frequency of 10 Hz (top figures), 100 Hz (middle figures) and 1000 Hz (bottom figures) and for an upward refracting atmosphere.....	62
Figure 7.10 - Transmission loss as a function of range using the GFPE method, the ray model and the hybrid model, for a homogeneous atmosphere.....	63
Figure 7.11 - Transmission loss as a function of range using the GFPE method, the ray model and the hybrid model, for a downward refracting atmosphere. ....	64
Figure 8.1 - SPL and range time history for the ILS approach simulation. ....	69
Figure 8.2 - Experimental SEL spectrum for the approach simulation (Correia, 2011). ....	70
Figure 8.3 - Numerical SEL spectrum for the approach simulation.....	71
Figure 8.4 - SPL and range time history for the ILS approach simulation in a downward refracting atmosphere (left figure) and in an upward refracting atmosphere (right figure). ....	71
Figure 8.5- SPL and range time history for NADP 1 (left figure) and NADP 2 (right figure) departing procedures.....	73
Figure 8.6 - SPL and engine thrust time history for NADP 1 (left figure) and NADP 2 (right figure) departing procedures.....	73
Figure 8.7 - Altitude (left figure) and engine thrust (right figure) as functions of distance to the start of takeoff roll. ....	75
Figure 8.8 - Noise maps for the departure test cases of section 8.2, representing the aircraft's trajectory (blue line) and the SEL (in dB) contours (black lines). ....	77
Figure A.1 - Transmission loss up to 200 m (left figures) and up to 2 km with parameters from test case 1 (Attenborough et al., 1995). ....	85
Figure A.2 - Transmission loss up to 200 m (left figures) and up to 2 km with parameters from test case 2 (Attenborough et al., 1995). ....	86
Figure A.3 - Transmission loss up to 200 m (left figures) and up to 2 km with parameters from test case 3 (Attenborough et al., 1995). ....	87
Figure B.1 - Position of the receivers for the airport simulations. <b>Google Earth</b> . July 8 <sup>th</sup> , 2012. April 29 <sup>th</sup> 2015.....	89

# List of Tables

Table 1.1 - Effective flow resistivity for different materials, from Embleton et al. (1983) and reproduced by Rosenbaum (2011). ..... 8

Table 2.1 – Values of the parameters *A* and *B* in Equation ( 2.36 ), from Salomons (2001). ..... 24

Table 2.2 – Values of the attenuation factor for an octave band scale (Salomons, 1998). ..... 27

Table 6.1 - Description of the memory usage algorithms implemented in the program ..... 47

Table 7.1 - Atmospheric refraction parameters of the three test cases for the GFPE method validation. .... 49

Table 7.2 - Acoustic parameters for the test cases from Table 7.1..... 50

Table 7.3 - Test conditions for the two ray model validation. .... 50

Table 7.4 - Numerical parameters for the test cases in Table 7.1 and Table 7.3. .... 51

Table 7.5 - Source and receiver conditions for the validation cases of the transition region. .... 52

Table 8.1 - Fuel distribution (in percentage of fuel tank capacity) of the A320 used in the simulated trajectories. .... 65

Table 8.2 - Environmental parameters for the simulated airport scenarios. .... 65

Table 8.3 - Grid parameters for the simulated airport scenarios. .... 66

Table 8.4 - Computation times for the ILS approach and the noise abatement departing trajectories. 68

Table 8.5 - SEL for the ILS approach and the noise abatement departing trajectories. .... 68

Table 8.6 - Maximum SPL and SEL for the ILS approach simulation. .... 70

Table 8.7 - SEL from numerical calculations and experimental measurements for the ILS approach in a homogeneous atmosphere..... 70

Table 8.8- Atmospheric refraction parameters for the ILS approach in refracting conditions. .... 71

Table 8.9 - SEL from numerical calculations and experimental measurements for the ILS approach in refracting conditions. .... 72

Table 8.10 - SEL from numerical calculations for the departing procedures. .... 73

Table 8.11 - SEL (dB) from numerical calculations and experimental measurements for the departing procedure..... 74

Table 8.12 - Maximum SPL (dB) from numerical calculations and experimental measurements for the departing procedure. .... 74

Table 8.13 - Definition of the takeoff stages (in feet AGL) for the NADP published by ICAO (2007b). 75

Table 8.14 - SEL (dB) for the reviewed departing procedures and for each receiver position. .... 78

Table B.1 - Geographic (GPS) positions of the receivers for the airport simulation. .... 89



# List of Acronyms and Symbols

## Mathematical notation

Boldfaced symbols are used for vector, for example  $\mathbf{r} = (x, y, z)$ ,

$\partial_x f = \partial f / \partial x$  is the partial derivative of function  $f$ ,

$\partial_x^2 f = \partial^2 f / \partial x^2$  is the second partial derivative of function  $f$ ,

$\nabla f = (\partial_x f, \partial_y f, \partial_z f)$  is the gradient of a scalar function  $f$ .

## Acronyms

AGL	Above Ground Level
AIP	Aeronautical Information Publication
AMSL	Above Mean Sea Level
ANP	Aircraft Noise and Performance
ANSP	Air Navigation Service Provider
CAA	Civil Aviation Authority
CNPE	Crank-Nicholson Parabolic Equation
CNT	Corrected Net Thrust
ECAC	European Civil Aviation Conference
EPR	Engine Pressure Ratio
DFT	Discrete Fourier Transform
EPNL	Effective Perceived Noise Level
FAA	Federal Aviation Administration
FFP	Fast Field Program
FFT	Fast Fourier Transform
GFPE	Green's Function Parabolic Equation
GPS	Global Positioning System
ICAO	International Civil Aviation Organization
IFR	Instrument Flight Rules
ILS	Instrument Landing System
NADP	Noise Abatement Departure Procedure
NAP	Noise Abatement Procedure
NPD	Noise Power Distance
PE	Parabolic Equation
SAE	Society of Automotive Engineers
SEL	Sound Exposure Level
SID	Standard Instrument Departure
SPL	Sound Pressure Level

STAR	Standard Terminal Arrival Route
TL	Transmission Loss

### Roman symbols

$a$	Parameter in equations ( 1.27 ) and ( 1.28 )
$A$	Attenuation factor
$b$	Parameter in equations ( 1.27 ) and ( 1.28 )
$b_1$	Parameter in equation ( 1.14 )
$b_2$	Parameter in equation( 1.15 )
$c$	Sound speed
$c_0$	Sound speed at ground surface
$c_{eff}$	Effective sound speed
$C_{sat}$	Parameter defined in equation ( 1.20 )
$f$	Frequency
$f_{c,l}$	Lower frequency of a 1/3-octave band
$f_{c,m}$	Center frequency of a 1/3-octave band
$f_{c,u}$	Upper frequency of a 1/3-octave band
$f_{r,N}$	Relaxation frequency of nitrogen
$f_{r,O}$	Relaxation frequency of oxygen
$g$	Grain shape factor
$g_2$	Two dimensional Green's function
$g_3$	Three dimensional Green's function
$h$	Parameter in equation ( 1.18 )
	Airplane height in equations ( 5.1 ) and ( 5.2 )
$H_1$	Quantity defined in equation ( 2.29 )
$H_{1a}$	Quantity defined in equation ( 2.31 )
$H_2$	Quantity defined in equation ( 2.28 )
$H_{2a}$	Quantity defined in equation ( 2.30 )
$k$	Wave number
$k_0$	Reference wave number in equation ( 2.26 )
$k_a$	Reference wave number in equation ( 2.27 )
$k_{abs}$	Absorption layer wave number
$k_{eff}$	Effective wave number
$k_h$	Horizontal wave number
$k_v$	Vertical wave number
$k_z$	Vertical wave number
$L_A$	A-weighted sound pressure level
$L_{AE}$	Sound exposure level

$L_{Amax}$	Maximum A-weighted sound pressure level
$L_E$	Single event sound exposure level
$L_{eq}$	Equivalent sound exposure level
$L_{max}$	Maximum sound pressure level
$L_p$	Sound pressure level
$L_{PNT}$	Tone-corrected perceived noise level
$L_W$	Sound power level
$M$	Number of vertical points in the PE grid
$\mathbf{n}$	Unit outward normal vector
$N$	Number of aircraft movements
	Size of the Fourier transforms for the GFPE method
$N_1$	Engine rotational speed
$p$	Complex pressure amplitude, ( $p \equiv p_c$ )
$p_a$	Atmospheric pressure
$p_c$	Complex pressure amplitude
$p_f$	Harmonic pressure signal
$p_{free}$	Complex pressure of free field
$p_r$	Reference atmospheric pressure
$p_{ref}$	Reference pressure level
$q$	Quantity defined in equation ( 2.7 ), ( $q \equiv q_c$ )
$q_c$	Quantity defined in equation ( 2.4 ), ( $q \equiv q_c$ )
$r$	Horizontal distance
	Radial distance in equations ( 1.4 ), ( 2.35 ) and ( 3.1 )
$\mathbf{r}$	Two dimensional position vector
$r_h$	Relative humidity
$\mathbf{R}$	Position vector
$R_1$	Distance travelled by the direct ray
$R_2$	Distance travelled by the reflected ray
$R_A$	A-weighting filter
$R_p$	Plane wave reflection coefficient
$s_f$	Pore shape factor ratio of porous medium
$S_c$	Closed Surface
$t$	Ambient air temperature (in °C)
$t_0$	Reference time
$T$	Absolute temperature
$T_0$	Reference temperature
$T_{01}$	Triple point temperature of water
$T_{20}$	Reference temperature for the atmospheric absorption calculations
$\mathbf{u}$	Wind speed vector of three components

$u_r$	Horizontal wind component (cylindrical coordinates)
$u_\theta$	Angular wind component (cylindrical coordinates)
$u_z$	Vertical wind component (cylindrical coordinates)
$v_c$	Speed amplitude of a travelling acoustic wave
$V_2$	Takeoff safety speed
$V_C$	Calibrated airspeed
$V_{ZF}$	Zero flap minimum safety speed
$z$	Vertical distance
$z_0$	Parameter in equations ( 1.27 ) and ( 1.28 )
$z_{abs}$	Initial height of the absorption layer in PE grid
$z_{aircraft}$	Aircraft height (above ground level)
$z_s$	Source height
$z_{top}$	Height of the PE grid
$Z_g$	Normalized ground impedance

### Greek Symbols

$\alpha$	Atmospheric absorption coefficient
	Attenuation factor in the absorption layer, defined in equation ( 2.46 )
$\beta$	Quantity defined in equation ( 2.26 )
$\gamma$	Elevation angle
	Ray trajectory angle in chapter 3
$\gamma_{max}$	Maximum elevation angle for the parabolic equation methods
$\delta$	Dirac delta function
$\Delta k$	Wave number spacing
$\Delta L$	Relative sound pressure level
$\Delta L_{absorption}$	Atmospheric absorption
$\Delta L_{lateral}$	Lateral directivity correction
$\Delta L_{longitudinal}$	Longitudinal directivity correction
$\Delta L_{spreading}$	Geometrical attenuation
$\Delta r$	Horizontal grid spacing
$\Delta z$	Vertical grid spacing
$\zeta_{air}$	Acoustic impedance of air
$\zeta_g$	Acoustic impedance of (ground) surface air
$\theta$	Angle of incidence
	Temperature ratio in equation ( 5.3 )
	Spherical longitudinal angle
$\theta_i$	Angle of incidence
$\theta_r$	Angle of reflection

$\theta'$	Angle of transmission
$\lambda$	Wavelength
$\Pi$	Quantity defined in equation ( 2.42 )
$\rho_0$	Air density
$\rho_r$	Pressure ratio
$\rho_{sat}$	Saturation pressure ratio
$\sigma$	Effective flow resistivity
$\tau_r$	Temperature ratio
$\phi$	Azimuthal angle
$\varphi$	Spherical lateral angle in equations ( 5.4 ) and ( 5.5 )
$\psi$	Quantity defined in equation ( 2.33 )
$\Psi$	Quantity defined in equation ( 2.34 )
$\omega$	Angular frequency
$\Omega$	Porosity of porous medium



# 1 Introduction

## 1.1 Motivation

For communities established in the vicinity of airports, aviation noise has become a major concern as the regular operation of multiple aircraft can become an unwelcome presence. Although aircraft are becoming quieter, due to the forecasts of continuous air traffic growth (International Civil Aviation Organization, 2010) and increased public awareness to the health issues brought by aircraft noise, these concerns are becoming more important than ever and it is expected that they continue to drive both commercial and military operations.

In order to establish an oriented approach to mitigate the impact of aircraft operations, the International Civil Aviation Organization (ICAO) (International Civil Aviation Organization, 2008, 2013) has proposed four major fields of intervention, namely noise reduction at source, land planning, noise abatement procedures and operational constraints. There has been a continuous and successful effort to decrease aircraft noise emissions, thus making land planning and optimization of in-flight procedures the areas where improvement must be pursued as a means of preventing restrictions and penalties to aircraft movements.

Following these directives, several computational applications have been developed by national authorities in order to predict noise contours in major airports that can help to minimize the impact of aviation noise by providing tools that facilitate land use management as well as offer a direct approach to mitigate noise influence in specific areas. For these reasons, viable numerical models must be employed with the purpose of producing accurate results regarding noise propagation in the atmosphere.

The research discussed in this dissertation is based on two well-known numerical models of sound propagation, namely the parabolic equation model and the ray model which are combined in a hybrid propagation model in order to study a wide range of propagation conditions as well as to be applicable to the particular situation of aviation noise in the vicinity of airports.

This chapter presents the most important mechanisms of outdoor sound propagation and presents the state of the art in propagation modeling and aviation oriented computational tools. Afterwards, it describes the main goals of this research and briefly outlines the remainder of this dissertation.

## 1.2 Outdoor Sound Propagation

### 1.2.1 Atmospheric acoustics

The atmosphere is a complex environment with a multitude of variables that affect both directly and indirectly the propagation of sound. The purpose of atmospheric acoustics is to accurately compute the sound field in the atmosphere and ultimately provide the sound pressure level (SPL)  $L_p$  at a receiver, which is related to the complex pressure amplitude  $p_c$  of a harmonic spherical wave.

In practice the pressure produced by these mechanical waves is small when compared to the ambient pressure and consequently the SPL is expressed in a logarithmic scale in decibels, abbreviated *dB*, where the value of *0 dB* corresponds to the threshold of human perception and *130 dB* to the threshold of pain (Salomons, 2001). Another consequence of the limited amplitude of sound waves when compared to the atmospheric pressure is that the mathematical derivation of the acoustic equations only considers the first order terms and so atmospheric acoustics are also referred to as linear acoustics. The SPL measured in decibels is then calculated as follows

$$L_p = 20 \log_{10} \left( \frac{1}{2} \frac{|p_c|}{p_{ref}} \right), \quad (1.1)$$

where  $p_{ref}$  is a reference value to the threshold of human hearing (at *1 kHz*) usually considered as  $2 \times 10^5 \text{ Pa}$ .

Typically the pressure amplitude  $p_c$  is obtained from numerical simulations by employing empirical correlations or propagation models, thus equation ( 1.1 ) cannot be applied directly in these cases and it is recommended to follow the expression presented below

$$L_p = L_W - \Delta L_{spreading} - \Delta L_{absorption} + \Delta L, \quad (1.2)$$

being  $L_W$  the sound power level of the acoustic source (a measure of the signal strength),  $\Delta L_{spreading}$  the geometrical attenuation due to the expansion of the wave front (detailed in section 1.2.2);  $\Delta L_{absorption}$  is related to the phenomenon of atmospheric absorption (described in section 1.2.3) and finally the relative SPL  $\Delta L$  is obtained from the propagation algorithms and measures the influence of the atmosphere and ground interaction on the sound field.

The relative SPL  $\Delta L$  is a comparison of the pressure level  $p_c$  obtained from the numerical calculations against the corresponding value  $p_{free}$  in a unbounded homogeneous atmosphere and satisfies the following relation

$$\Delta L = 20 \log_{10} \left( \frac{|p_c|}{|p_{free}|} \right), \quad (1.3)$$

where the free field pressure amplitude at a distance  $r$  from the source is computed by

$$p_{free}(r) = S \frac{e^{ikr}}{r}, \quad (1.4)$$

being  $S$  a constant and  $k$  the wave number.

Another parameter that allows the definition of the pressure field created by a monopole source is the transmission loss (TL) which is calculated as follows

$$TL = 20 \log_{10}(|p_c|), \quad (1.5)$$

This quantity is very useful for the comparison of benchmark test cases as a validation criteria for numerical propagation models.

Equations ( 1.2 ) to ( 1.4 ) model a generic outdoor sound propagation situation, although they are only valid for harmonic sources, where there is only one frequency. In reality sound sources are often not harmonic (e.g. an aircraft) and it is necessary to decompose the sound signal into several harmonic components:

$$p(t) = \sum p_f(t) \quad (1.6)$$

where  $p_f(t)$  are the harmonic pressure signals of the source frequency spectrum.

The combination of all harmonic contributions is called logarithmic summation of the harmonic levels  $L_p(f)$  and it is given by

$$L_p = 10 \log_{10} \left( \sum 10^{\frac{L_p(f)}{10}} \right). \quad (1.7)$$

It can be observed that for a source containing a large number of harmonic contributions the previous calculations are time consuming and therefore one typically replaces the values of each individual frequency by a smaller normalized number of octave or 1/3-octave bands. These levels are obtained by dividing the human hearing spectrum into several intervals characterized by a center frequency, a lower frequency and an upper frequency (see Figure 1.1).

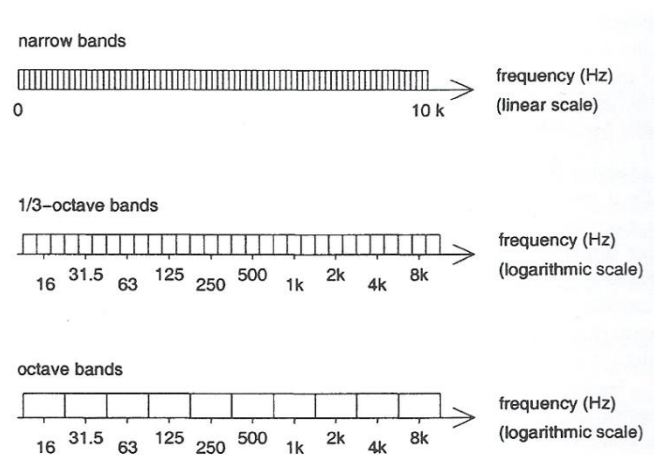


Figure 1.1 - Illustration of frequency scales: narrow band, 1/3-octave band and octave band scale. (Salomons, 2001).

The following three equations mathematically define respectively the center, lower and upper frequencies of a  $m^{th}$  order band:

$$f_{c,m} \approx 1000 \times 2^{-10+m/3} [Hz] \quad (1.8)$$

$$f_{c,l} = f_{c,m} \times 2^{-1/2} [Hz] \quad (1.9)$$

$$f_{c,u} = f_{c,m} \times 2^{1/2} [Hz] \quad (1.10)$$

where  $m = 1,2,3, \dots$  for 1/3-octave bands and  $m = 3,6,9, \dots$  for octave bands. Consequently, the study of a sound field produced by a non harmonic source is simplified by limiting the number of harmonic frequencies to a representative group.

The following sections will describe the various correction factors existing in equation ( 1.2 ) that arise from the complexity of the atmosphere and their influence in the SPL at the receiver.

### 1.2.2 Geometrical spreading

As a sound wave propagates across the atmosphere in the outward direction from a source (i.e. with increasing radius), the wave front is expanded and consequently the sound intensity decreases. For a monopole source in a unbounded medium this spreading is spherical, thus the variation of the sound pressure level at a distance  $r$  from the source is calculated as follows

$$\Delta L_{spreading} = 10 \log_{10}(4\pi r^2). \quad (1.11)$$

As it will be seen along this dissertation a single vehicle (like an airplane) may be regarded as a point source and therefore equation ( 1.11 ) is applied in the numerical models implemented in the present work.

### 1.2.3 Atmospheric absorption

Geometrical spreading only represents a fraction of the overall reduction of sound power in the atmosphere as a result of wave front expansion.

For long range propagation the atmosphere dissipates part of the total sound intensity as the wave front travels away from the source. This effect is mainly frequency and range dependent and becomes significant when both of these quantities increase in magnitude. This noise attenuation is called atmospheric absorption and results from three major phenomena:

- i. Thermal conduction and viscosity of air;
- ii. Vibrational relaxation of air molecules (namely oxygen and nitrogen);
- iii. Rotational relaxation of air molecules.

Therefore, the numerical computation of the sound field produced by a source must include this atmospheric influence and two different approaches are available. The first option consists in including atmospheric absorption in the propagation model itself by adding an imaginary term to the wave number. The second solution is illustrated in equation ( 1.2 ) and considers a correction term in the overall pressure calculation. This correction factor is determined by the following expression

$$\Delta L_{absorption} = \alpha r, \quad ( 1.12 )$$

where  $r$  is the radial distance travelled by the wave front and  $\alpha$  is the absorption coefficient.

The absorption coefficient was defined in the International Standard ISO 9613-1:1993(E) and the necessary expressions are published by Salomons (2001). The computation of this quantity requires three atmospheric parameters: the absolute temperature  $T$  in  $K$ , the relative humidity  $r_h$  in % and the atmospheric pressure  $p_a$  in  $Pa$ . The absorption coefficient in  $dB$  per meter for a sound wave with frequency  $f$  follows the relation

$$\alpha = 8.686 f^2 \tau_r^{1/2} (1.84 \times 10^{-11} \rho_r^{-1} + \tau_r^{-3} [b_1 + b_2]), \quad ( 1.13 )$$

where  $\tau_r = T/T_{20}$  and  $\rho_r = p_a/p_r$  are respectively the ratios of temperature and pressure, and the reference values are  $T_{20} = 293.15 K$  and  $p_r = 101\,325 Pa$ .

The coefficients  $b_1$  and  $b_2$  are given by

$$b_1 = 0.1068 \frac{e^{(-3352/T)}}{f_{r,N} + f^2/f_{r,N}}, \quad ( 1.14 )$$

$$b_2 = 0.01275 \frac{e^{(-2239.1/T)}}{f_{r,O} + f^2/f_{r,O}}, \quad ( 1.15 )$$

where  $f_{r,N}$  and  $f_{r,O}$  are the relaxation frequencies of nitrogen and oxygen respectively and can be calculated by the following equations

$$f_{r,N} = \rho_r \tau_r^{-1/2} \left( 9 + 280 h e^{-4.17[\tau_r^{-1/3} - 1]} \right) \quad ( 1.16 )$$

$$f_{r,O} = \rho_r \left[ 24 + \frac{40400 h (0.02 + h)}{0.391 + h} \right], \quad ( 1.17 )$$

the quantity  $h$  being defined as

$$h = r_h \frac{\rho_{sat}}{\rho_r}. \quad ( 1.18 )$$

The variable  $\rho_{sat}$  can be written as

$$\rho_{sat} = 10^{C_{sat}}, \quad (1.19)$$

with

$$C_{sat} = -6.8346 \left( \frac{T_{01}}{T} \right)^{1.261} + 4.6151, \quad (1.20)$$

where  $T_{01} = 273.16 \text{ K}$  is the triple point temperature of water.

Figure 1.2 shows a typical evolution of the absorption coefficient with the wave frequency and it proves the initial statement that atmospheric absorption increases with increasing frequency.

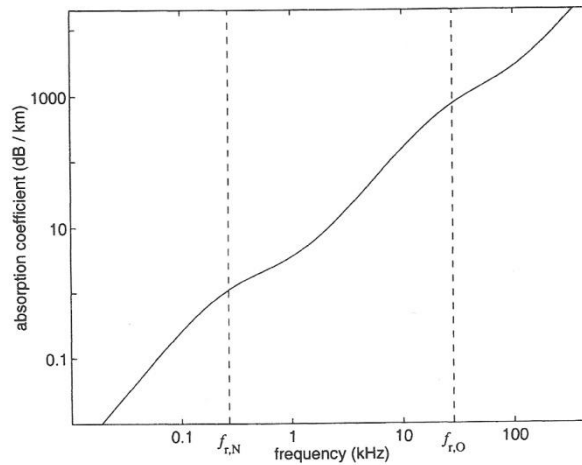


Figure 1.2 - Example of a typical evolution of the absorption coefficient as a function of the source frequency (Salomons, 2001).

#### 1.2.4 Ground interaction

When the source or the receiver, or both, are close to the ground surface a complex interaction between sound waves takes place and affects sound propagation. This occurs in the majority of outdoor sound propagation when sound waves reach the ground. In this situation, it can be observed that part of the wave is reflected back to the atmosphere and another fraction is absorbed by the ground (see Figure 1.3), thus the propagation models need to consider both direct travelling waves and ground reflected sound waves and one needs to define a quantity that describes the acoustic behavior of a plane surface when in presence of incident sound waves.

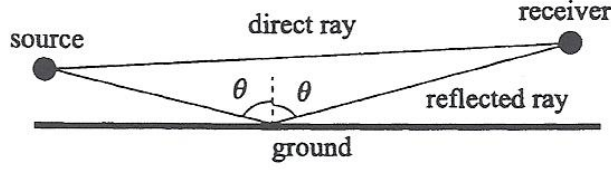


Figure 1.3 - Illustration of reflection of sound waves on a ground surface (Salomons, 2001).

The reflection coefficient for a plane wave on a locally reacting surface is calculated as follows (Salomons, 2001)

$$R_p = \frac{Z_g \cos \theta - 1}{Z_g \cos \theta + 1} \quad (1.21)$$

where  $\theta$  is the angle of incidence and  $Z_g$  is a property of the reflective material denominated normalized ground impedance. The reflection coefficient can be computed by equation ( 1.21 ) for every type of sound wave as long as both source and receiver are not in a low position and it is a good approximation, as considering the more adequate spherical wave reflection coefficient results in a more complex process.

The normalized impedance is defined as follows:

$$Z_g = \frac{\zeta_g}{\zeta_{air}} \quad (1.22)$$

where the acoustic impedance  $\zeta = p_c/v_c$  is the ratio of the complex pressure and the speed amplitude of an acoustic wave travelling through a given medium.

Several authors proposed different accurate models that simulate the acoustic behavior of different materials based on empirical correlations that depend on the wave frequency and on the type of ground material (Attenborough, 1985; Delany and Bazley, 1970; Zwicker and Kosten, 1949). In the computational tool developed in the present work we adopted the empirical model presented by Delany and Bazley (1970) and described by Salomons (2001)

$$Z_g = 1 + 0.0511 \left( \frac{\sigma}{f} \right)^{0.75} + i 0.0768 \left( \frac{\sigma}{f} \right)^{0.73} \quad (1.23)$$

where  $\sigma$  is the effective flow resistivity of the porous material. Embleton et al. (1983) published different values of flow resistivity for a wide range of materials of interest for aviation oriented simulations as shown in Table 1.1.

Table 1.1 - Effective flow resistivity for different materials, from Embleton et al. (1983) and reproduced by Rosenbaum (2011).

Description of surface	Effective flow resistivity [ $kPa\ s/m^2$ ]
0.1 m new fallen snow, over older snow	10 – 30
Sugar snow	25 – 50
Floor of evergreen forest	20 – 80
Airport grass or old pasture	150 – 300
Roadside dirt, ill-defined, small rocks up to 0.01 m mesh	300 – 800
Sandy silt, hard packed by vehicles	800 – 2500
Thick layer of clean limestone chips, 0.01 to 0.025 m mesh	1500 – 4000
Old dirt roadway, small stones with interstices filled by dust	2000 – 4000
Earth, exposed and rain-packed	4000 – 8000
Very fine quarry dust, hard packed by vehicles	5000 – 20 000
Asphalt, sealed by dust and use	~ 30 000
Upper limit, set by thermal conduction and viscosity	$2 \times 10^5$ to $1 \times 10^6$

### 1.2.5 Atmospheric refraction

Atmospheric refraction can be regarded as the change of the wave propagation direction due to the effects of the sound speed gradient. This phenomenon can be neglected for small receiver distances but in long range propagation it should not be ignored.

The atmospheric sound speed depends on the ambient temperature  $T$  and this relation can be defined by

$$c = c_0 \sqrt{\frac{T}{T_0}}, \quad (1.24)$$

where the quantities  $c_0$  and  $T_0$  are related to each other are commonly set respectively to  $c_0 = 343\ m/s$  and  $T_0 = 293\ K$ .

Two situations of interest arise from the existence of temperature gradients in the atmosphere. The first one corresponds to the daytime situation when the ambient temperature decreases with increasing height. In this case sound waves travelling closer to the ground surface will propagate faster than the waves travelling at the top layers of the atmosphere and consequently the various wave fronts are bent upwards, as illustrated by Figure 1.4 (right figure). The second situation is related to the nighttime period when an inversion may occur and the ground cools faster than the surrounding atmosphere and for that reason the sound waves are bent downwards, as in Figure 1.4 (left figure).

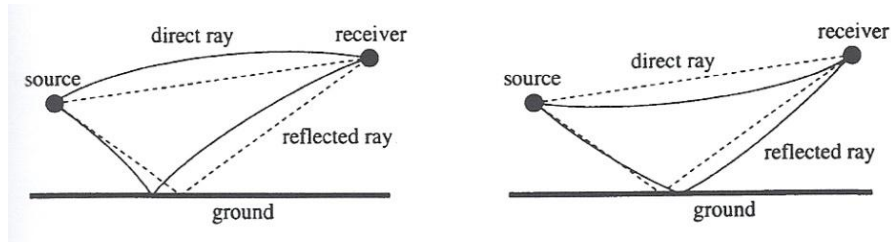


Figure 1.4 - Direct ray and reflected ray in a downward refracting atmosphere (left) and upward refracting atmosphere (right) (Salomons, 2001).

However, temperature gradients are not the only cause to atmospheric refraction as the existence of wind may also create similar effects to the ones explained in the previous paragraph. Unlike the refraction caused by temperature gradients, which is identical in all directions, ray deflection due to atmospheric winds depends on both sound propagation direction and wind direction. We can represent the wind as a vector of three components in a cylindrical coordinate system

$$\mathbf{u}(r, \theta, z) = (u_r, u_\theta, u_z), \quad (1.25)$$

where  $u_r$  is the wind speed component in the direction of sound propagation,  $u_z$  is the vertical component of the wind vector and  $u_\theta$  relates to the crosswind part of the wind vector.

We can approximate a moving atmosphere to a non-moving atmosphere by using an effective sound speed that only accounts for the wind component in the direction of sound propagation as it is the most influencing part when studying sound refraction. Therefore, we may define the effective sound speed as

$$c_{eff} = c + \|\mathbf{u}\| \approx c + u_r. \quad (1.26)$$

From equation ( 1.26 ) we may observe that wind blowing in the direction of sound propagation induces downward refraction as it adds a positive contribution to the sound speed. Following a similar analysis, if the wind direction is opposite to the direction of sound propagation upward refraction is observable.

There are several functions defining the atmospheric speed profile  $c(z)$  that allow the simulation of wave refraction. These expressions also reproduce the effects of wind speed and in the remainder of this dissertation we will denote the effective sound speed as  $c_{eff} \equiv c$ . In the program developed in this thesis we included, besides a constant speed profile, two functions that simulate the atmospheric acoustic behavior. The first is a linear evolution as follows

$$c(z) = c_0 + az. \quad (1.27)$$

The second is more frequently applied when a more realistic model is needed:

$$c(z) = c_0 + az + b \ln\left(1 + \frac{z}{z_0}\right). \quad (1.28)$$

The adjustment of the various constants allows the user to obtain a more or less realistic representation of the atmosphere; the values adopted in the development of numeric results are described later in this dissertation.

### **1.3 State of the Art in Aviation Noise**

Standard computational tools are oriented towards the application in a typical personal computer in order to optimize runtimes and consequently several simplifications regarding the physics of sound propagation are employed by resorting to empirical correlations. As computational power increases, these simplifications may be substituted by physics-based propagation methods and as a result more realistic results are achieved.

The following two sections will provide an overview of the computational tools designed for the study of aviation noise and the propagation models commonly used in sound propagation applications. The third section is related to the typical indices used to evaluate the impact of aircraft operations on the surrounding communities.

#### **1.3.1 Aviation oriented computational tools**

As stated previously, aviation noise is a primary concern of both regulators and operators. Therefore, several computational tools were developed in order to study the impact of aircraft operations in the surrounding communities, like the FAA's (Federal Aviation Administration) Integrated Noise Model (Federal Aviation Administration, 2008) and the Aviation Environmental Design Tool (Federal Aviation Administration, 2014). It is also worth mentioning the CAA's (Civil Aviation Authority) Aircraft Noise Contour Model software (Ollerhead, 1992; Ollerhead et al., 1999).

These programs typically rely on noise databases supplied by aircraft manufactures at the moment of noise certification called Noise Power Distance (NPD) databases. These tables present the relevant noise data of multiple aircraft at normalized conditions and are published by several aviation authorities (Eurocontrol, 2012).

The software tools previously mentioned compute the sound levels by following the general procedure described below which is proposed by the European Civil Aviation Conference (ECAC) (European Civil Aviation Conference, 2005a, 2005b):

- i. Load the intended aircraft route;
- ii. Divide the selected route into several linear segments;
- iii. Compute the sound level of each segment;
- iv. Apply corrections to the values obtained in the previous steps.

Therefore, it can be observed that these computational models do not calculate directly the propagation of sound waves emitted by an airplane, but instead they obtain the relevant results at the

observer's location by using empirical correlations and correction factors. As computational resources continue to evolve, more complex propagation methods can be adopted to allow more accurate results (Rosenbaum, 2011) and, although at an initial stage of implementation, this approach is starting to be adopted by aviation regulators and organizations (Rosenbaum et al., 2012a, 2012b).

### 1.3.2 Numerical propagation models

There are three propagation methods widely used in atmospheric sound propagation modeling that provide accurate results for a wide range of test cases which are the Fast Field Program (FFP), the Parabolic Equation (PE) method and the Ray Model.

The FFP was firstly created to study underwater sound propagation (Dinapoli and Deavenport, 1979; Jensen et al., 1994) and was later adapted to meet the requirements of atmospheric acoustics (Lee et al., 1986). This numerical method is characterized, as seen in Figure 1.5, by the division of the atmosphere into several horizontal homogeneous layers (each one with its own effective sound speed) in order to solve the two dimensional wave equation.

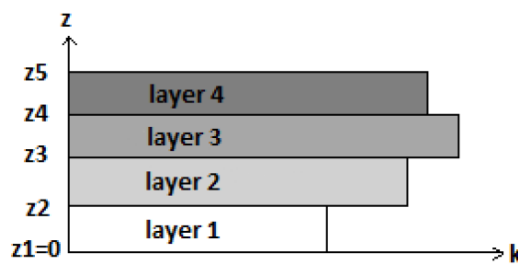


Figure 1.5 - Representation of a layered atmosphere for the FFP model (Salomons, 2001).

The pressure field is calculated by solving the wave equation in the horizontal wave number domain. This can be accomplished by first applying a Fourier transform and after the numerical solution is obtained, an inverse Fourier transform is used to write the sound field in the original spatial coordinates.

The use of the FFP is restricted to environments where each layer contains a constant value of sound speed, therefore reducing the complexity of situations that can be simulated. Nevertheless, the Fast Field Program is accurate in a wide range of situations that approximate a real moving atmosphere with realistic wind and temperature gradients and it is not time consuming in long range calculations.

The second approach that obtains the sound field produced by a monopole source is based on a parabolic equation that approximates the wave equation and therefore it is only valid for situations of one way propagation, neglecting back scattering of sound waves.

In order to solve the parabolic equation, this propagation model employs a numerical step by step method by using a two dimensional grid (see Figure 1.6) and sequentially solving the parabolic equation.

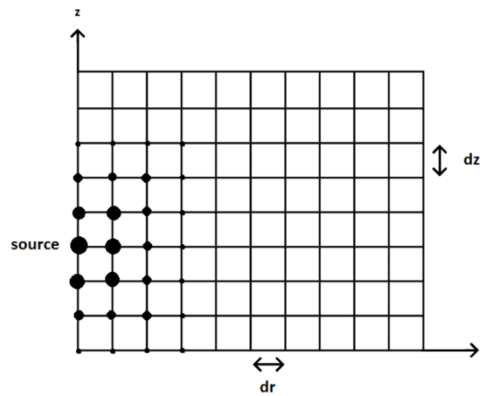


Figure 1.6 - Two dimensional numerical grid used in the PE models (Salomons, 2001).

This method allows greater flexibility in the definition of atmospheric parameters considering range dependent conditions and it may even include atmospheric turbulence. In order to minimize the computational resources consumed by this method, only two dimensions are usually considered by employing an axisymmetric approximation.

As this approach is based on a parabolic equation, the numerical computations at each step will require data from previous calculations and consequently various schemes arise as means of solving the parabolic equation. There are two numerical schemes that are most commonly used: the Crank-Nicholson Parabolic Equation method (CNPE) and the Green's Function Parabolic Equation method (GFPE).

The main difference between both models is related to the accuracy that each scheme can accomplish, which is typically associated with the maximum elevation angle  $\gamma_{max}$  that provides accurate results. Therefore, the pressure amplitudes obtained with each method are only valid if the receiver presents an elevation angle smaller than the maximum allowed, as exemplified in Figure 1.7.

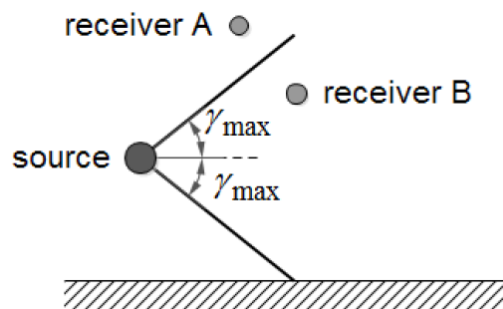


Figure 1.7 - Representation of the angular limitation of PE schemes (Oliveira, 2012).

The Crank-Nicholson method was firstly derived by Gilbert (1989) and a detailed description on its application to outdoor sound propagation is presented by West et al. (1992).

In each step of this numerical algorithm, the wave equation derivatives are approximated by a finite difference Crank-Nicholson scheme.

As this is a step by step method an initial field must be provided. The CNPE model accepts two types of initial sound fields, each guaranteeing different validity regions: a narrow-angle approach (where  $\gamma_{max} = 15^\circ$ ) or a wide-angle starting field (with  $\gamma_{max} = 35^\circ$ ).

The numerical grid is built by choosing suitable values for the horizontal and vertical spacing. A maximum value of  $\lambda/10$ , where  $\lambda$  is the average wavelength, is recommended. Consequently the grid spacing is frequency dependent and for high frequencies and long range propagation the CNPE method is computationally heavy due to the large number of range steps that are necessary.

This disadvantage is overcome by the GFPE computational model. This method was developed by Gilbert and Di (1993) and later on improved by Salomons (1998) and requires a numerical grid similar to the one represented in Figure 1.6. The solution of the approximated wave equation is computed in the vertical wave number domain and requires, like the FFP, two Fourier transforms, the first one being responsible for the transformation from the spatial domain into the vertical wave number space and the second one related to the inverse operation.

The numerical formulation of the GFPE model allows the use of range steps up to 50 wavelengths (Gilbert and Di, 1993) although several considerations must be taken into account to guarantee an accurate solution (Cooper and Swanson, 2007). Therefore, as the horizontal spacing between successive extrapolation steps becomes larger, the computational time consumed in the overall simulation is reduced. This property of the GFPE scheme makes it the appropriate choice for the majority of situations simulated in the aircraft noise scenario, merging the superior flexibility in modeling the atmosphere of the PE method with the faster long range calculations of the FFP algorithm.

The ray model, also called geometrical acoustics, is based on the calculation of sound rays trajectories as a means of obtaining the sound field created by a sound source. The determination of the path length and the associated travel time allows the calculation of the pressure amplitude at each receiver by applying the expression related to an omnidirectional point source. These quantities are obtained by integrating Snell's law along each ray.

This numerical scheme is valid for both refracting and non-refracting atmospheres thus allowing the definition of a realistic sound speed profile. For short range propagation this model can be simplified by neglecting the refraction effects whereas for larger distances the curvature of the sound rays must be considered and an iterative ray tracing algorithm must be implemented.

The main disadvantage of the ray model occurs when two sound rays intersect. In this case, geometrical acoustics predicts an infinite pressure amplitude when in reality it assumes a finite yet high value. This situation is called caustics and it requires computational methods to be developed to overcome the associated loss of accuracy (Salomons, 2001). Therefore, although the ray model is accurate for a wide range of sound propagation situations it becomes less attractive as the correction of caustic fields in complex environments involves the addition of several time consuming processes.

### 1.3.3 Aviation noise metrics

The quantities defined in section 1.2 allow the determination of the sound field (in terms of sound pressure level) emanating from a monopole source defined by a power spectrum.

However, when studying aviation noise this quantity is not sufficient as the main goal is to study the effect of aircraft operations in the surrounding populations and therefore the numerical models must include algorithms that rewrite the noise data in terms of human perception.

The first main characteristic of human perception that can be modeled is the different sensitivity of the human ear in the audible frequency spectrum. This phenomenon can be studied using two different scales: the A-weighted sound level and the Tone-corrected Perceived Noise Level.

The A-weighting scale consists on a simple filter that applies more or less emphasis to certain frequencies to mirror the human ear sensitivity. This scale is applied in almost every sound application and the A-weighted levels are normally defined as  $L_A$ . The mathematical definition of the sound filter defined in this paragraph is exposed below (Salomons, 2001)

$$L_A(f) = L_p(f) + 20 \log_{10} \left( \frac{R_A(f)}{R_A(1000)} \right), \quad (1.29)$$

where  $R_A(f)$  is given by

$$R_A(f) = \frac{12200^2 f^4}{(f^2 + 20.6^2)(f^2 + 12200^2)(f^2 + 107.7^2)^{1/2}(f^2 + 737.9^2)^{1/2}} \quad (1.30)$$

and  $R_A(1000)$  is defined by equation ( 1.30 ) for a frequency of 1000 Hz.

The tone-corrected perceived noise levels (denoted  $L_{PNT}$ ) are mainly used for precision aircraft noise measurements and model the human perception of noise from sources consisting of pure tones or other spectral irregularities (European Civil Aviation Conference, 2005a). As this frequency weighting scale is computed by a complex procedure, as established by the International Civil Aviation Organization (2005), it is not modeled in the program developed in this thesis.

The second characteristic of human perception that must be taken into account when studying aircraft noise is related to the exposure to a certain noise event and it is denominated noise metrics. There are two main categories regarding noise metrics, the first describing the single noise events (Single Event Noise Metrics) and the other considering the effects of longer exposure intervals (Cumulative Noise Metrics). The latter index, a measure of community annoyance, will not be approached in this dissertation as it is related to multiple aircraft movements and therefore does not lie within the scope of this research.

Single Event Noise Metrics studies the influence of a single aircraft operation and two quantities are defined in this context. Firstly we may consider the maximum sound pressure level  $L_{max}$  experienced in the entire exposure period as the characterizing parameter of the airplane movement. Alternatively one may take the total sound energy contained in the airplane movement and consider a

generic single event sound exposure level  $L_E$  as the variable that defines the noise event. This measure is defined by the following relation

$$L_E = 10 \log_{10} \left( \frac{1}{t_0} \int_{t_1}^{t_2} 10^{L(t)/10} dt \right), \quad (1.31)$$

where  $t_0$  is a reference time.

In the aircraft noise environment, three different single event metrics arise from the two previous quantities. The first is the A-weighted sound level  $L_{Amax}$  that corresponds to the maximum sound pressure level measured during the exposure corrected by the frequency filter defined in equations ( 1.29 ) and ( 1.30 ). The second measure is called Sound Exposure Level (SEL) and it is denoted by  $L_{AE}$ . This metric accounts for both duration and intensity of the event and therefore it is preferred over  $L_{Amax}$  for daily noise monitoring at airports as it provides more information than the A-weighted sound level and it is used to build cumulative noise indices when needed. SEL is consequently derived from equation ( 1.31 ) and is defined by

$$L_{AE} = 10 \log_{10} \left( \frac{1}{t_0} \int_{t_1}^{t_2} 10^{L_A(t)/10} dt \right) \text{ with } t_0 = 1 \text{ second}. \quad (1.32)$$

The choice of the integration interval must guarantee that all relevant sound levels are enclosed. For that reason, the European Civil Aviation Conference (2005a) recommends that the time interval  $[t_1, t_2]$  should only include the sound levels  $L_A$  that lie within 10 dB of the maximum sound level  $L_{Amax}$ , instead of using the whole time history of  $L_A(t)$ .

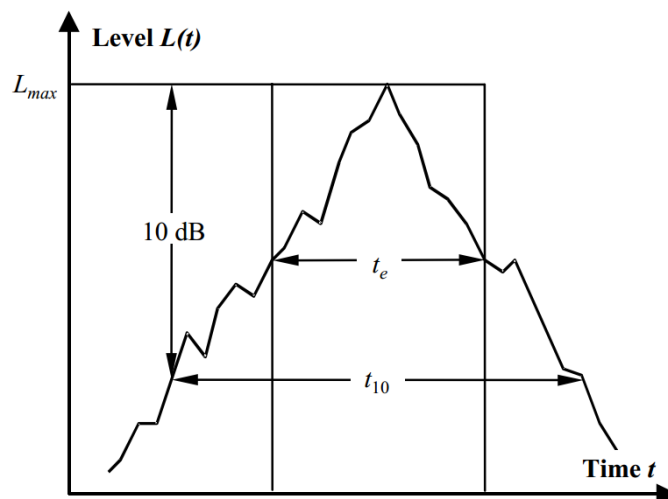


Figure 1.8 - Level time history of a noise event (European Civil Aviation Conference, 2005a).

These two quantities,  $L_{Amax}$  and  $L_{AE}$ , can be obtained from direct measurements using standard precision data acquisition equipment, while the third single event metric, called Effective Perceived Noise Level (EPNL), is related to the aircraft certification process as specified by ICAO

Annex 16. This noise index is calculated from the tone-corrected levels  $L_{PNT}$  and consequently shares the degree of complexity stated previously. Although EPNL is calculated by an expression equivalent to ( 1.31 ) it was not implemented in the developed application as the computation of  $L_{PNT}$  is intricate and complex.

## 1.4 Research Objectives and Outline

The main objective of the research discussed in this dissertation was to develop a computational tool that accurately predicts aviation noise in simplified environmental conditions at a specified location. In order to accomplish this goal, attention was given to both the propagation modeling and to the adequate representation of an aircraft as a noise source.

The propagation of acoustic waves was studied by developing an hybrid model consisting of the combination of two popular propagation methods, the parabolic equation method and a simplified ray model in order to minimize their limitations and maximize their capabilities.

The noise source modeling was based on the empirical studies employed by Eurocontrol (Eurocontrol, 2012) regarding the spectral distribution of the sound power level for a various number of aircraft. Focus was given to the inclusion of directivity effects in the hybrid propagation model by applying simplified relations to both longitudinal and lateral directivity of aircraft (Butikofer, 2006).

This chapter provided an overview of the various dimensions related to outdoor sound propagation and the challenges involved in accurately modeling realistic conditions.

Chapters 2 and 3 discuss respectively the details in the formulation of the two dimensional parabolic equation method and the ray model, including the numerical implementation adopted while developing the hybrid computational tool.

Chapter 4 describes the combination of the two propagation methods and outlines the overall structure of the hybrid model and its relation to the limitations presented by each individual propagation model.

Chapter 5 provides an insight to the process of modeling aircraft as an aircraft source, describing the process to obtain sound power spectra from experimental data and the process of including directivity corrections along a flight path.

Chapter 6 of this text relates to the general structure of the created computational tool in Matlab environment, focusing on the code structure and user interaction.

Chapter 7 details the validation process of the two propagation models used to develop the hybrid approach. Afterwards, it validates the transition region created to merge both theories, focusing on the determination of its structure and limits.

Chapter 8 applies the developed program to an airport situation, using realistic aircraft trajectories and parameters, evaluating the obtained results.

At last, chapter 9 provides a global overview of the discussed work, including suggested future work guidelines for further developments on this theme.

## 2 Green's Function Parabolic Equation Method (GFPE)

In this chapter, we intend at first to provide a brief theoretical background of the two-dimensional GFPE method, both in a homogeneous and inhomogeneous atmosphere above a ground surface. The remainder of the chapter is oriented to the details involved in the numerical implementation of such propagation model.

### 2.1 Theoretical Formulation

#### 2.1.1 Inhomogeneous Helmholtz equation

The propagation model derived in this chapter is based on linear acoustics, which considers that the pressure variations created by a sound wave are small when compared with the average pressure in the surrounding environment. This assumption allows the elimination of the nonlinear terms that are only necessary when studying very loud sounds such as the sound of an explosion (Salomons, 2001).

Considering a monopole source in a moving atmosphere with a non constant sound speed profile, the corresponding three dimensional Helmholtz equation is

$$k_{eff}^2 \nabla \cdot (k_{eff}^{-2} \nabla p_c) + k_{eff}^2 p_c = 0, \quad (2.1)$$

where  $p_c(\mathbf{R})$  is the complex pressure amplitude,  $\mathbf{R}$  is a position vector and  $k_{eff}$  is the effective wave number, defined as

$$k_{eff} = \frac{\omega}{c_{eff}}, \quad (2.2)$$

where  $\omega$  is the angular frequency of the sound wave and  $c_{eff}$  is the effective sound speed as described in section 1.2.5.

As the majority of sound propagation models is based on a two-dimensional atmosphere, further simplifications may be applied to the three dimensional Helmholtz equation. Using a cylindrical coordinate system  $(r, \phi, z)$ , being  $\phi$  the azimuthal angle and  $r$  and  $z$  consistent with Figure 1.6, equation (2.1) is written as

$$\frac{1}{r} \frac{\partial}{\partial r} \left( r \frac{\partial p_c}{\partial r} \right) + k_{eff}^2 \frac{\partial}{\partial z} \left( k_{eff}^{-2} \frac{\partial p_c}{\partial z} \right) + \frac{1}{r^2} \frac{\partial^2 p_c}{\partial \phi^2} + k_{eff}^2 p_c = 0. \quad (2.3)$$

In the axisymmetric simplification we consider that the sound field is independent of the azimuthal angle and therefore we can neglect the third term on the left-hand side of the previous equation. Replacing  $p_c$  by the quantity

$$q_c = p_c \sqrt{r} \quad (2.4)$$

and assuming only the far-field approximation, the resulting equation is

$$\frac{\partial^2 q_c}{\partial r^2} + k_{eff}^2 \frac{\partial}{\partial z} \left( k_{eff}^{-2} \frac{\partial q_c}{\partial z} \right) + k_{eff}^2 q_c = 0. \quad (2.5)$$

For most numerical applications, the second term of equation ( 2.5 ) can be approximated by (Salomons, 2001)

$$k_{eff}^2 \frac{\partial}{\partial z} \left( k_{eff}^{-2} \frac{\partial q_c}{\partial z} \right) \approx \frac{\partial^2 q_c}{\partial z^2}. \quad (2.6)$$

Replacing  $k_{eff}$  by  $k$  and  $q_c$  by  $q$ , equation ( 2.5 ) becomes

$$\frac{\partial^2 q}{\partial r^2} + \frac{\partial^2 q}{\partial z^2} + k^2 q = 0. \quad (2.7)$$

where  $q = q(r, z)$  and  $k = k(z)$ . This last equation is the basis for the derivation of the GFPE propagation model.

### 2.1.2 Kirchhoff-Helmholtz integral equation

Considering now a volume  $V$  occupied by an inhomogeneous fluid and enclosed by a surface  $S$  with an outward normal vector  $\mathbf{n}$ , it can be shown that the complex pressure amplitude  $p(\mathbf{R}_1)$  at a point  $\mathbf{R}_1 = (x_1, y_1, z_1)$  can be calculated by employing the Kirchhoff-Helmholtz integral equation

$$p(\mathbf{R}_1) = \frac{1}{4\pi} \iint_{S_c} [g_3(\mathbf{R}, \mathbf{R}_1) \nabla p(\mathbf{R}) - p(\mathbf{R}) \nabla g_3(\mathbf{R}, \mathbf{R}_1)] \cdot \mathbf{n} dS_c, \quad (2.8)$$

where the integral is evaluated over  $\mathbf{R} = (x, y, z)$  on the surface  $S$  and the pressure amplitude  $p(\mathbf{R})$  is a solution of the homogeneous Helmholtz equation in volume  $V$

$$\nabla^2 p(\mathbf{R}) + k^2(\mathbf{R}) p(\mathbf{R}) = 0. \quad (2.9)$$

Also, it can be shown that the Green's function  $g_3(\mathbf{R}, \mathbf{R}_1)$  satisfies the homogeneous Helmholtz equation in volume  $V$  with a point source at  $\mathbf{R}_1$

$$\nabla^2 g_3(\mathbf{R}, \mathbf{R}_1) + k^2(\mathbf{R})g_3(\mathbf{R}, \mathbf{R}_1) = -4\pi\delta(\mathbf{R} - \mathbf{R}_1). \quad (2.10)$$

The two dimensional Kirchhoff-Helmholtz can be obtained from equation ( 2.8 ) by considering only the  $xz$  plane

$$p(\mathbf{r}_1) = \frac{1}{4\pi} \int_C [g_2(\mathbf{r}, \mathbf{r}_1)\nabla p(\mathbf{r}) - p(\mathbf{r})\nabla g_2(\mathbf{r}, \mathbf{r}_1)] \cdot \mathbf{n} ds, \quad (2.11)$$

where  $\mathbf{r} = (x, z)$  and  $\mathbf{r}_1 = (x_1, z_1)$ ; the integral is evaluated on the closed contour  $C$  (as represented by Figure 2.1), where  $g_2(\mathbf{r}, \mathbf{r}_1)$  is a two dimensional Green's function.

Following a similar procedure, the three dimensional Helmholtz equation is transformed into

$$\nabla^2 p(\mathbf{r}) + k^2(\mathbf{r})p(\mathbf{r}) = 0. \quad (2.12)$$

The associated two dimensional Green's function satisfies the inhomogeneous Helmholtz equation and is obtained from integration of equation ( 2.10 ) over  $y = -\infty$  to  $y = +\infty$  as follows

$$\nabla^2 g_2(\mathbf{r}, \mathbf{r}_1) + k^2(\mathbf{r})g_2(\mathbf{r}, \mathbf{r}_1) = -4\pi\delta(\mathbf{r} - \mathbf{r}_1). \quad (2.13)$$

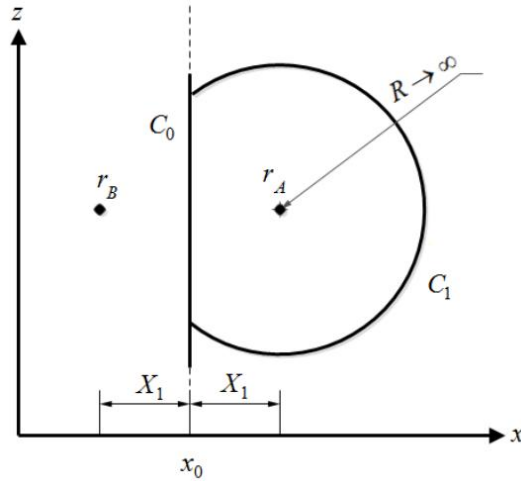


Figure 2.1 – Geometry for the two dimensional Kirchhoff-Helmholtz equation (Salomons, 2001).

Figure 2.1 represents the two dimensional geometry used for the two dimensional Kirchhoff-Helmholtz equation, where the closed contour  $C$  is defined by the linear segment  $C_0$  and the arc  $C_1$  with radius  $R$ . It can be shown (Salomons, 2001) that as  $R$  goes to infinity, the pressure contribution from the circular segment  $C_1$  vanishes. There is a significant freedom regarding the choice of the two

dimensional Green's function; it is only required that this function contains a contribution from a point source at position  $\mathbf{r}_1$  in order to guarantee that equation ( 2.13 ) is satisfied. As additional sources outside the closed contour  $C$  can be added to the Green's function, if two monopole sources are placed symmetrically with respect to the line  $C_0$  (on positions  $\mathbf{r}_1$  and  $\mathbf{r}_2$ ) the contribution of this segment to  $g_2$  is eliminated and the resulting Green's function is

$$g_2(\mathbf{r}, \mathbf{r}_1) = g(\mathbf{r}, \mathbf{r}_1) - g(\mathbf{r}, \mathbf{r}_2). \quad (2.14)$$

Applying ( 2.14 ) on the two dimensional Kirchhoff-Helmholtz equation ( 2.11 ), the first term in the integrand vanishes and in the second term we have  $\nabla g_2 \cdot \mathbf{n} = -\partial_x g_2 = -2\partial_x g$ . Therefore, equation ( 2.11 ) becomes

$$p(\mathbf{r}_1) = \frac{1}{2\pi} \int_{-\infty}^{+\infty} \left( p(r) \frac{\partial g(\mathbf{r}, \mathbf{r}_1)}{\partial x} \right)_{x=x_0} dz. \quad (2.15)$$

### 2.1.3 General Green's function method

In this section we return to the notation used previously in section 2.1.1. For a system with a ground surface at  $z = 0$ , equation ( 2.15 ) becomes

$$q(r_1, z_1) = \frac{1}{2\pi} \int_0^{\infty} \left( q(r, z) \frac{\partial g(r, z; r_1, z_1)}{\partial r} \right)_{r=r_0} dz. \quad (2.16)$$

The two dimensional Green's function is also a solution of the two dimensional wave equation as follows

$$[\partial_r^2 + \partial_z^2 + k^2(z)]g(r, z; r_1, z_1) = -4\pi\delta(r - r_1)\delta(z - z_1), \quad (2.17)$$

where it is assumed that the wave number  $k$  is a function of  $z$  only, so that the range dependence of the wave number is modeled by changing its value between successive horizontal steps. Consequently, the Green's function can be expressed as  $g(\Delta r, z, z_1)$ , where  $\Delta r = r_1 - r$  is the horizontal spacing. To write the Green's function with relation to the horizontal wave  $k_h$ , the following Fourier transform is introduced (Salomons, 2001)

$$G(k_h, z, z_1) = \int_{-\infty}^{+\infty} g(\Delta r, z, z_1) e^{-ik_h \Delta r} d(\Delta r). \quad (2.18)$$

The inverse Fourier transform is expressed by the following equation

$$g(\Delta r, z, z_1) = \frac{1}{2\pi} \int_{-\infty}^{+\infty} G(k_h, z, z_1) e^{ik_h \Delta r} dk_h. \quad (2.19)$$

Considering the Fourier transform properties, substitution of ( 2.19 ) into ( 2.16 ) gives (changing the notation from  $z_1$  to  $z$  and from  $z$  to  $z'$ )

$$q(r + \Delta r, z) = \frac{1}{4\pi^2 i} \int_{-\infty}^{+\infty} k_h e^{ik_h \Delta r} dk_h \int_0^{\infty} G(k_h, z', z) q(r, z') dz'. \quad (2.20)$$

The Green's function  $G(k_h, z', z)$  satisfies the Fourier transformed variant of ( 2.17 ) and it is written as

$$[\partial_z^2 + k^2(z) - k_h^2]G(k_h, z', z) = -4\pi\delta(z - z'). \quad (2.21)$$

#### 2.1.4 Constant sound speed profile

For a non-refracting atmosphere we have a constant wave number, such that  $k(z) = k_0$ , where  $k_0$  is a reference wave number (typically at the ground surface). In this situation, for a system with a ground surface at zero height, the solution of ( 2.21 ) is (Gilbert and Di, 1993)

$$G(k_h, z', z) = \frac{2\pi i}{k_v} \{e^{ik_v|z-z'|} + R(k_v)e^{ik_v|z+z'|}\} \quad (2.22)$$

where  $k_v$  is the vertical wave number defined by

$$k_v^2 = k^2(z) - k_h^2 \quad (2.23)$$

and  $R(k_v)$  is the plane wave reflection coefficient defined as follows

$$R(k_v) = \frac{k_v Z_g - k_0}{k_v Z_g + k_0}. \quad (2.24)$$

where  $Z_g$  is the normalized impedance of the ground surface, as explained in section 1.2.4.

Substituting ( 2.22 ) into ( 2.20 ) yields

$$q(r + \Delta r, z) = \frac{1}{\pi i} \int_{-\infty}^{+\infty} k_h e^{ik_h \Delta r} dk_h \int_0^{\infty} \frac{i}{2k_v} \{e^{ik_v|z-z'|} + R(k_v)e^{ik_v|z+z'|}\} q(r, z') dz'. \quad (2.25)$$

Salomons (2001) provides a detailed derivation of the governing equation of the GFPE method which can be obtained by applying the residue theorem and manipulating the integrals in equation ( 2.25 ) in order to get a unique dependence on the wave number

$$\begin{aligned}
q(r + \Delta r, z) = & \frac{1}{2\pi} \int_{-\infty}^{+\infty} e^{i\Delta r \sqrt{k_0^2 - k_z^2}} e^{ik_z z} dk_z \int_0^{\infty} e^{-ik_z z'} q(r, z') dz' \\
& + \frac{1}{2\pi} \int_{-\infty}^{+\infty} R(k_z) e^{i\Delta r \sqrt{k_0^2 - k_z^2}} e^{ik_z z} dk_z \int_0^{\infty} e^{ik_z z'} q(r, z') dz' \\
& + 2i\beta e^{-i\beta z} e^{i\Delta r \sqrt{k_0^2 - \beta^2}} \int_0^{\infty} e^{-i\beta z'} q(r, z') dz',
\end{aligned} \tag{ 2.26 }$$

where  $\beta = k_0/Z_g$  is the surface wave pole coefficient.

This expression consists in a sum of three integrands each one representing a different type of sound wave. The first term refers to the direct wave, the second represents the wave reflected by the ground surface and the third term is related to the surface wave.

### 2.1.5 Non-constant sound speed profile

In this section, we discuss the derivation of the basic equation for the GFPE method when considering a refracting atmosphere. In this situation, the variation of the wave number in each range step is small enough to consider that the wave number is only a function of height; therefore it can be defined as

$$k^2(z) = k_a^2 + \delta k^2(z), \tag{ 2.27 }$$

being  $k_a$  a constant wave number at an average height, typically assumed as the value obtained at the ground surface.

Returning to equation ( 2.7 ), the wave equation can be written as follows

$$\partial_r^2 q(r, z) = -H_2(z)q(r, z), \tag{ 2.28 }$$

where  $H_2(z) = k^2(z) + \partial_z^2$ .

Considering  $H_1 = \sqrt{H_2}$ , the associated one way wave equation is

$$\partial_r q(r, z) = iH_1(z)q(r, z), \tag{ 2.29 }$$

being the positive side related to waves travelling in the positive direction of  $r$  and the negative sign applied for waves travelling in the opposite direction.

For a refracting atmosphere, the operator  $H_2$  becomes

$$H_2(z) = H_{2a} + \delta k^2(z), \quad (2.30)$$

with  $H_{2a} = k_a^2 + \partial_z^2$ . Consequently, the square-root operator may be written as

$$H_1(z) \approx H_{1a} + \frac{\delta k^2(z)}{2k_a}, \quad (2.31)$$

where  $H_{1a}^2 = H_{2a}$ .

Integrating the one way wave equation over one range step results in

$$q(r + \Delta r, z) = e^{i\Delta r \frac{\delta k^2(z)}{2k_a}} e^{iH_{1a}\Delta r} q(r, z) \quad (2.32)$$

For improved numerical accuracy, the quantity  $q(r, z)$  is replaced by  $\psi(r, z) = e^{-ik_a r} q(r, z)$  and ( 2.32 ) becomes

$$\begin{aligned} \psi(r + \Delta r, z) = e^{i\Delta r \frac{\delta k^2(z)}{2k_a}} & \left\{ \frac{1}{2\pi} \int_{-\infty}^{+\infty} [\Psi(r, k_z) \right. \\ & + R(k_z)\Psi(r, -k_z)] e^{i\Delta r \left( \sqrt{k_a^2 - k_z^2} - k_a \right)} e^{ik_z z} dk_z \\ & \left. + 2i\beta\Psi(r, \beta) e^{-i\beta z} e^{i\Delta r \left( \sqrt{k_a^2 - \beta^2} - k_a \right)} \right\}, \end{aligned} \quad (2.33)$$

where

$$\Psi(r, k_z) = \int_0^{\infty} e^{-ik_z z'} \psi(r, z') dz' \quad (2.34)$$

is the spatial Fourier Transform of  $\psi(r, z)$ .

## 2.2 Numerical Implementation

The numerical implementation of the GFPE propagation model is based on the computation of equations ( 2.33 ) and ( 2.34 ). According to their mathematical nature, it is observable that numerical methods are required in order to solve these expressions, which will be described in this chapter.

As the GFPE method is a step by step extrapolation of the sound field  $\psi(r + \Delta r, z)$ , a two dimensional rectangular grid is used, where the two grid parameters (horizontal spacing  $\Delta r$  and vertical spacing  $\Delta z$ ) are frequency dependent. The length of the numerical grid is defined by the number of horizontal steps necessary to reproduce the horizontal distance between the source and

the receiver. Simultaneously, the grid is limited by the ground surface at  $z = 0$  and at a height  $z_{top} = M\Delta z$ , where  $M$  is a positive integer and dependent on the source height.

The following sections discuss the various details that must be considered when implementing the GFPE method in a programming language.

### 2.2.1 Starting field

As stated above, the GFPE model is based on the successive extrapolation of the sound field so it is mandatory to define a initial field that models a monopole source. In a unbounded non-refracting environment, this type of source is represented by a spherical harmonic wave as follows

$$p_c(r) = S \frac{e^{ikr}}{r}, \quad (2.35)$$

where  $p_c$  is the complex pressure amplitude,  $S$  is a constant and  $r$  is the radial distance from the source to the receptor. Equation ( 2.35 ) cannot be used in actual algorithms as it diverges at the source (when the distance reaches zero) and consequently leads to numerical errors.

For that reason we use a Gaussian starting field defined as (Salomons, 2001)

$$q(0, z) = \sqrt{ik_a} (A_0 + A_2 k_a^2 z^2 + A_4 k_a^4 z^4 + A_6 k_a^6 z^6 + A_8 k_a^8 z^8) e^{-\frac{k_a^2 z^2}{B}} \quad (2.36)$$

where the coefficients  $A_i$  and  $B$  are dependent on the order of the Gaussian field and established on the following table:

Table 2.1 – Values of the parameters  $A$  and  $B$  in Equation ( 2.36 ), from Salomons (2001).

Order	$A_0$	$A_2$	$A_4$	$A_6$	$A_8$	$B$
0	1	0	0	0	0	2
2	1.3717	-0.3701	0	0	0	3
4	1.9705	-1.1685	0.0887	0	0	3
8	9.6982	-20.3785	6.0191	-0.4846	0.0105	3

For a source near a ground surface, it is mandatory to include the contribution from the reflected wave as follows

$$q(0, z) = q_0(z - z_s) + \frac{Z_g - 1}{Z_g + 1} q_0(z + z_s), \quad (2.37)$$

being  $q_0$  calculated by equation ( 2.36 ) and  $z_s$  the source height above the ground surface.

## 2.2.2 Discretization of the Fourier integrals

The determination of the sound field at each range step requires the computation of several Fourier integrals, as shown in equation ( 2.33 ). Adopting the discrete domain (as the sound field is being calculated in a numerical grid), it can be shown that each of the integrals may be regarded as a sum denominated Discrete Fourier Transform (DFT). Following the procedure developed by Oppenheim et al. (1998) the Fourier transform in equation ( 2.34 ) in its discrete form is

$$\Psi(r, k_z) = \int_0^{\infty} e^{-ik_z z'} \psi(r, z') dz' \approx \left[ \sum_{j=0}^{N-1} \psi(r, z_j) e^{-ik_n z_j} \right] \Delta z, \quad (2.38)$$

where the two integration variables are discretized as

$$k_n = n\Delta k, \quad n = 0, 1, 2, \dots, N/2, -N/2 + 1, -N/2 + 2, \dots, -1 \quad (2.39)$$

$$z_j = j\Delta z, \quad j = 0, 1, 2, \dots, N - 1, \quad (2.40)$$

where  $\Delta k = 2\pi/(N\Delta z)$ ,  $\Delta z$  is the vertical spacing of the numerical grid and  $N = 2M$  is the Fourier transform size, related to the grid vertical dimension.

In order to reduce the computational effort required to calculate the two Fourier transforms included in equation ( 2.33 ), the periodic property inherent to the definition of Fourier transform is adopted and both  $\Psi(r, k_z)$  and  $\Psi(r, -k_z)$  may be determined with a single transform of size  $N = 2M$  and related by a permutation of vector positions.

On the other hand, the integral  $\Psi(r, \beta)$  is calculated with a single summation of  $N$  terms following the definition of a DFT

$$\Psi(r, \beta) \approx \left[ \sum_{j=0}^{N-1} \psi(r, z_j) e^{-i\beta z_j} \right] \Delta z. \quad (2.41)$$

Applying a similar procedure, the inverse Fourier transform of equation ( 2.33 ) can be approximated by

$$\psi(r, z_j) = \int_{-\infty}^{\infty} \Pi(r, k_z) e^{ik_z z} dk_z \approx \left[ \sum_{n=0}^{N-1} \Pi(r, k_n) e^{ik_n z_j} \right] \Delta k, \quad (2.42)$$

where

$$\Pi(r, k_n) = [\Psi(r, k_n) + R(k_n)\Psi(r, -k_n)] e^{i\Delta r \left( \sqrt{k_a^2 - k_n^2} - k_a \right)}. \quad (2.43)$$

Therefore, equation ( 2.33 ) in the discrete domain is

$$\psi(r + \Delta r, z_j) = e^{i\Delta r \frac{\delta k^2(z)}{2k_a}} \left\{ \frac{1}{2\pi} \psi(r, z_j) + 2i\beta\Psi(r, \beta) e^{-i\beta z_j} e^{i\Delta r \left( \sqrt{k_a^2 - \beta^2} - k_a \right)} \right\} \quad ( 2.44 )$$

### 2.2.3 Fast Fourier Transform (FFT)

Although the DFT algorithm is simple to implement in a programming language, the computing time required for the direct and inverse Fourier transforms may become impractical for large volumes of data. For that reason, the program discussed in this thesis includes a Matlab built-in function which applies a procedure called Fast Fourier Transform that, while producing the exact same results as the DFT, reduces the computing time significantly. This Matlab function is based on the algorithm originally developed by Matteo Frigo and Steven Johnson at the Massachusetts Institute of Technology, denominated “Fast Fourier Transform in the West” (Frigo and Johnson, 1997).

### 2.2.4 Artificial absorption layer

In real outdoor sound propagation, the atmosphere can be considered as an infinite medium regarding its vertical dimension, where sound waves travel until their amplitude reaches zero. However, the discrete formulation of the governing equations as discussed in section 2.2.2 requires a finite length of the atmosphere and consequently introduces unwanted and unrealistic reflections of sound waves at the top of the numerical grid. This numerical error can be eliminated by introducing an artificial absorption layer at the top of the grid which attenuates the sound waves travelling upwards and reaching the maximum height discretized (Gilbert and Di, 1993; Salomons, 1998). The implementation of such attenuation layer involves the manipulation of the wave number at the affected grid points by adding an imaginary part to its real value as follows

$$k_{abs} = k(z) + i\alpha(z), \quad ( 2.45 )$$

where the imaginary part is calculated by

$$\alpha(z) = A \left( \frac{z - z_{abs}}{z_{top} - z_{abs}} \right)^2, \quad ( 2.46 )$$

being  $A$  a frequency dependent attenuation factor (Gilbert and Di, 1993; Salomons, 1998) defined in Table 2.2,  $z_{abs}$  the initial height of the absorption layer and  $z_{top}$  the maximum height of the numerical grid. Intermediate values of  $A$  may be computed by linear interpolation.

Table 2.2 – Values of the attenuation factor for an octave band scale (Salomons, 1998).

$f(\text{Hz})$	$\leq 16$	31.5	63	125	250	500	$\geq 1000$
$A(\text{m}^{-1})$	0.1	0.2	0.3	0.4	0.5	0.5	1

The absorption layer discussed in this section has a thickness based on the wavelength of travelling sound waves and is typically delimited by  $50\lambda$  and  $100\lambda$  to avoid increasing the size of the Fourier transforms used in this propagation method.

### 2.2.5 Alternate refraction factor

In the GFPE method, atmospheric refraction was originally included by multiplying the solution by the exponential factor shown below

$$e^{i\Delta r \frac{\delta k^2(z)}{2k_a}} \quad (2.47)$$

However, an alternate exponential factor was developed and it can be shown that it provides more accurate results than the one defined in equation ( 2.47 ). The derivation of this refraction factor is based on the expansion of the square-root operator (Salomons, 2001)

$$H_1(z) = \sqrt{(k_a + \delta k)^2 + \partial_z^2} \approx \sqrt{k_a^2 + \partial_z^2} + \delta k \quad (2.48)$$

where  $k(z) = \delta k(z) + k_a$ . Therefore the alternate refraction factor used in the algorithm developed in Matlab language is

$$e^{i\Delta r \delta k(z)}. \quad (2.49)$$



## 3 Ray Model

In this chapter, we discuss the theoretical formulation of the propagation method named ray model and provide a derivation for a simplified version developed for a reduction of the computational effort required. Afterwards, we study the implementation of such model in the programming language selected for the present work.

### 3.1 Theoretical Formulation

#### 3.1.1 Snell's Law

Outdoor sound propagation may be regarded as the propagation of multiple sound rays emanated from a source across the atmosphere; this approach is called geometrical acoustics.

Recovering equation ( 2.35 ), the complex pressure amplitude at a receiver intersected by a sound ray is calculated as follows

$$p_c(r) = S \frac{e^{ikr}}{r}, \quad (3.1)$$

where  $S$  is a constant,  $r$  is the distance travelled by the sound ray from the source to the receptor and  $k$  the wave number.

Therefore, from equation ( 3.1 ) we may conclude that the pressure amplitude at a specified location is given by the sum of the pressure amplitudes of each ray that passes through that position (Salomons, 2001)

$$p_c = \sum_{m=1}^{N_{rays}} A_m e^{i\phi_m}, \quad (3.2)$$

where the amplitudes  $A_m$  and phases  $\phi_m$  follow by comparison with equation ( 3.1 ).

The computation of the total pressure at a specific receiver is correlated with the determination of all rays intersecting that location and consequently it is necessary to follow a procedure called ray tracing. The trajectory followed by a sound ray is obtained from the integration of Snell's law, which is defined as

$$\frac{\cos \gamma}{c} = \text{constant along a sound ray}, \quad (3.3)$$

where  $\gamma$  is the angle of the ray's trajectory, as defined by Figure 3.1 and  $c = c(z)$  is the sound speed at the height where the calculation is done. As the quotient in equation ( 3.3 ) is constant along a sound ray, it can be also written as (following the notation on Figure 3.1)

$$\frac{\cos \gamma_1}{c_1} = \frac{\cos \gamma_2}{c_2}. \quad (3.4)$$

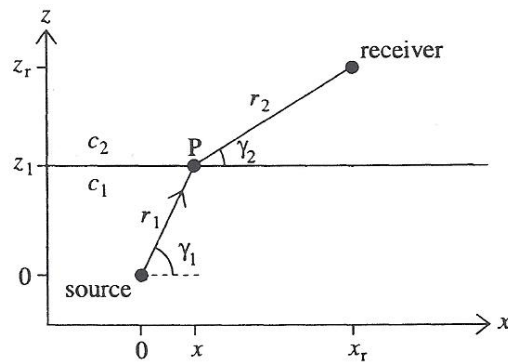


Figure 3.1 – Refracted ray from a monopole source to a receiver in the same atmosphere (Salomons, 2001).

Figure 3.1 represents a situation where the sound speed profile is defined by two values of speed separated by a simple discontinuity where, by applying equation ( 3.4 ) one can obtain the ray trajectory from the initial angle  $\gamma_1$ . For a continuous speed profile, equation ( 3.4 ) is also valid as long as there is an initial known value for the trajectory's angle. From the computation of the trajectory angles, the distance  $r$  travelled by the sound ray is obtained by geometrical relations.

In sections 3.1.2 and 3.1.3 we will discuss the application of the ray model in the situations where the atmosphere presents a constant or a refracting sound speed profile.

### 3.1.2 Constant sound speed profile

A non-refracting atmosphere is one where the sound speed profile is defined by a single constant  $c_0$  as follows

$$c(z) = c_0. \quad (3.5)$$

Referring to equation ( 3.4 ) and applying the speed profile presented in this section, it can be stated that the trajectory of a sound ray in a homogeneous atmosphere is represented by a straight line due to the constant nature of the speed profile.

For that reason, in a unbounded homogeneous atmosphere, each location is intersected by a single ray emanated from a source, while in a homogeneous atmosphere with a ground surface the pressure amplitude consists in the contribution of both a direct and a reflected ray; in the latter situation we are in conditions of developing a two ray model which will be discussed in more detail in section 3.2.

### 3.1.3 Non-constant sound speed profile

A refracting atmosphere is characterized by a non-constant sound speed profile, where the sound speed can be a continuous or a discontinuous function of height.

This condition implies that the trajectory of the sound rays is curved according to the speed gradient along the atmosphere, justifying the definitions of downward and upward refracting atmospheres (as seen in section 1.2.5). Therefore, the problem of computing the sound field at a spatial location in these conditions differs from the procedure described in section 3.1.2 as there is no initial estimate of the number of rays that pass at the receiver location. In the case of a refracting atmosphere, the complex pressure is calculated by tracing each ray that originates from the source. This is accomplished by integrating Snell's law, which is presented in equation ( 3.4 ). Although some speed profiles allow the calculation of an analytical solution (for example, a linear relation of the type  $c(z) = c_0 + az$ ) more complex equations that model more accurately a real atmosphere require the implementation of a numerical integration scheme in order to obtain ray trajectories and consequently the computational effort for larger distances between source and receiver is increased due to the growing number of ground reflections of the sound rays. Based on the assumption of a downward refracting atmosphere, Salomons (2001) presents a detailed derivation for a ray tracing algorithm.

### 3.1.4 Ground interaction

As seen in the previous paragraphs, sound rays may reach the receiver directly or after one or more ground reflections.

Therefore, the mechanism of reflection and its influence on the ray's trajectory must be included in the ray model.

Figure 3.2 defines the situation of an oblique reflection of a sound wave by a ground surface, where  $\theta_i$  is the angle of incidence,  $\theta_r$  is the angle of reflection and  $\theta'$  is the angle of transmission.

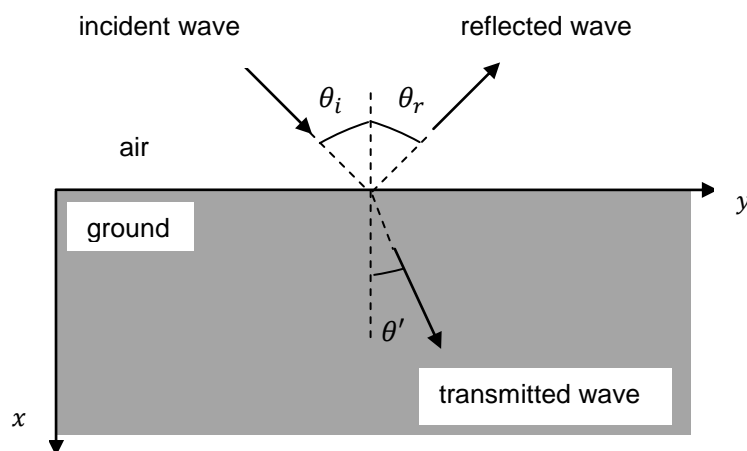


Figure 3.2 – Oblique reflection of a sound wave by a flat ground surface (Salomons, 2001).

Assuming a perfectly flat surface, the law of reflections states that (Salomons, 2001)

$$\theta_i = \theta_r, \quad (3.6)$$

so we may conclude that the angle of incidence of the sound ray is equal to the angle of the reflected wave therefore the computation of ray trajectories when a ground reflection occurs can be easily accomplished by using this equation.

### 3.2 Numerical Implementation

As seen in section 3.1 the implementation of the ray model in a programming language may become complex for situations comprehending simultaneously long range propagation, refracting atmospheres and low elevation angles.

For that reason, we implemented in the hybrid propagation model developed in this thesis a simplified version called two ray model (Boeker and Rosenbaum, 2012; de Roo et al., 2007) where only two sound rays are considered, the direct ray and the reflected ray. This simplification is well suited for the situation where large elevation angles and consequently short range sound propagation are being considered, as the real number of rays intersecting the receiver location is close to two while in the opposite case (long range propagation) the number of sound rays is typically superior to two.

Figure 3.3 represents the rays included in this simplified approach for a general case involving one source and one receiver.

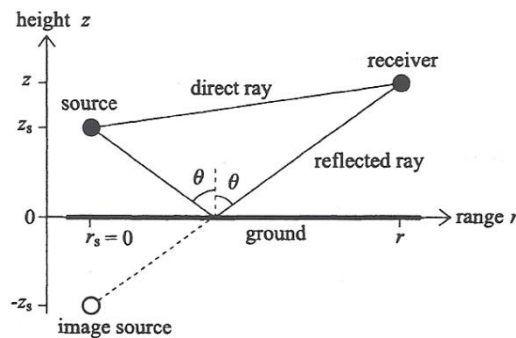


Figure 3.3 – Geometry of the two ray model with a source and receiver above a ground surface (Salomons, 2001).

As the two ray model is only valid for large elevation angles, it can be concluded that in its region of validity, ray curvature is in practice negligible so an additional approximation is employed where both rays are modeled as straight rays. This assumption simplifies the implementation of this method as the determination of ray travel time and distance is accomplished by elementary trigonometric relations instead of following from the integration of Snell's law.

Defining the source position as  $(0, z_s)$  and the receiver location by  $(r, z)$  (see Figure 3.3), the distance travelled by the direct ray is

$$R_1 = \sqrt{r^2 + (z - z_s)^2}. \quad (3.7)$$

On the other hand, the distance covered by the reflected ray may be calculated considering an imaginary source below the ground source resulting in

$$R_2 = \sqrt{r^2 + (z + z_s)^2}. \quad (3.8)$$

At last, the determination of the pressure amplitude follows the relation given by

$$p_c = S \frac{e^{ikR_1}}{R_1} + R_p S \frac{e^{ikR_2}}{R_2}, \quad (3.9)$$

being  $R_p$  the plane wave reflection coefficient defined as

$$R_p = \frac{Z_g \cos \theta - 1}{Z_g \cos \theta + 1}. \quad (3.10)$$



## 4 Hybrid Numerical Model

The following sections will discuss the implementation of an hybrid propagation model based on the methods described in chapters 2 and 3, respectively the GFPE method and the two ray model.

Firstly we approach the limitations of both models and then we describe the available procedures for model combination and associated limitations regarding their implementation in a programming language and also focusing on the impact on the computational resources needed to run the combination criteria.

### 4.1 Propagation models limitations

#### 4.1.1 GFPE model

The GFPE propagation method is well suited for low elevation angles and it is valid for a wide variety of sound frequencies. Its accuracy is accomplished by fine tuning the various numerical parameters that characterize this model and it is mostly related to a variation in the maximum elevation angle that limits the region where the GFPE method is valid.

It can be verified that the maximum elevation angle where accuracy can be attained is mainly due to the choice of an adequate starting field (Cooper and Swanson, 2007) while the other numerical variables have a lower influence on the region of validity. Therefore, it can be shown that a standard Gaussian field (Gilbert and Di, 1993) provides accurate results up to an elevation angle of  $35^\circ$  whereas a higher-order starting field (Salomons, 2001) as the one described in section 2.2.1 returns an accurate pressure field for a maximum angle of approximately  $50^\circ$ .

#### 4.1.2 Two ray model

The simplified variant of the ray model implemented in this thesis is employed for high elevation angles, where the number of rays that reaches the receiver's position is approximately two and the effects of atmospheric refraction are negligible.

For that reason, the lower limit of the validity region of the two ray model is typically imposed at approximately  $50^\circ$  (Boeker and Rosenbaum, 2012), where the effects described previously start to affect the accuracy of sound field obtained from the numerical calculations.

### 4.2 Model combination

The main concern while developing an hybrid approach based on different models is the boundary definition for each of the individual methods in order to guarantee a smooth transition between the results obtained by the different methods.

There are various published procedures regarding model combinations with different degrees of complexity. The first approach consists in dividing the spatial domain into two regions (Boeker and Rosenbaum, 2012; Rosenbaum and Boeker, 2014) separated by a transition angle such that the sound pressure level  $L_P$  at the receiver (with an associated elevation angle  $\gamma$  between the source and the receptor) is evaluated as follows

$$L_P = \begin{cases} L_{P,GFPE}, & \gamma < \gamma_{transition} \\ L_{P,Ray Model}, & \gamma \geq \gamma_{transition} \end{cases}, \quad (4.1)$$

being  $L_{P,GFPE}$  and  $L_{P,Ray Model}$  the values of the sound pressure level at a receiver calculated respectively with the GFPE method and the two ray model, while  $\gamma_{transition}$  is the angle that defines the separation between both regions. This combination model is of simple implementation and does not increase the overall computational capacity required for the propagation calculations. However it is necessary that a careful choice of  $\gamma_{transition}$  is employed to maximize the number of cases where a smooth transition is obtained.

The second transition criterion is based on the determination of the region where only two sound rays occur. This procedure involves the calculation of the caustic curves (where the number of rays jumps from two to four) or alternatively one may determine the curve created by the collection of the turning points of each sound ray (de Roo et al., 2007). This method, although more accurate and precise than the one previously described, is highly dependent on the atmospheric parameters used (namely those affecting atmospheric refraction) and consequently it may require a considerable volume of computational effort as each pair of receiver and source positions is needed for the computation of the specific transition curves.

For that reason, we developed a method that, while preserving a simple implementation in a programming language as the first one, merges the results obtained in a transition region by employing a linear interpolation scheme as below

$$L_P = L_{P,GFPE} \frac{\gamma_{top} - \gamma}{\gamma_{top} - \gamma_{bottom}} + L_{P,Ray Model} \frac{\gamma - \gamma_{bottom}}{\gamma_{top} - \gamma_{bottom}}, \quad (4.2)$$

where  $\gamma_{bottom}$  and  $\gamma_{top}$  are respectively the lower and upper limits of the combination region; equation ( 4.2 ) is valid only when the elevation angle  $\gamma$  is within the interval  $\gamma_{bottom} \leq \gamma \leq \gamma_{top}$ , otherwise we apply an equivalent criterion to the one presented in equation ( 4.1 )

$$L_P = \begin{cases} L_{P,GFPE}, & \gamma < \gamma_{bottom} \\ L_{P,Ray Model}, & \gamma > \gamma_{top} \end{cases}. \quad (4.3)$$

In section 7.3 we will define the limits  $\gamma_{bottom}$  and  $\gamma_{top}$  of the transition region resorting to numerical results from reference test cases.

## 5 Aircraft as a Noise Source

This chapter describes the procedure developed in this dissertation regarding the modeling of an aircraft as a noise source as a means of obtaining the sound field at a receiver. The first part of the procedure is related to the determination of the sound power spectrum while the final steps consist in applying correction factors that simulate the effects of the aircraft's attitude.

### 5.1 Sound Power Spectrum

#### 5.1.1 Noise Power Distance (NPD) results

Noise certification plays an important role in an airplane design process. Therefore, several simulations and flight tests must be performed and the results must fulfill the requirements of the International Civil Aviation Organization to guarantee the airworthiness of the aircraft.

In this context the manufacturers build several tables that summarize the results obtained from the test flights. It is mandatory that the test conditions comply with those proposed in Annex 16 published by ICAO (Airbus - Flight Operations Support & Line Assistance, 2003; International Civil Aviation Organization, 2007a). These tables, containing the NPD information, are specific for each aircraft type that is airworthy and relate three different quantities: noise level, aircraft power/thrust and distance from the receiver. The information regarding each airplane is condensed into one single public database called Aircraft Noise and Performance (ANP) database (Eurocontrol, 2012; International Civil Aviation Organization, 2005).

The noise data is measured in the situation of an aircraft overfly at locations that lie underneath the aircraft's trajectory, which is regarded for modeling purposes as an infinite straight flight path, flown at constant speed and unchanging flight parameters.

The ANP database also allows the definition of the power spectrum of each aircraft and therefore one may use this information to model aircraft as a non harmonic source.

The noise-related parameter of the NPD data is the engine power setting, namely the corrected net thrust (*CNT*), chosen as the main quantity affecting the aircraft's noise emissions (Butikofer, 2006). Consequently, as the NPD results are classified according to the operating mode, departure operations are related to high power settings while approach data is associated with lower power settings. Although the *CNT* is the parameter that correlates the NPD data, it is not a quantity that drives in-flight operations. Therefore, when modeling an aircraft movement, it is necessary to assess the variables used to control the airplane, specifically the engine's low pressure rotor speed  $N_1$  (in %) or the Engine Pressure Ratio *EPR*, and convert these parameters to the associated *CNT*. As a result, one can define the *CNT* as a function of  $N_1$  or *EPR*, respectively as (European Civil Aviation Conference, 2005b; Mcaninch and Shepherd, 2011)

$$CNT = E + F \cdot V_C + G_A \cdot h + G_B \cdot h^2 + H \cdot t + K_3 \cdot \left(\frac{N_1}{\sqrt{\theta}}\right) + K_4 \cdot \left(\frac{N_1}{\sqrt{\theta}}\right)^2 \quad (5.1)$$

$$CNT = E + F \cdot V_C + G_A \cdot h + G_B \cdot h^2 + H \cdot t + K_1 \cdot EPR + K_2 \cdot EPR^2 \quad (5.2)$$

where  $E$ ,  $F$ ,  $G_A$ ,  $G_B$  and  $H$  are engine thrust constants obtained from the ANP database and  $K_1$  to  $K_4$  are correlation coefficients available in the ANP database.  $V_C$  is the calibrated airspeed (in knots),  $t$  is the ambient air temperature (in °C),  $h$  is the aircraft altitude (in feet) and  $\theta$ , the temperature ratio, is given by

$$\theta = \frac{t + 273.15}{288.15}. \quad (5.3)$$

By resorting to equations ( 5.1 ) to ( 5.3 ), it is possible to recover real in-flight parameters to feed the sound propagation schemes adopted and thus achieve more realistic computational results. The next section describes the procedure that allows the determination of the power spectrum  $L_W$  present in equation ( 1.2 ) for a constant  $CNT$  value.

### 5.1.2 Reverse engineering from NPD values

The main goal of reverse engineering the NPD data is to obtain the sound power spectrum of an aircraft for each power setting used in the noise certification stage.

This method is described in detail by Butikofer (2006) and using an Excel spreadsheet developed by Rudolf Butikofer we were able to obtain the power spectrum for different Airbus models, namely the A319/320/321, A330 and A340 families. The general guidelines used are described in the Excel program and are reproduced below:

- i. Fill in the aircraft information: number of engines, SEL from the NPD data and associated  $CNT$ ;
- ii. Specify the appropriate directivity class;
- iii. Adjust the estimated spectrum to reflect the spectral class shape of the aircraft;
- iv. Adjust the estimated spectrum to minimize the difference between the original NPD results and the ones obtained by the program calculations;
- v. Retrieve the resulting power spectrum.

The curve obtained from the spreadsheet relates the engine power spectrum with the 1/3-octave band centre frequencies studied previously in section 1.2.1.

As the determined spectra are only applicable for a limited number of  $CNT$  values, we implemented a linear interpolation algorithm for intermediate values in the computational application discussed in this dissertation (Butikofer, 2006).

## 5.2 Aircraft Attitude Corrections

In the previous chapters we have discussed the subject of aviation noise by developing a hybrid propagation method based on the combination of the GFPE method and the two ray model. We have also mentioned that both numerical schemes assume that the noise source is a monopole source and that it presents cylindrical symmetry.

In reality, aircraft are a complex noise emitter and therefore they cannot be modeled as a point source with an omnidirectional sound spreading. Consequently, the determination of the SPL at the receiver as specified by equation ( 1.2 ) must include additional correction factors that reflect the effects of lateral and longitudinal directivity of airplanes.

As both effects are affected mainly by the relative position between aircraft and receiver, as well as by the vehicle's attitude, it is necessary to unequivocally define the sound emission coordinates that represent a generic situation of aviation noise (see Figure 5.1).

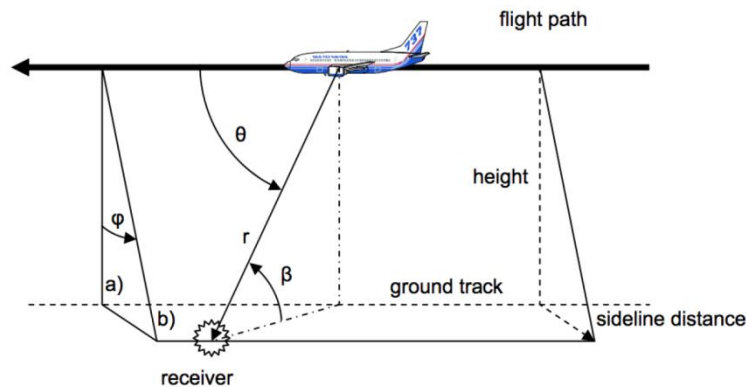


Figure 5.1 - Aircraft sound emission coordinates (Butikofer, 2006).

The spherical angles  $\theta$  and  $\phi$  are defined in relation to the aircraft, with their origin at the center of gravity of the airplane. The longitudinal angle  $\theta$  is the angle formed by the axis of flight and the vector point towards the receiver. The lateral angle  $\phi$  is defined by the following two planes: the one created by the axis of flight and the vector with downward direction perpendicular to wing plane and another plane formed by the axis of flight and the vector that connects the aircraft and the receiver.

### 5.2.1 Lateral directivity

Lateral directivity is often called engine installation effect and reflects the influence of the engine location and type on the overall directivity of the aircraft. There is a distinction between three situations:

- i. Fuselage mounted jet engines, where lateral levels decrease due to fuselage shielding;

- ii. Wing mounted jet engines, where lateral levels may increase due to wing reflections;
- iii. Propeller engines, where no correction is employed as directivity effects are negligible.

The SAE AIR 5662 (Society of Automotive Engineers, 2006) proposes two expressions that model the lateral effects of engine installation for the two first situations above mentioned. These equations are defined as follows (Butikofer, 2006; European Civil Aviation Conference, 2005b), respectively for fuselage mounted engines and wing mounted engines):

$$\Delta L_{lateral} = 10 \log_{10}(0.1225 \sin^2 \varphi + \cos^2 \varphi)^{0.329} \text{ dB} \quad (5.4)$$

$$\Delta L_{lateral} = 10 \log_{10} \left( \frac{(0.1225 \sin^2 \varphi + \cos^2 \varphi)^{0.329}}{0.8786 \sin^2 2\varphi + \cos^2 2\varphi} \right) \text{ dB}. \quad (5.5)$$

### 5.2.2 Longitudinal directivity

Longitudinal directivity is mostly influenced by the engine characteristics as the bypass ratio and the type of fan installed. Butikofer (2006) provides the value of the correction factor  $\Delta L_{longitudinal}$  as a function of the longitudinal angle  $\theta$  for different classes of aircraft as follows:

- i. Classes "d1" to "d4" refer to different generations of jet engines;
- ii. Class "d prop" is used for propeller driven aircraft;
- iii. Class "d m" is related to military aircraft.

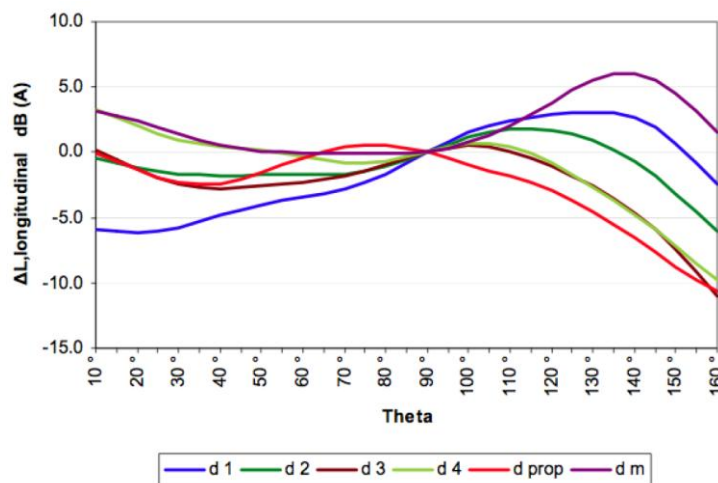


Figure 5.2 - Directivity functions for departing flights (Butikofer, 2006).

Figure 5.2 plots the values measured experimentally for flights in the vicinity of runways in the case of departure operations. For arrivals, similar classes were defined using the appropriate experimental parameters.

## 6 Program Description

This chapter is aimed towards the discussion of the computational algorithm developed in Matlab environment.

At first we explain briefly the interface between the user and the application and provide the main features that are available to the user. Afterwards we discuss the various quantities necessary to the correct operation of the implemented algorithms, namely the user defined inputs and internal application parameters. The simulation calculation stages are explained in detail by resorting to the concepts discussed in the previous chapters and the output variables available to the user are described at the end of this chapter.

### 6.1 User interface

The program discussed in this dissertation was developed in Matlab programming language and it runs on a command window environment. The computational application studies the influence of a single aircraft movement at a selected receiver's location, by using realistic parameters that define both the aircraft's trajectory and the airport scenario.

By introducing keyboard inputs the user can operate three main features:

- i. Run a new simulation;
- ii. Load an existing simulation;
- iii. Run the pos-processing functions.

The first operating mode requires the specification of several parameters specified in section 6.2 and that were defined in the previous chapters, while the process of loading an existing simulation only requires the selection of the intended aircraft movement. The last key option is only available when one of the first two was initially selected as the pos-processing functions need simulation results as an input.

### 6.2 Input parameters

As stated in the previous section, the program developed in this dissertation is oriented towards the study of aviation noise and its influence at an observer's position. Therefore, several quantities need to be defined besides the ones associated with the numerical propagation schemes that calculate the sound field. These parameters are related to the definition of the airport scenario, the acquisition of aircraft noise data and the specification of the aircraft trajectory in an adequate coordinate system.

### 6.2.1 Aircraft parameters

The aircraft related quantities are associated to the definition of the airplane as a noise source.

The noise data is loaded in the form of a data structure containing the power spectrum of the available aircraft and the application selects the appropriate information according to the aircraft used to fly the trajectory being simulated. Several engine parameters are also loaded from the ANP database as they are required to compute the variables defined in equations ( 5.1 ) and ( 5.2 ) that correlate the engine data available from in-flight recordings with the values specified by Eurocontrol (2012).

The aircraft noise data is only used by the program algorithms when calculating the lateral and longitudinal directivity correction factors as well as when determining the sound power level  $L_W$  required by equation ( 1.2 ).

### 6.2.2 Airport parameters

The computational algorithms are intended to be simultaneously used with realistic in-flight data and with an aircraft route described in Global Positioning System (GPS) coordinates. Consequently, it is mandatory to define a correspondence between this coordinate system and another that suits the generation of a two dimensional numerical grid (as in Figure 1.6).

To fulfill this need we implemented an airport database that can be updated and that defines the airport main characteristics. These quantities allow the definition of a three dimensional global Cartesian system aligned with the major magnetic directions, North and East, as well as with the vertical upward direction. The main airport parameters that need to be defined are as follows:

- i. Airport ICAO four letter identifier;
- ii. Aerodrome Reference Point (ARP) position in the GPS system;
- iii. Number of active runways;
- iv. Runway extremities in GPS coordinates;
- v. Receiver location in the GPS system (by default coincident with the ARP).

The ARP is the position used to define the geographic location of an aerodrome in the associated operational charts. As it is a key point in the airport layout we decided that this should be the origin of the global reference system  $O_{xyz}$  where the Cartesian directions  $(x, y, z)$  are respectively aligned with the Eastern, Northern and upward directions.

The specification of the active runways' information is for visualization purposes only as these parameters do not take an active part in any of the calculation stages.

We also specified a characteristic location for the receiver at each airport, which can be modified according to the user's discretion. For simplicity the receptor's location is attributed by default to the same location as the aerodrome reference point at a height of 1.2 m in order to be coherent with

the height of the microphone arrays used in the aircraft certification process (International Civil Aviation Organization, 2005).

### 6.2.3 Numerical parameters

The numerical parameters are related to the construction of the numerical grids necessary to run the GFPE method, the two ray model and the hybrid combination scheme, as described in the corresponding chapters. Therefore, the user is required to establish the value of these quantities or choose a predefined configuration proposed by the program.

The various parameters are grouped according to their application:

- i. Atmospheric information;
- ii. Ground interaction parameters;
- iii. Hybrid propagation model;
- iv. Grid generation parameters;
- v. GFPE method parameters.

The atmosphere is modeled by defining the sound speed profile, as established by section 1.2.5. We included three different evolutions of the sound speed that model a homogeneous atmosphere with a constant profile and a refracting atmosphere with a linear or logarithmic function. The user is also required to indicate the baseline atmospheric temperature for the computation of the engine coefficients (see section 5.1.1).

The ground interaction introduced in section 1.2.4 is modeled by prompting the user with multiple options of ground materials. The available materials are defined by Table 1.1 and are used as a means of obtaining a value for the effective flow resistivity, which is necessary for the determination of the normalized ground impedance.

The user is also allowed to choose the propagation method that is considered adequate for the selected aircraft trajectory so that the propagation calculations can be performed by resorting to the GFPE method, the two ray model or a combination of both (as discussed in Chapter 4).

As stated previously, the GFPE method requires the generation of a numerical grid that is based on four generic parameters, namely the length of both horizontal steps and vertical steps, the height at which the absorption layer starts and its associated thickness. As shown in the derivation and consequent studies of the GFPE method's accuracy (Cooper and Swanson, 2007; Gilbert and Di, 1993), the governing parameter for the grid generation is the wavelength and accordingly the user is asked to introduce the number of divisions  $div_r$  and divisions  $div_z$  per wavelength (here denoted  $\lambda$ ) so that the grid parameters of Figure 1.6 are defined as follows:

$$dr = \frac{\lambda}{div_r}, \quad (6.1)$$

$$dz = \frac{\lambda}{div\_z}. \quad (6.2)$$

Similarly, the absorption layer thickness is defined with relation to the average wavelength. On the other hand, the definition of the absorption layer starting height is done by resorting to the source height, as at each position the aircraft may be at a different elevation (e.g. a departure or landing procedure, where the airplane's height continuously increases and decreases, respectively). Consequently, for each aircraft position the initial height of the absorption layer  $z_{abs}$  is defined as

$$z_{abs} = n \times z_{aircraft}, \quad (6.3)$$

where  $n$  is a multiplying factor defined by the user and  $z_{aircraft}$  is the aircraft height (above ground level).

The last parameter that fully defines the numerical models implemented in this thesis is related to the GFPE method and in particular with the specification of the starting field. Following the information presented in section 2.2.1 we included two types of Gaussian fields, namely the standard version (Gilbert and Di, 1993) and the starting field proposed by Salomons (2001) and defined in equation ( 2.36 ).

#### 6.2.4 Trajectory parameters

As the simulations are intended to produce results as accurate as the propagation models allow, the aircraft trajectories are defined by relying on realistic parameters that not only describe the several geographic positions where the aircraft passes but also include performance indicators, such as the engine monitoring parameters.

Therefore, the program accepts trajectory information stored in Excel files, where each row represents a different aircraft position and each column indicates sequentially the following quantities:

- i. Aircraft GPS position: Latitude, Longitude and Altitude (in feet above mean sea level);
- ii. Aircraft Attitude: Pitch angle, Bank angle and Heading, all in degrees;
- iii. On ground indication;
- iv. Engine parameters for each engine (as defined in chapter 5);
- v. Indicated Airspeed, expressed in knots.

Additional information is retrieved from the filename of the Excel document where this information is stored, namely:

- i. Aircraft ICAO four character identifier (e.g. A320);
- ii. Airport ICAO identifier (as defined in section 6.2.2);
- iii. Type of movement: Departure, Arrival or generic;
- iv. Data recording rate: Spacing between consecutive data samples, in seconds.

Thus, it can be observed that the trajectory files aggregate all the relevant information for the simulation of sound emission by an aircraft movement thus justifying the creation of several auxiliary algorithms that preprocess the significant information and rewrite it in a format compatible with the numerical propagation schemes developed in chapter 2, 3 and 4.

## **6.3 Simulation calculations**

### **6.3.1 Program workflow**

The computational tool developed in this dissertation allows the computation of the sound field generated by a single aircraft flying a predefined trajectory by following a specific set of guidelines.

Firstly the program loads all the relevant data that is stored in several subdirectories, in detail the available aircraft trajectories (in the format specified in section 6.2.1), the airport database, the aircraft noise data and the previously saved configurations of numerical parameters. This is an important step as it prevents the user to redefine previous suitable configurations each time the program is restarted and allows access to previous simulation results in the post processing phase.

When a new simulation is started, a pre-processing procedure is required prior to any propagation calculations. This segment consists in three sequential steps suggested by the program interface.

The first step is related to the selection of the intended flight path, where the program internally links all the information contained in the several loaded databases and merges the relevant parameters into a single data structure containing the airplane's trajectory, which is written simultaneously in the global Cartesian coordinates and in the two dimensional system represented by Figure 1.6.

The ANP database contains information about several aircraft models and in certain cases the same model may be associated with different noise data according to the type of engine installed, i.e. according to its variant. We observed that for the Airbus families modeled resorting to the procedure from chapter 5 these situation occurred and thus we implemented a second stage that allows the user to choose which aircraft variant is intended when multiple options are available. This stage loads the correct sound power spectrum from the aircraft parameters database.

After both aircraft and flight trajectory are unequivocally established, it is necessary to define the numerical parameters necessary for the correct functioning of the propagation models. The user is allowed to define a new configuration of parameters or to load one from the existing listing. These parameters were discussed in section 6.2.3 and establish the miscellaneous data necessary for defining a realistic atmospheric propagation model. Also at this stage the program allows the user to indicate whether the entire frequency spectrum (in the 1/3-octave band) should be used or only a subset of it.

The previous steps formed the preprocessing stage of the numeric simulation. After the successful completion of all the mandatory data fields, the algorithm is prepared to calculate the sound

field produced by an airplane at each position of its trajectory and for each frequency belonging to the range selected by the user in the preprocessing steps.

The calculation phase starts by presenting the user an option regarding the level of use of computer memory, which is detailed in section 6.3.2. After this initial selection, the calculation stage begins and it follows a repeating sequence controlled by two main loops: the external loop covers the entire frequency range while the internal loop goes through each aircraft position of the simulated trajectory. At every iteration, the grid parameters associated with the aircraft position are loaded from the initially defined data structure and, according to the propagation scheme selected (GFPE method only, ray model only or hybrid model) and by evaluating the aircraft position (when the hybrid approach is selected), the program selects the appropriate sound propagation model to be used for that position.

The calculations using the capabilities of the GFPE method follow an iterative process consisting of the steps presented below:

- i. Calculation of the starting field using the appropriate expression (standard field or Gaussian field);
- ii. The main loop is executed, where each iteration is associated to a different range step. The vector calculated in the previous iteration is approximated by a DFT (see section 2.2.2) using the FFT numerical scheme;
- iii. The inverse Fourier transform is calculated resorting to the same FFT scheme as in the previous step;
- iv. The integral  $\Psi(r, \beta)$  is calculated using equation ( 2.41 );
- v. The final step in the loop is the calculation of the exponential factor defined by equation ( 2.49 ) and simultaneously the influence of the absorption layer is included at this stage as detailed in section 2.2.4).

The computation of the sound field by using the two ray model is based on equation ( 3.9 ) and, although the pressure level at the receiver can be readily calculated, for coherence with the results produced by the GFPE propagation method, the algorithm is applied to every point belonging to the numerical grid. When the hybrid model is selected, the algorithm applies the GFPE or the ray model if the position of the aircraft belongs to their region of validity or runs both schemes simultaneously if it detects that the aircraft lies in the transition region. Simultaneously, the pressure field of an unbounded homogeneous atmosphere is determined to be used in equation ( 1.3 ).

After all the computations are completed, the post processing becomes available and it is at this stage that the various correction terms appearing on equation ( 1.2 ) are computed.

As stated in the previous paragraph, the post processing algorithm initially computes the correction factors that are defined in equation ( 1.2 ) and that represent the geometrical spreading, the source directivity and the atmospheric absorption. The program also determines at this moment the sound power for each aircraft position from the engine thrust information provided by the input files. After these terms are calculated, the sound pressure level at each position and for each frequency

may be computed and consequently expression ( 1.7 ) can be applied as a means of retrieving the total sound pressure level at the receiver. As the pressure fields are calculated using a numerical grid, typically the receiver position does not correspond to a grid point. Therefore, we included a bilinear interpolation algorithm that detects the adjacent grid points to the receiver and extrapolates the sound pressure level at the receptor's location. The computed pressure levels are then manipulated by the post processing functions to present relevant results and noise indices as indicated by the user.

**6.3.2 Code performance optimization**

As the number of numerical simulations is dependent on both frequency range and number of aircraft positions contained in the trajectory, it can be concluded that the computational memory required to store all the relevant data may become unpractical for the average personal computer, especially when running the propagation models for high frequencies, where the numerical grid becomes denser and more grid points are generated.

Therefore, we considered relevant to develop a procedure that prevents the consumption of all available computer memory. This algorithm controls the pressure results that are saved into the data structure that gathers the important simulation data. This procedure presents four different levels (see Table 6.1):

Table 6.1 - Description of the memory usage algorithms implemented in the program

Level	Description
1	All the pressure fields are saved into a single matrix without any further action
2	All the pressure fields are saved into individual matrices
3	All the pressure fields are saved into individual matrices and the computation of equation ( 1.2 ) takes place at every iteration
4	Only the pressure field at the receiver is stored and the calculation of expression ( 1.2 ) is done at each iteration

Table 6.1 provides an overview of the four calculation modes available to the user. The first level computes the pressure fields of the entire numerical grid and concatenates them into a single matrix. This operation may produce excessively large matrices and consequently it is unsuitable for standard computational hardware. The second method computes the same pressure fields but, instead of storing them in a single matrix, it saves the simulation results in separate matrices. Although this approach prevents the excessive usage of computer memory, further improvements were introduced in the third level of Table 6.1. This alternative shares the same procedure as stage two however, at each iteration the pressure value at the observer is readily calculated and the pressure results of the numerical grid are cleared. The last development corresponds to the fourth level, where the sound field of the numerical grid is not stored. In fact, the GFPE scheme only considers the

necessary information to perform an extrapolation step and continuously clears unnecessary data until the pressure level at the receiver's location is determined.

## 6.4 Output Parameters

After the sound pressure levels at the receiver's position are calculated for the entire frequency range and for the whole aircraft trajectory, the post-processing functions become available for user interaction.

The program allows the user to view several quantities of interest when studying aviation noise that were detailed in section 1.3.3 and that are listed below:

- i. Sound pressure level time history (see Figure 1.8);
- ii. Sound pressure level time history per frequency;
- iii. Result summary including relevant acoustic data.

The sound pressure level time history graph is a curve relating the SPL at the receiver with the associated instant of trajectory. The user may choose whether this evolution is affected by the A-weighting described by equation ( 1.30 ) and if atmospheric absorption should be considered. The main difference between option i. and ii. is due to the fact that the second approach produces a surface plot as a third axis is added to the graph to translate the frequency dependence of the SPL, while the first alternative only produces a line plot describing the total sound pressure as expressed by equation ( 1.7 ).

The third option presents the user with a summary of all relevant noise metrics in a textual format and includes the minimum and maximum values of the A-weighted SPL as well as the moment they are measured. Besides these quantities, the SEL defined in section 1.3.3 is also listed.

## 7 Analysis and Results

This chapter focuses on the validation of the propagation models included in the program developed in this thesis. Therefore, at first we study the pressure field in benchmark conditions established in published literature and then we compare the obtained values from the simulations with the reference results. At the end of this chapter we define the limits of the transition region of the hybrid propagation model in order to guarantee the criteria detailed in chapter 4. This is accomplished by studying the pressure evolution in the selected reference environments.

### 7.1 Benchmark test cases

As stated in the introductory paragraph, the first part of this chapter will focus on the validation of the two propagation methods included in the hybrid model.

The GFPE method is widely used in outdoor sound propagation models and therefore several test cases were developed as a standard validation criterion. In this thesis we adopted the cases published by Attenborough et al. (1995) and that are summarized in Table 7.1 and Table 7.2.

Table 7.1 - Atmospheric refraction parameters of the three test cases for the GFPE method validation.

Test Case	1	2	3
Sound speed profiles	Homogeneous	Downward	Upward
Speed $c$ (m/s)	$c = 343$	$c = 343 + z/10$	$c = 343 - z/10$

The three test cases that allow the validation of the GFPE method consider a homogeneous atmosphere (case 1), a downward refracting environment (case 2) and an upward refracting atmosphere (case 3). The last two cases consider a linear profile similar to the one defined in equation ( 1.27 ). Additionally, Attenborough et al. (1995) propose a logarithmic evolution of the speed of sound that was not studied in this report.

Each of the three test cases presented in Table 7.1 considers a ground surface with an effective flow resistivity of  $366 \text{ kPa} \cdot \text{s}/\text{m}^2$ , a source height of  $5 \text{ m}$  and a receiver at  $1 \text{ m}$  above the ground. As studied in section 1.2.4, the ground impedance  $Z_g$  depends not only on the ground properties but on the wave frequency as well. Therefore, for each test frequency different values for the normalized impedance are obtained as shown in Table 7.2. These parameters were retrieved from the reference test conditions (Attenborough et al., 1995) where a four parameter correlation was employed (Salomons, 2001) using the following settings:

- i. Flow resistivity  $\sigma = 366 \text{ kPa} \cdot \text{s}/\text{m}^2$ ;
- ii. Porosity  $\Omega = 0.27$ ;
- iii. Pore shape factor  $s_f = 0.25$ ;

- iv. Grain shape factor  $g = 0.5$ ;
- v. Air density  $\rho_0 = 1.2 \text{ kg/m}^3$ .

Table 7.2 - Acoustic parameters for the test cases from Table 7.1.

Ground Surface	Absorbing
10 Hz	$Z_g = 38.79 + 38.41i$
100 Hz	$Z_g = 12.81 + 11.62i$
1000 Hz	$Z_g = 5.96 + 2.46i$
Source Height (m)	5
Receiver Height (m)	1

As the two ray model is only valid in a homogeneous atmosphere, where it produces an analytical solution of the wave equation, additional tests must be developed in order to validate the algorithm implemented in the developed program, as the ones used for the validation of the GFPE method are not adequate for the simplified ray model.

Therefore, we adopted three scenarios proposed by Salomons (2001) where it is possible to compare the pressure field evolutions produced by different propagation schemes, namely the GFPE method and the two ray model. These test cases consider a homogeneous atmosphere and different ground surfaces, as presented in Table 7.3.

Table 7.3 - Test conditions for the two ray model validation.

Test Case	4	5	6
Sound speed profiles	Homogeneous	Homogeneous	Homogeneous
Speed $c$ (m/s)	$c = 343$	$c = 343$	$c = 343$
Flow Resistivity $\sigma$ (kPa s/m <sup>2</sup> )	200	200	300
Frequency $f$ (Hz)	500	300	1/3 – octave band

The first validation test of the ray model (case 4) studies the pressure distribution for multiple receiver positions with constant height. In this simulation, the source is at a height of 2 m and the receiver is 50 m from the ground surface.

On the other hand, test case 5 studies the pressure evolution for multiple receivers lying on a vertical line. The pressure field is calculated assuming the same source position as in the previous case and considering that all observers are at a horizontal distance of 400 m from the source.

The last case is aimed towards the verification of the frequency influence on the implemented methods and for this reason it calculates the pressure at a single receiver considering the center frequencies of the audible 1/3-octave band. This simulation (case 6) studies the atmospheric sound

propagation originating at a source with a height of 1 m and with a receiver at different horizontal ranges at a height of 5 m from the ground surface.

For the successful completion of all the numerical calculations it is also necessary to define properly the parameters that generate the two dimensional grid necessary to implement the GFPE method. As these validation test cases do not refer to a moving source, the necessary parameters are more easily defined than the ones introduced in section 6.2.3 for aviation noise prediction. Therefore, we defined the following quantities:

- i. Horizontal range step, defined with relation to the average wavelength  $\lambda$ ;
- ii. Vertical step, also referenced to the average wavelength;
- iii. Initial height of the absorption layer  $z_{abs}$ , defined in meters;
- iv. Absorption layer thickness ( $z_{top} - z_{abs}$ ) expressed as a multiple of the average wavelength.

Table 7.4 presents the values of each grid parameter used in the several case studies adopted in this thesis and that fulfill the requirements demanded by each propagation method (Cooper and Swanson, 2007).

Table 7.4 - Numerical parameters for the test cases in Table 7.1 and Table 7.3.

Test Case	1	2	3	4	5	6
$dr$	$\lambda$	$\lambda$	$\lambda$	$\lambda$	$\lambda$	$2\lambda$
$dz$	$\lambda/20$	$\lambda/20$	$\lambda/20$	$\lambda/20$	$\lambda/20$	$\lambda/10$
$z_{abs}$ (m)	300	300	300	300	600	300
$z_{top} - z_{abs}$	$80\lambda$	$80\lambda$	$80\lambda$	$80\lambda$	$80\lambda$	$80\lambda$

The validation process of the hybrid model discussed in this dissertation includes two separate stages. The first step is aimed towards the definition of the transition region boundaries, while the second phase studies the results obtained from the application of the hybrid model and compares their evolution with the corresponding data retrieved from the GFPE method and the two ray model.

Therefore, we adopted the same atmospheric conditions as the ones established in Table 7.1 and we also used the ground properties from Table 7.2. The numerical grid for both validation stages was generated using the same numerical parameters as in test case 1 (see Table 7.4).

The main differences from the previous tests are related to the position of the source and the receiver as shown in Table 7.5.

Table 7.5 - Source and receiver conditions for the validation cases of the transition region.

Test Case	7	8
Source Height ( <i>m</i> )	25	5
Receiver Height ( <i>m</i> )	-	100
Maximum Range ( <i>m</i> )	200	200

Test case 7 is related to the definition of the transition region limits. As the merging region between the two propagation models must take into account the respective angular limitations, this validation procedure consists in plotting the pressure field along multiple radials originating from the source and comparing the results obtained with each numerical scheme for each atmospheric scenario. The main purpose of the comparison process is to define a lower limit and an upper limit for the transition zone that can be shared and be valid for all the environmental conditions tested.

Test case 8 establishes an evaluation process of the performance of the hybrid model defined by the results of test case 7 under different atmospheric conditions. This simulation plots the pressure field obtained with each individual method and with the hybrid model along a line of constant height, allowing us to observe simultaneously the behavior of the three approaches studied in this thesis.

From these last two test cases we may fully define the propagation algorithms necessary to calculate the pressure field created by a monopole source at a generic position with different atmospheric conditions.

## 7.2 Propagation models validation

### 7.2.1 GFPE Validation

In this section we study the pressure field resulting from the application of the GFPE propagation method to three different test cases that were developed as a standard in the validation of outdoor sound propagation algorithms (Attenborough et al., 1995).

Each test case followed the conditions described in the previous section and involves three distinct frequencies (10 Hz, 100 Hz and 1000 Hz) and two different ranges for the observer, namely 200 m and 2 km.

Figure 7.1 plots the pressure fields obtained with the GFPE method following the specified conditions. These results correspond to a homogeneous atmosphere above a flat ground surface and we can observe that the geometrical spreading (as defined in section 1.2.2) is the most influencing parameter in the solution, especially for short distances. As the wave frequency increases the effects of atmospheric absorption become more noticeable for long range propagation, as the shadow region, here represented by the lower limit of the vertical axis, occurs for decreasing ranges with increasing frequencies.

### Case 1

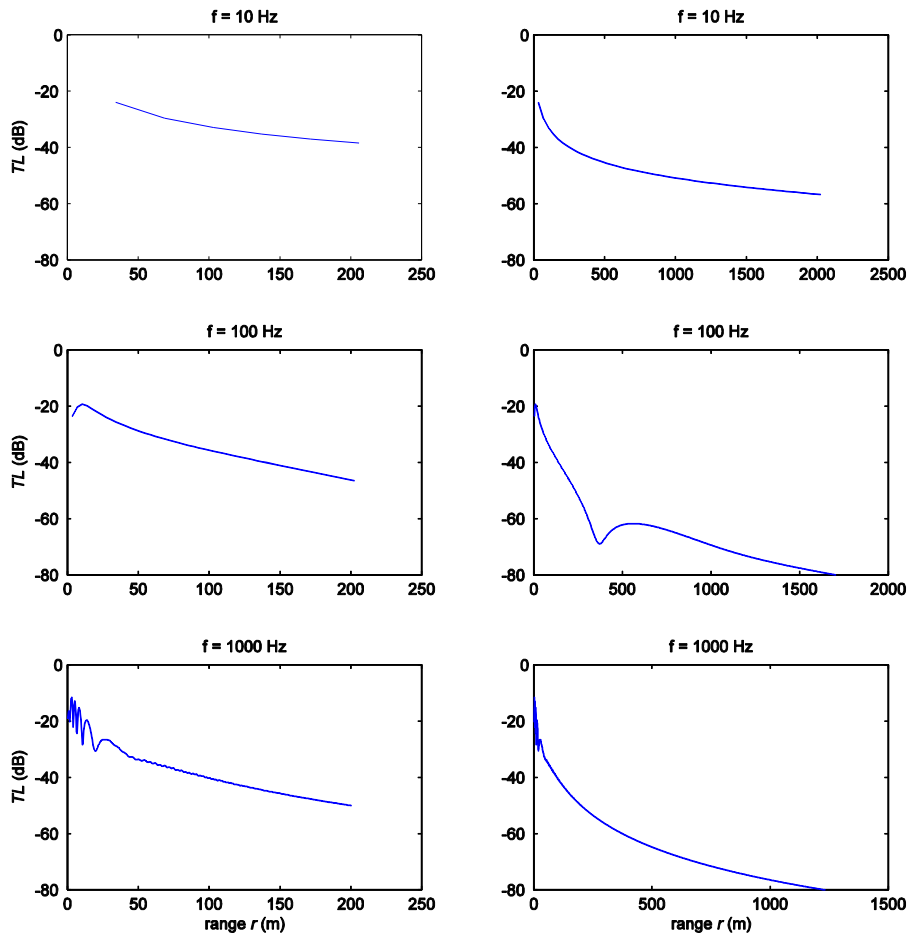


Figure 7.1 - Transmission loss up to 200  $m$  (left figures) and up to 2  $km$  (right figures) with parameters from test case 1.

The results related to case 2 from Table 7.1 are plotted in Figure 7.2 and follow an identical structure to Figure 7.1. This situation refers to an atmosphere with downward refraction imposed by a linear speed profile.

From the analysis of the results from case 1 and case 2, we can detect that for short range propagation the speed gradient does not affect the evolution of the transmission loss and therefore the conclusions from case 1 are applicable to the situation of sound propagation at small distances in a downward refracting atmosphere.

## Case 2

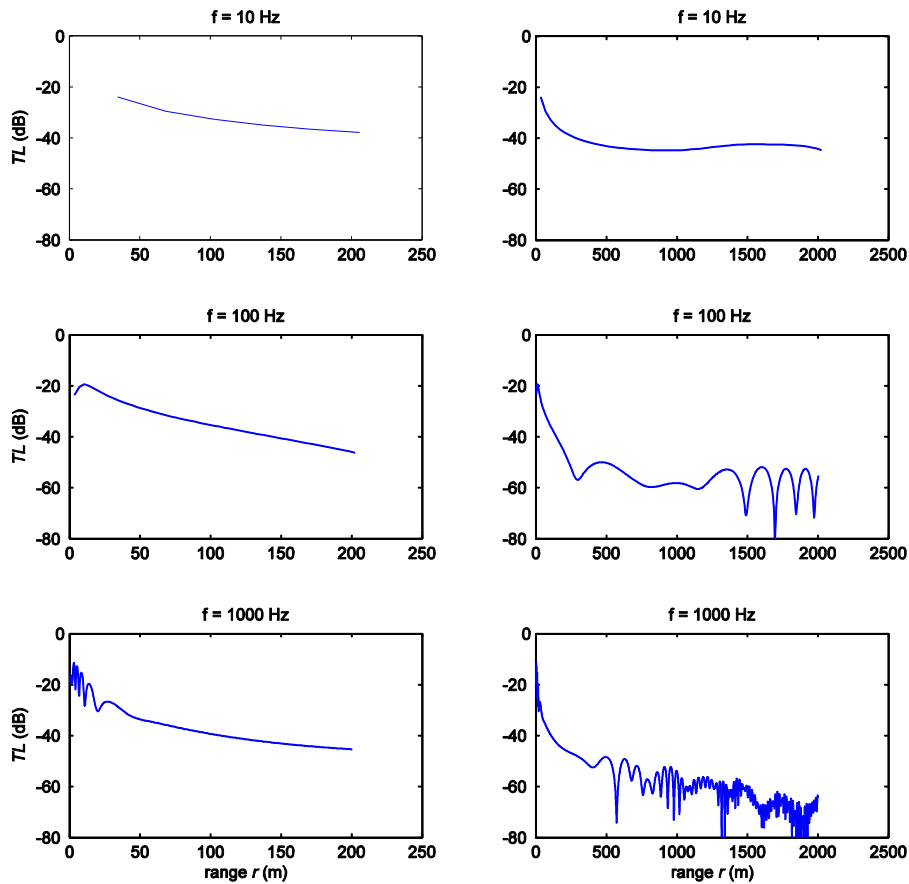


Figure 7.2 - Transmission loss up to 200 m (left figures) and up to 2 km (right figures) with parameters from test case 2.

However, for higher distances we may expect that interaction between the surface and the sound waves starts to occur as the multiple sound rays are directed towards the ground and that this phenomenon consequently becomes more significant in the transmission loss evolution. The effects of ground reflections of sound waves may be observed in the graphics on the right side of Figure 7.2 and we can verify that for increasing frequencies the ground interaction is noticeable for decreasing ranges and it appears as non periodic fluctuations in the value of the transmission loss.

Figure 7.3 represents the results obtained from the application of the GFPE method to the situation described by test case 3.

The tested environment corresponds to an upward refracting atmosphere where the sound rays are deflected away from the ground surface towards the top of the atmosphere. Therefore, we expect that the occurrence of a shadow region becomes evident particularly in long range propagation.

### Case 3

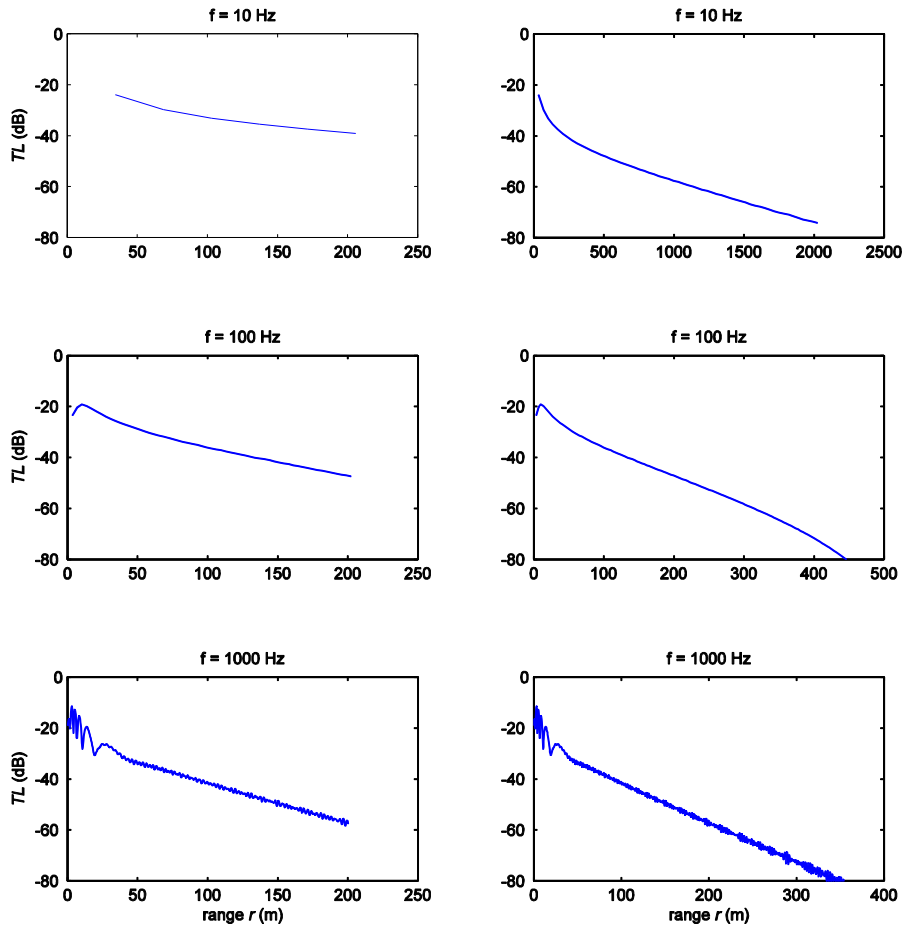


Figure 7.3 - Transmission loss up to 200  $m$  (left figures) and up to 2  $km$  (right figures) with parameters from test case 3.

Observing the graphics on the left side of Figure 7.3 we can verify that the evolution of the transmission loss follows the same trend as in test cases 1 and 2 (see Figure 7.1 and Figure 7.2 respectively), although the effects of upward refraction are visible for a wave frequency of 1000  $Hz$ , where we may detect an increase in attenuation of about 5  $dB$  at a range of 200  $m$  when compared with the corresponding results in the first test cases.

When analyzing the transmission loss behavior for higher distances, the influence of upward refraction becomes more important as the shadow region occurs for shorter ranges when compared with the data related to sound propagation in a homogeneous atmosphere (see Figure 7.1). In the first tested simulation the shadow region becomes noticeable at a range of approximately 1600  $m$  and 1200  $m$  for wave frequencies of 100  $Hz$  and 1000  $Hz$  respectively, while in test case 3 the shadow region for the same frequencies occurs at 450  $m$  and 350  $m$ .

From the analysis of the previous three figures we may affirm that the developed GFPE algorithm produces results consistent with the sound propagation mechanisms in different environments. Additionally, the results discussed in this section are similar to the benchmark cases

created as a validation baseline for propagation schemes (Attenborough et al., 1995) and we can confirm the correct implementation of the parabolic equation formulation in the program developed in this thesis. The published benchmark results are included in appendix A for comparison with the results obtained by the implemented GFPE method.

### 7.2.2 Two Ray Model Validation

As discussed in the previous section the implemented GFPE algorithm was validated by resorting to published benchmark test cases. Consequently, the results obtained with this method may be used as a reference in the validation process of the two ray model.

The three test cases used to compare the results obtained with both the GFPE method and the simplified ray model were defined in Table 7.3 and the associated figures are analyzed in this section.

Figure 7.4 presents the relative SPL as a function of range obtained using both the GFPE scheme and the two ray model in a homogeneous atmosphere. We can verify that both models agree with each other from a range of 20 m up to 100 m and that major differences are only noticeable at the first range steps, up to a range of 20 m. From Figure 7.4 we may also observe that the results are mostly coherent and that the GFPE method differs from the analytical solution produced by the ray model in the calculation of the relative SPL minimums.

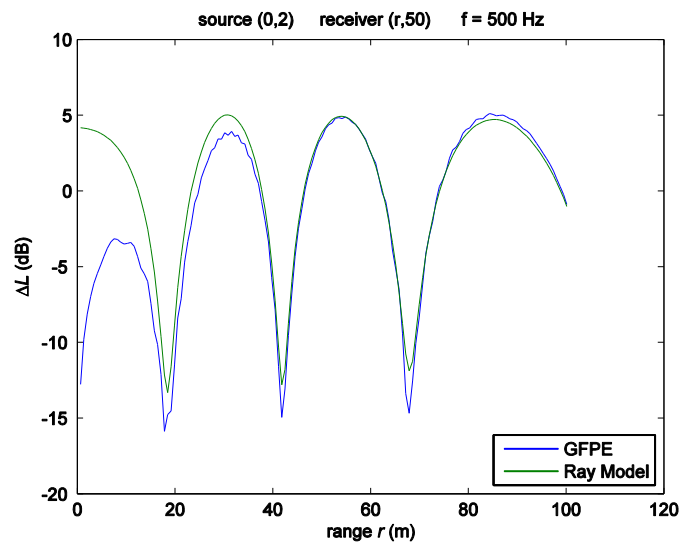


Figure 7.4 - Relative SPL as a function of range for a receiver height of 50 m.

The second test case implemented to validate the ray model consists on the computation of the relative SPL values along a vertical line and plotting them as a function of the elevation angle  $\gamma$  defined as follows

$$\gamma = \arctan\left(\frac{z - z_s}{r}\right), \quad (7.1)$$

where  $z_s$  is the source height and  $(r, z)$  are the receiver coordinates in the numerical grid reference system.

The use of the elevation angle as the independent variable is of great advantage as the angular limitations of the propagation model are more easily read than when considering the pressure results as a function of range or height.

Figure 7.5 allows the verification that from  $10^\circ$  both models produce equivalent results and as in Figure 7.4 the regions where the relative SPL local minimums occur are the ones where the differences between the two methods are greater.

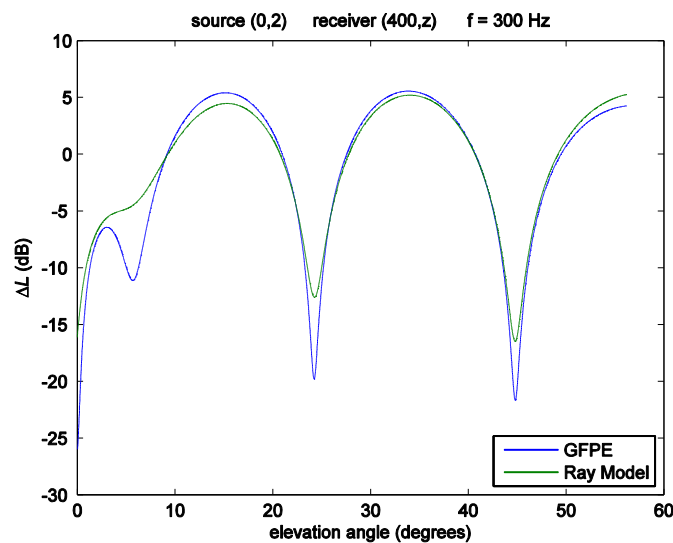


Figure 7.5 - Relative SPL as a function of elevation angle for receiver range of 400 m.

From the analysis of both graphics in the two previous figures we may detect that the differences between the two numerical schemes are mostly related to amplitude discrepancies and that there are no significant discrepancies between the phase angles of each solution.

The last validation case is oriented towards the behavior of the relative SPL at fixed locations as a function of the wave frequency, which in turn is expressed using the 1/3-octave band center frequencies (see section 1.2.1).

Figure 7.6 plots the relative SPL as a function of the wave frequency for four different receiver ranges. We may observe that for all the situations the GFPE scheme and the ray model produce the same trend. Additionally we may note that for the highest frequencies, namely above 1000 Hz, the two curves become indistinguishable and that major differences are registered for lower wave frequencies. The highest discrepancies between the two models become more noticeable for increasing distance between source and receiver up to 10 dB but when the frequency is increased these differences decay for a maximum deviation of about 5 dB.

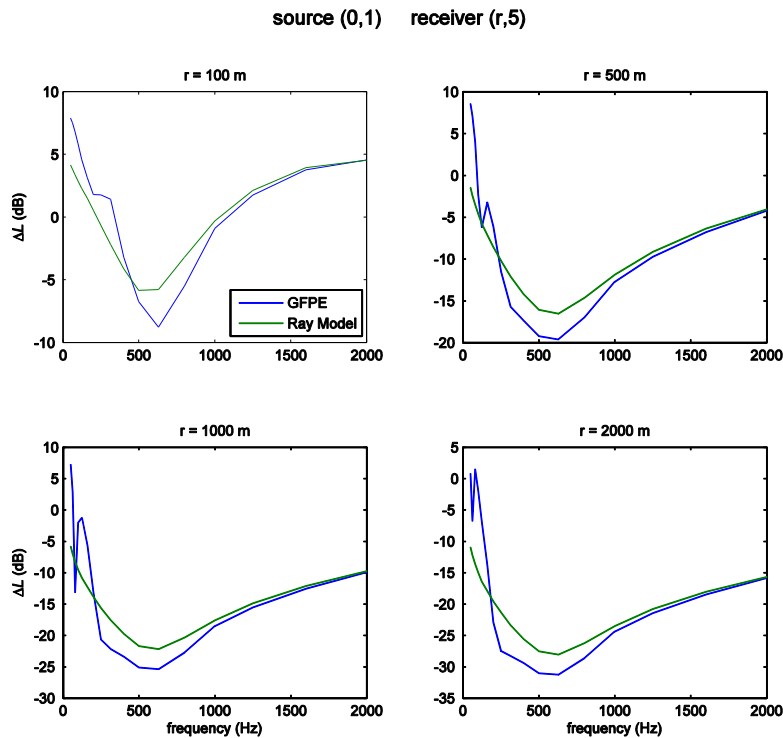


Figure 7.6 - 1/3-octave band spectra of the relative SPL computed with the GFPE method and the two ray model for a homogeneous atmosphere.

The results presented in this section compare the solutions produced when applying the GFPE method and the two ray model in different sound propagation environments. The figures related to each of the test cases show that the numerical schemes reach coherent pressure fields for a homogeneous atmosphere and indicate a correct implementation of the simplified ray model studied in this dissertation.

Although we can observe differences in the results presented in the previous figures due to the limitations of each method (as discussed in chapter 4), the curves obtained indicate that the inclusion of a transition region may produce a smooth evolution and mitigate the restrictions inherent to each model that become more important when considering atmospheric refraction.

### 7.3 Hybrid model validation

This section describes the results obtained by resorting to the test conditions defined in section 7.1. The simulations were performed in order to determine the limits of the transition region as established in chapter 4. The validation of the proposed boundaries was accomplished by comparing the pressure fields that result from the application of the three methods discussed in this dissertation, respectively in chapter 2, chapter 3 and chapter 4.

The first stage of the validation process is the determination of suitable limits  $\gamma_{bottom}$  and  $\gamma_{top}$  to apply the system of equations ( 4.3 ).

This procedure consists on the computation of the pressure field generated by a monopole source in standardized atmospheric conditions (Attenborough et al., 1995). Therefore, we adopted the parameters presented in Table 7.1 and Table 7.2, where the source and receiver positions were modified as follows from Table 7.5.

The resulting pressure field was studied by plotting the transmission loss as a function of range along a line of constant elevation angle, as defined by equation ( 7.1 ). This type of evolution is of particular interest when defining the limits of the transition region as the numerical limitations inherent to each propagation method become visible and more easily analysed.

Figure 7.7, Figure 7.8 and Figure 7.9 present the pressure field along four different downward travelling lines with elevation angles of 30°, 40°, 50° and 60°. Each figure is related to a different atmospheric setting and for each environment we varied the wave frequency as established in Table 7.2.

Figure 7.7 shows that for a non-refracting atmosphere both the GFPE method and the two ray model agree with each other for all the elevation angles and all the tested frequencies as expected. We may observe that the deviations between the two propagation methods become more visible for the highest elevation angle as it lies outside the typical region of validity of the GFPE model. For angles lower than 50° the GFPE method provides an accurate solution of the wave equation (where the exact solution is given by the ray model, which is represented by the green curve) when a suitable starting field is chosen, such as the adopted fourth order Gaussian field.

Regarding the case of a downward refracting atmosphere, shown in Figure 7.8, the differences between both models are not relevant for a wave frequency of 10 Hz. However, for the highest frequencies we may detect that for elevation angles of 30° and 60° the two formulations present discrepancies due to the fact that these angles do not belong respectively to the region of validity of the ray model and of the GFPE method. We may additionally state that for the elevation angle of 30° there is a phase difference between the two models for a frequency of 1000 Hz, thus suggesting that aside the angular limitations inherent to the propagation models, the atmospheric acoustic characteristics play an important role in the performance of the numerical methods. These differences are also identifiable for the situation of upward refraction (see Figure 7.9), where for a frequency of 1000 Hz and at an elevation angle of 30°, the major discrepancies observed in Figure 7.8 occur in an upward refracting atmosphere, although these differences are only related to amplitude shifting and do not involve phase discrepancies as in the previous case.

The results shown in these figures suggest that limiting the merging zone between elevation angles of 40° and 50° is the more appropriate choice as in the three environments these elevation angles presented the smallest deviations between the two models.

## Case 1

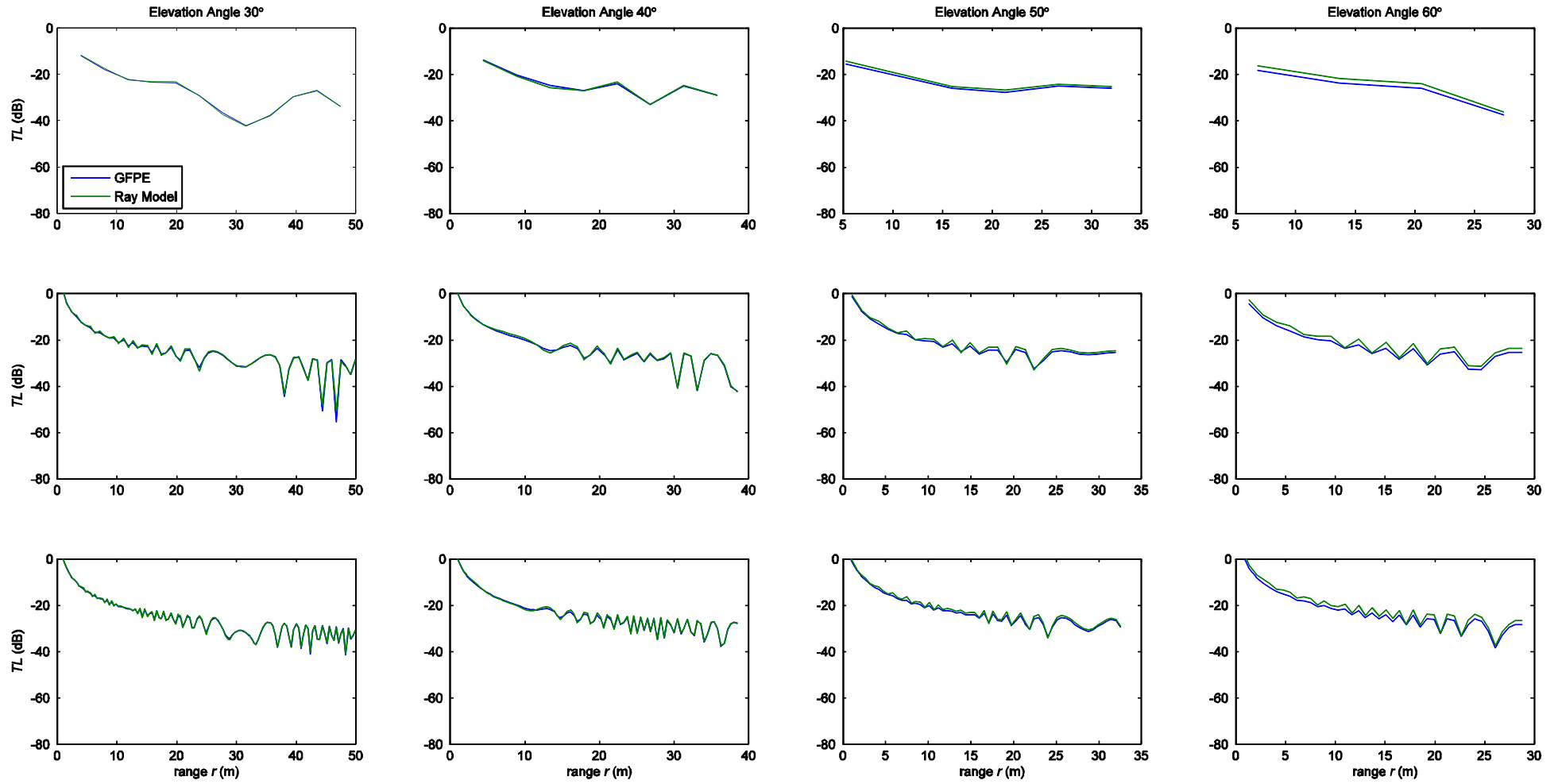


Figure 7.7 - Transmission loss along a line of constant elevation angle for a wave frequency of 10 Hz (top figures), 100 Hz (middle figures) and 1000 Hz (bottom figures) and for a non-refracting atmosphere.

### Case 2

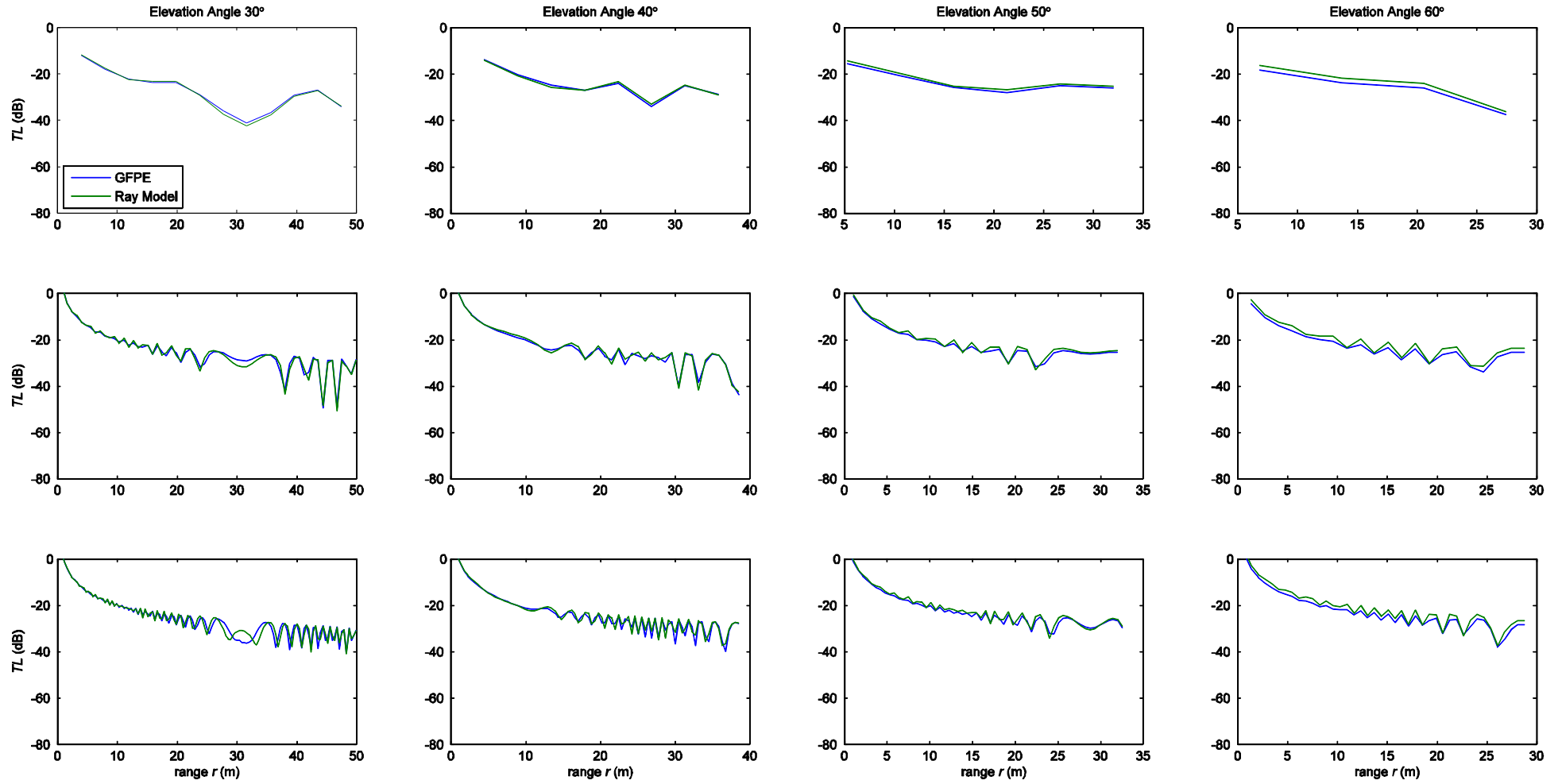


Figure 7.8 - Transmission loss along a line of constant elevation angle for a wave frequency of 10 Hz (top figures), 100 Hz (middle figures) and 1000 Hz (bottom figures) and for a downward refracting atmosphere.

## Case 3

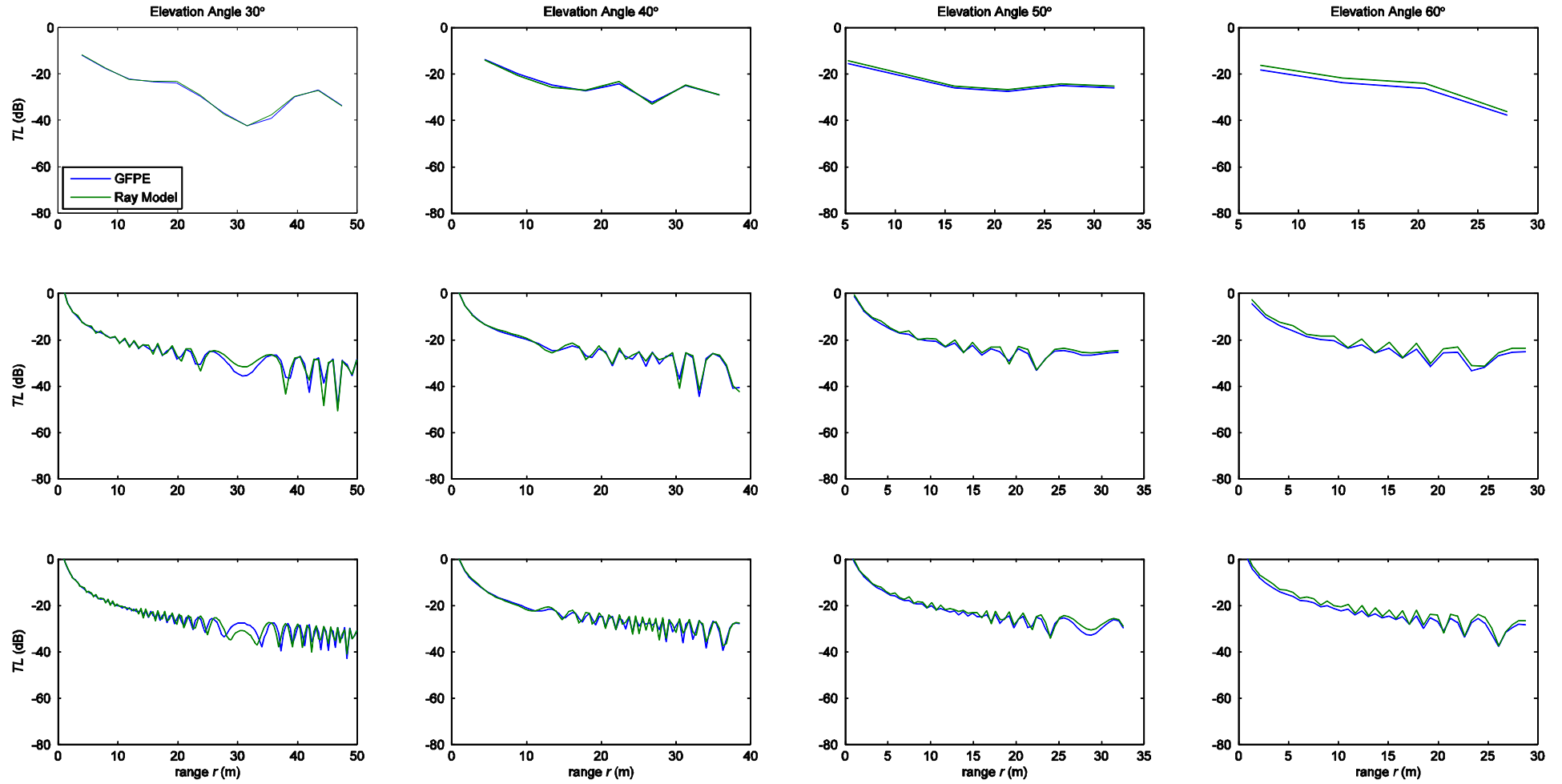


Figure 7.9 - Transmission loss along a line of constant elevation angle for a wave frequency of 10 Hz (top figures), 100 Hz (middle figures) and 1000 Hz (bottom figures) and for an upward refracting atmosphere.

After defining the boundaries of the transition region, we can now verify if the proposed limits are adequate for the benchmark test cases introduced in section 7.1.

Figure 7.10 plots the pressure field calculated using each of the three propagation models described in this dissertation in the conditions of test case 7. Analyzing the evolution of the transmission loss along a horizontal line, we may verify that the hybrid model provides, as intended, a smooth transition between the GFPE method and the two ray model for the entire frequency interval tested.

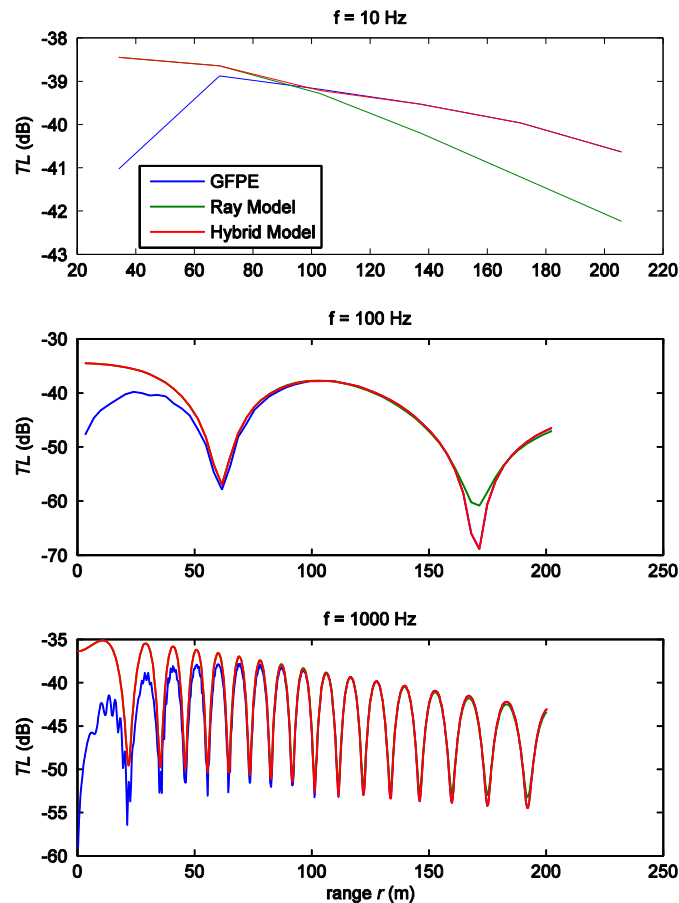


Figure 7.10 - Transmission loss as a function of range using the GFPE method, the ray model and the hybrid model, for a homogeneous atmosphere.

Observing the trend adopted by the red curve, we may detect that the hybrid model follows equation ( 4.3 ) because for short ranges, i.e. high elevation angles, the obtained function is indistinguishable from the ray model while for longer ranges the curve is coincident with the one related to the GFPE method.

Figure 7.11 presents the results for a downward refracting atmosphere, where we may verify that for the two first frequencies the hybrid model adopts a smooth trend in the merging region and in the zone of validity of each propagation method it follows the correct curve.

Unlike in Figure 7.10, in Figure 7.11 the GFPE method and the two ray model present greater deviations for increasing frequency, an effect that is observable for a frequency of 1000 Hz.

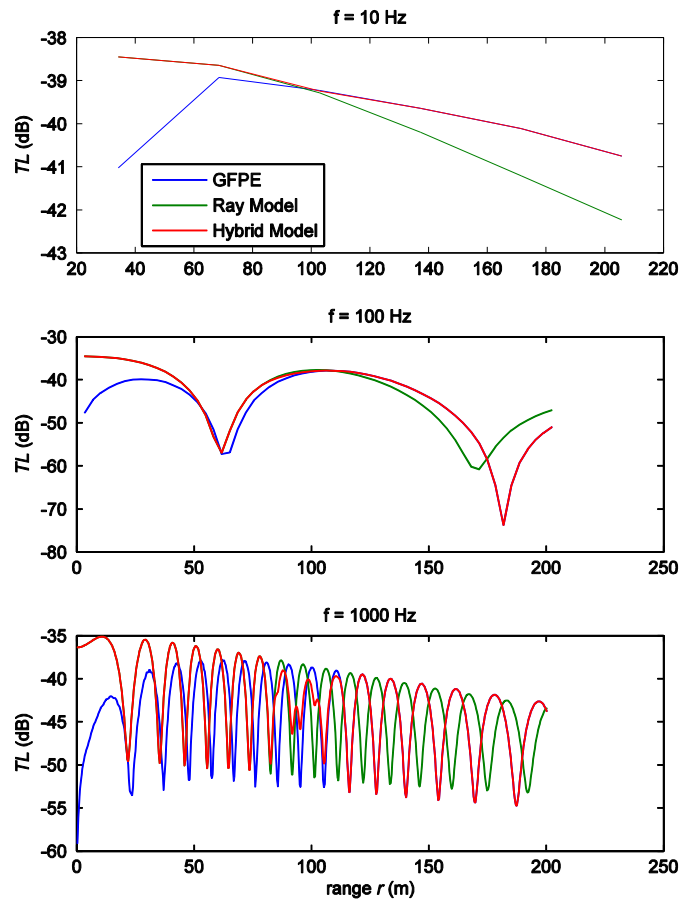


Figure 7.11 - Transmission loss as a function of range using the GFPE method, the ray model and the hybrid model, for a downward refracting atmosphere.

This situation implies that the hybrid model does not adopt a trend similar to the case of a homogeneous atmosphere, where the differences between the hybrid model and the individual propagation methods are indistinguishable. This phenomenon is not observable in Figure 7.11 due to the fact that the two base methods are shifted between each other by a phase factor. We believe that this effect is originated by the application of the two ray model to an inhomogeneous atmosphere despite being only valid for homogeneous environments. Similarly, we verified that an equivalent behavior of the hybrid model is obtained for an upward refracting atmosphere.

Although the transition stage of the hybrid model does not reflect the behavior of any of the curves obtained with the implemented propagation methods, at that region the transmission loss is delimited in a 10 dB wide band and consequently the maximum difference that can be registered between the hybrid model and the GFPE method or the ray model is 5 dB.

Therefore, we implemented the merging region using the limiting angles obtained in this section as these values are the ones that minimize the deviations between both base propagation methods in the three atmospheres tested in this chapter.

## 8 Program application to aircraft trajectories

In this chapter we apply the developed noise prediction program to the situation of airport operations by resorting to realistic trajectories and flight parameters.

### 8.1 Simulated airport scenario: case studies

#### 8.1.1 Reference conditions

As stated previously, the application of the program developed in this thesis not only requires the definition of the numerical grid but also demands the inclusion of parameters that characterize the flight path and the power spectrum of the airplane. Therefore, we simulated different standard aircraft trajectories using a commercial flight simulation tool, while adopting common conditions for all the flight paths in order to establish comparable sets of results.

The simulated trajectories are based on the Airbus A320-211, which is one of the most commonly used aircraft in real operations. As the aircraft's performance plays an important role in the flight path, it was necessary to define baseline conditions of mass and balance for all the simulations. In this context, we considered the airplane to be fully loaded where passengers and payload are concerned, with an assumed fuel distribution (in percentage of each fuel tank capacity) as shown in Table 8.1.

Table 8.1 - Fuel distribution (in percentage of fuel tank capacity) of the A320 used in the simulated trajectories.

Outer Left Tank	Inner Left Tank	Center Tank	Inner Right Tank	Outer Right Tank
10 %	20 %	20 %	20 %	10 %

Similarly, a standardized set of numerical parameters was used in order to allow a comparison between the noise indices obtained for the different simulations. In the previous chapters, we concluded that a homogeneous atmosphere promoted the best agreement between the results obtained with the GFPE method and the two ray model. Consequently, in all the simulated environments we assumed a constant speed profile and an unvarying ground surface material (see Table 8.2).

Table 8.2 - Environmental parameters for the simulated airport scenarios.

Parameter	Value
Speed of Sound ( $m/s$ )	340
Ambient Temperature ( $^{\circ}C$ )	15
Ground Surface	<i>Airport Grass</i>

Table 8.3 presents the values of the different parameters that are necessary for the construction of the numerical grid. These quantities were defined in accordance with the criteria developed for the maximization of the GFPE method accuracy (Cooper and Swanson, 2007) while reducing the computation time as much as possible.

Table 8.3 - Grid parameters for the simulated airport scenarios.

Parameter	Value
$dr$	$10\lambda$
$dz$	$\lambda/10$
$z_{abs}$	$2 \times z_{aircraft}$
$z_{top} - z_{abs}$	$300\lambda$
Starting Field	<i>Gaussian 4<sup>th</sup> order</i>

As flight trajectories in the vicinity of airports are characterized by considerable variations in the aircraft's altitude, the initial height of the absorbing layer ( $z_{abs}$ ) is defined as a function of the airplane's height (above ground level) instead of using a fixed value as in the test cases studied in chapter 7. As this approach produces small values of  $z_{abs}$  for low aircraft altitudes, the thickness of the attenuation layer ( $z_{top} - z_{abs}$ ) was increased when compared to the simulations of chapter 7 in order to guarantee a sufficient number of vertical points for the correct functioning of the GFPE method (Salomons, 2001). Simultaneously, and as the GFPE method accuracy is highly dependent on the choice of the starting field, a 4<sup>th</sup> order Gaussian field was used in all test cases.

### 8.1.2 Aircraft trajectories

The simulations studied in this section refer to realistic aircraft operating procedures based on Lisbon airport and the relevant trajectory parameters were obtained by resorting to the capabilities of a commercial flight simulation software (*Microsoft Flight Simulator X*).

The adopted procedures describe the most common trajectories that can be observed in an airport environment, namely departures and arrivals. For that reason, we included in the simulated scenarios two departure procedures and one landing trajectory using the airport's preferential runway (runway 03, North-oriented).

Commercial aviation airlines are required to follow standard authorized trajectories for each airport as flight operations are conducted under Instrument Flight Rules (IFR). Consequently, national air traffic management organizations publish and periodically update the departing and arrival procedures, denominated respectively SIDs and STARs. Following the directives of ICAO, aircraft operations in the vicinity of airports include additional information regarding noise reduction, called Noise Abatement Procedures (NAP) which may be developed for both approaching and departing routes. Typically, SID procedures are related to the lateral navigation of the airplane and do not include impositions on the climb gradient of the airplane, unless necessary for obstacle clearance or fr

traffic reasons. On the other hand, STARs establish not only the lateral navigation profile of the approach but also define the approach's vertical profile. Consequently, while NAPs may be defined explicitly in instrument approach charts by manipulating the approach slope, the inclusion of noise abatement guidelines is accomplished by establishing standard performance-based climb profiles aside from the SID charts.

Following these considerations, NAV Portugal (the Portuguese ANSP - Air Navigation Service Provider) has published in the Aeronautical Information Publication (AIP) two different NAPs for departing flights (NADP - Noise Abatement Departure Procedures) that must be followed by all commercial flights. These procedures are applied according to the certification date of the aircraft and shall be used in every Portuguese airport.

For aircraft licensed in accordance with ICAO Annex 16 Chapter 2, the following NAP should be considered (this procedure will be denominated NADP 1 throughout the remainder of this chapter):

- i. From takeoff to 1500 *ft* AGL, climb with takeoff configuration and takeoff thrust, while maintaining an indicated airspeed of  $V_2 + 10 \text{ kt}$ ;
- ii. At 1500 *ft* AGL, reduce thrust to climb setting;
- iii. From 1500 *ft* AGL to 3000 *ft* AGL, maintain climb speed of  $V_2 + 10 \text{ kt}$ ;
- iv. At 3000 *ft* AGL, accelerate to normal climb speed and follow flap retraction schedules.

For aircraft licensed in accordance with ICAO Annex 16 Chapter 3 and 4, the following NAP is applicable (designated NADP 2):

- i. From takeoff to 1000 *ft* AGL, climb with takeoff configuration and takeoff thrust, while maintaining an indicated airspeed of  $V_2 + 10 \text{ kt}$ ;
- ii. At 1000 *ft* AGL, while maintaining a positive rate of climb, accelerate to zero flap minimum safety speed ( $V_{ZF}$ ), retracting flaps on schedule and simultaneously reducing to climb thrust setting;
- iii. From 1000 *ft* AGL to 3000 *ft* AGL, continue climb at an indicated speed below of  $V_{ZF} + 10 \text{ kt}$ ;
- iv. At 3000 *ft* AGL, accelerate to normal climb speed.

Consequently, the two simulations of departing procedures followed the NAPs provided by NAV Portugal.

As the A320 is certified according to ICAO Annex 6 Chapter 3, the first simulation considered the corresponding noise reduction procedure (NADP 2), where the thrust cutback was performed at 1000 *ft* AGL. The simulation registered the relevant flight parameters from the start of the takeoff run until an altitude of 3000 *ft* AGL.

The second departure simulation replicates the first NADP. As this set of instructions is not applicable to the A320, we adopted the more generic procedure recommended by ICAO, where the

thrust cutback is done at an altitude of 800 *ft* AGL instead of 1500 *ft* as published by NAV Portugal. Similarly to the first simulation, the simulated flight was recorded from the beginning of the takeoff run until an altitude of 3000 *ft* AGL was achieved.

Finally, the simulated arrival trajectory consists in an ILS (Instrument Landing System) approach using the aircraft's auto flight system. The flight path was recorded from an initial altitude of 2200 *ft* AMSL until the complete stop of the aircraft is registered.

### 8.1.3 Simulation results

In this section we describe the results related to the aircraft trajectories established in section 8.1.2.

As explained in chapter 6, the program developed in this dissertation calculates the relevant noise indices for an aircraft movement by calculating the SPL at the receiver for each aircraft's position and for the entire 1/3-octave band spectrum. This procedure implies that for longer aircraft trajectories the number of numerical simulations may require large computation times and the use of the noise prediction program becomes impracticable.

Table 8.4 presents the computation times for each of the three simulations. The approach simulation was performed resorting to the entire frequency spectrum, while the departing procedures were studied up to a maximum frequency of 4 *kHz*. We may observe that using a subset of the entire frequency range reduces substantially the computation time required for the calculation of the noise indices of an aircraft trajectory.

Table 8.4 - Computation times for the ILS approach and the noise abatement departing trajectories.

Procedure	ILS Approach	NADP 1	NADP 2
Computation time (hours)	34.2	4.5	9.5

On the other hand, Table 8.5 shows the SEL values for each aircraft movement according to the maximum frequency used in the acoustic calculations.

Table 8.5 - SEL for the ILS approach and the noise abatement departing trajectories.

Frequency (Hz)	ILS Approach	NADP 1	NADP 2
50	56.7 <i>dB</i>	41.1 <i>dB</i>	43.4 <i>dB</i>
250	79.0 <i>dB</i>	74.6 <i>dB</i>	76.3 <i>dB</i>
1600	87.5 <i>dB</i>	83.7 <i>dB</i>	85.8 <i>dB</i>
2500	87.9 <i>dB</i>	84.6 <i>dB</i>	86.5 <i>dB</i>
3150	88.0 <i>dB</i>	84.6 <i>dB</i>	86.6 <i>dB</i>
4000	88.0 <i>dB</i>	84.7 <i>dB</i>	86.6 <i>dB</i>
10000	88.3 <i>dB</i>	—	—

Analyzing the information presented in Table 8.5, it is possible to verify that limiting the frequency range of the simulations to a maximum frequency of 4 kHz produces the same results as the entire 1/3-octave band, as the variations in the SEL at the receiver are negligible from 1.6 kHz up to 10 kHz. This phenomenon is due to the absorption of the highest frequencies by the atmosphere which attenuates the corresponding pressure levels. For that reason, we truncated the frequency range at 4000 Hz for the simulations studied in the remainder of this section as the SEL values are conserved while the computation time is reduced significantly. In section 8.2, the frequency range was limited to a maximum frequency of 3150 Hz for all simulations.

As described previously in section 8.1.2, the arrival trajectory followed the ILS glide slope. The noise propagation calculations assumed a fixed receiver located at a distance of 2 km before the runway threshold and aligned with the runway centerline. This geographic position was chosen in accordance to the noise certification regulations established in ICAO Annex 16 and it is established precisely in appendix B along with the receivers that are addressed in the remainder of this chapter.

Figure 8.1 represents the SPL and the distance between the aircraft and the receiver as functions of time. The time evolution of both quantities suggests that the distance between the source and the receiver is the governing parameter of the SPL at the receiver.

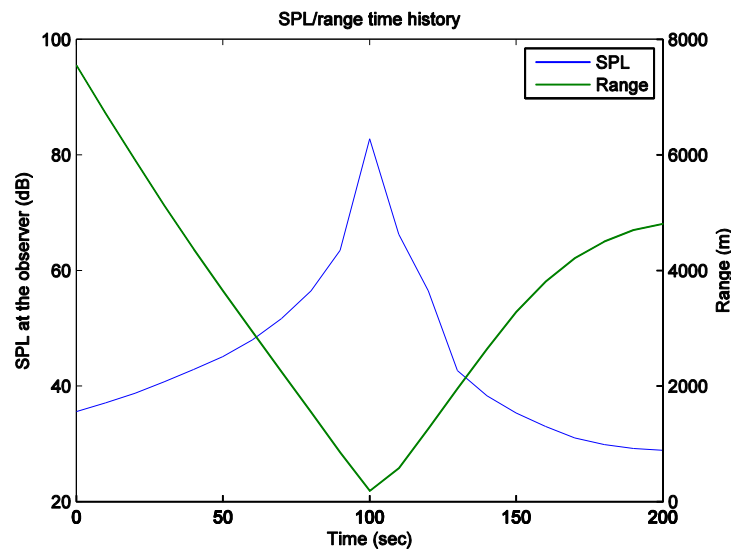


Figure 8.1 - SPL and range time history for the ILS approach simulation.

The integration of the SPL curve as established by equation ( 1.32 ) provides the SEL ( $L_{AE}$ ) of the entire aircraft movement. From the previous figure, we may observe that the relevant sound energy for the 10 dB-down integration (see section 1.3.3) is concentrated around the maximum SPL value and that most of the aircraft's trajectory is not considered in the calculations due to rapid evolution of the SPL curve at the vicinity of the maximum.

Table 8.6 shows the relevant parameters of the approach simulation, namely the maximum SPL at the receiver and the SEL value from the entire trajectory based on the computation of equation ( 1.32 ).

Table 8.6 - Maximum SPL and SEL for the ILS approach simulation.

Parameter	Value
Maximum SPL	82.8 dB(A)
$L_{AE}$	88.3 dB

Additionally, the numerical results obtained from the hybrid model calculations of the approach trajectory may be compared with the experimental results obtained by Correia (2011). Table 8.7 presents the SEL values obtained from experimental measurements (Correia, 2011) using a sound meter at a fixed location. The measuring equipment was placed near Campo Grande (Lisboa) and it can be verified that this position is coincident with the one assumed in the numerical calculations. Consequently, and while considering the limitations of the sound propagation program, both results may be compared as they describe the same aircraft movement and are related to a common receiver position.

Table 8.7 - SEL from numerical calculations and experimental measurements for the ILS approach in a homogeneous atmosphere.

Experimental (dB)	Numerical (dB)	Deviation (dB)
90.99	88.30	2.69

From Table 8.7, we may conclude that the numerical methods produce coherent results with the experimental data as the deviation between both sets of values is acceptable. Additionally, and as the measuring equipment allowed the determination of the frequency distribution of the SEL, we can observe that the frequency spectra obtained using the numerical model follows a trend similar to the experimental evolution (dark blue, green and red curves in Figure 8.2), where it can be observed a decay for the highest frequencies (see Figure 8.2 and Figure 8.3).

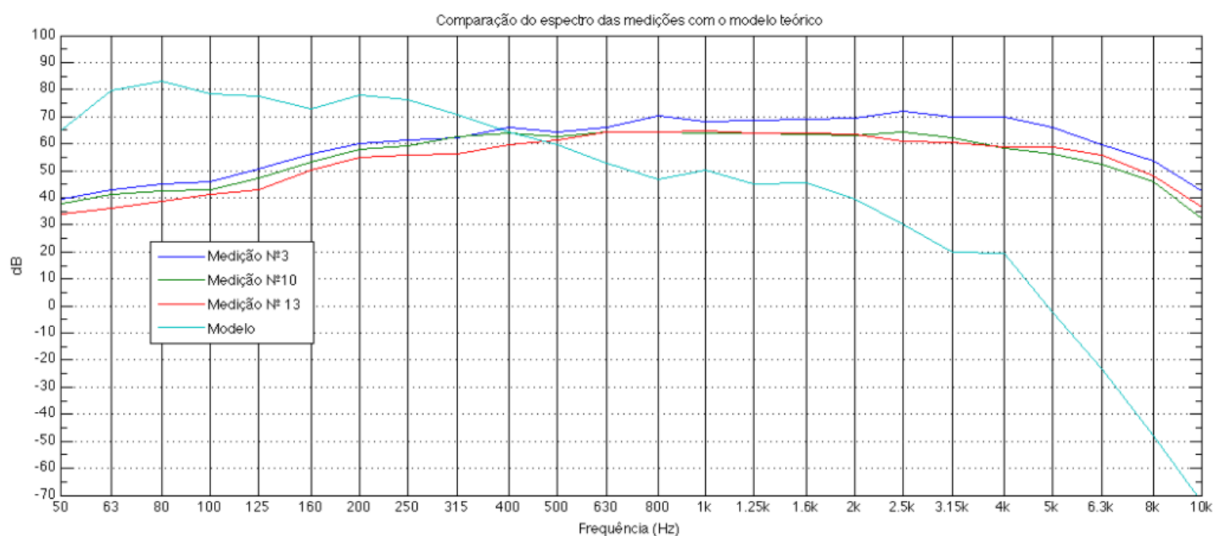


Figure 8.2 - Experimental SEL spectrum for the approach simulation (Correia, 2011).

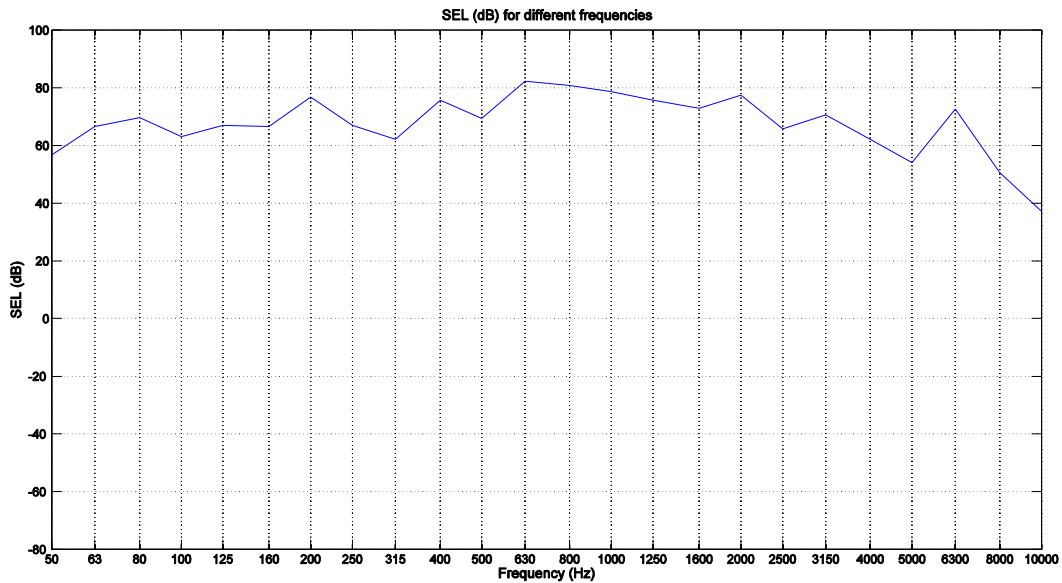


Figure 8.3 - Numerical SEL spectrum for the approach simulation.

In order to assess the influence of atmospheric refraction on the SEL perceived by the receiver, we simulated the landing trajectory in conditions where atmospheric refraction is expected. In this context, we adopted the same speed profiles of the validations cases 2 and 3 (see Table 7.1), and that are characterized by a linear evolution of the sound speed with height, as established in Table 8.8.

Table 8.8- Atmospheric refraction parameters for the ILS approach in refracting conditions.

Refraction	Downward	Upward
Speed $c$ (m/s)	$c = 343 + z/10$	$c = 343 - z/10$

Figure 8.4 represents the SPL and the distance between the aircraft and the receiver as functions of time considering the effects of downward (left graphic) and upward (right graphic) refraction.

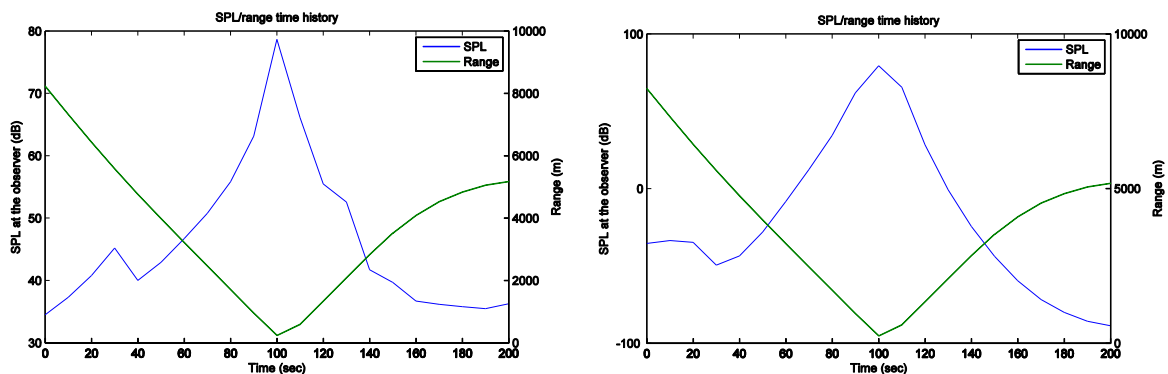


Figure 8.4 - SPL and range time history for the ILS approach simulation in a downward refracting atmosphere (left figure) and in an upward refracting atmosphere (right figure).

Similarly to the approach simulation in a homogeneous atmosphere, both trends suggest that the governing parameter of the SPL at the receiver is the distance between the source and the observer.

The SEL numerical results associated with the conditions described previously are presented in Table 8.9 and are compared with the experimental data published by Correia (2011).

Table 8.9 - SEL from numerical calculations and experimental measurements for the ILS approach in refracting conditions.

Experimental ( <i>dB</i> )	Downward		Upward	
	Numerical ( <i>dB</i> )	Deviation ( <i>dB</i> )	Numerical ( <i>dB</i> )	Deviation ( <i>dB</i> )
90.99	85.4	5.59	85.5	5.49

The results show that both atmospheres produce equivalent results in terms of the Sound Exposure Level. This phenomenon may be justified by the fact that, although an upward refracting atmosphere reduces the SPL at the receiver, its action influences the positions associated with low elevation angles, while for higher elevation angles this effect becomes negligible. By observing Figure 8.4, we may verify that both cases present a maximum SPL of approximately 80 *dB*, which occurs for the minimum distance between the source and the receiver. This figure also shows that in an upward refracting atmosphere, the SPL levels are more attenuated for larger distances when compared with the equivalent positions in a downward refracting environment. As the SEL is obtained from the 10 *dB*-down integration, the fact that both curves exhibit the same maximum justifies the similarity between the results in these two test cases. Simultaneously, we may verify from Table 8.9 that both results are coherent with the reference data and that the deviation from the experimental results are acceptable. The differences obtained from the results associated with a homogeneous atmosphere suggest that the choice of an adequate speed profile may become important when studying complex atmospheric conditions, such as strong winds and temperature gradients.

Regarding the departing simulations, we obtained the time history curves of the SPL at the receiver and compared its evolution with the power setting used at each moment and, similarly to the approach simulation, with the distance between the aircraft and receiver. The receiver was placed at a distance of 6.5 *km* from the beginning of the takeoff roll and aligned with the runway centerline extension, following the directives of ICAO Annex 16.

Figure 8.5 plots simultaneously the SPL at the receiver and the distance travelled by sound waves as functions of time for both NADPs (see section 8.1.2) and, on the other hand, Figure 8.6 establishes the same relation between the SPL at the observer and the thrust setting used throughout the duration of the departing procedures. This set of figures shows that both parameters plotted against the evolution of SPL at the receiver affect the latter quantity. In fact, we may observe in Figure 8.6 that the power cutback at each NADP results in a reduction of the pressure level at the receiver, suggesting that the selection of adequate thrust reduction altitudes may become relevant for the reduction of the overall SEL, as it may narrow the SPL values that are within the 10 *dB*-down integration region. Similarly, it can be verified that the distance travelled by sound waves also governs

the magnitude of acoustic pressure (as in Figure 8.1) where for increasing distances the value of the SPL is reduced whereas for shorter ranges the SPL increases.

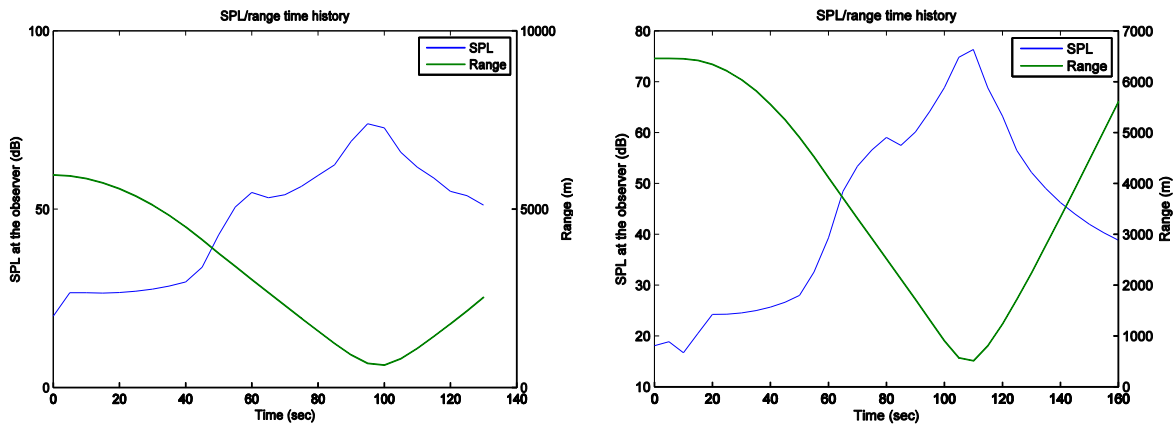


Figure 8.5- SPL and range time history for NADP 1 (left figure) and NADP 2 (right figure) departing procedures.

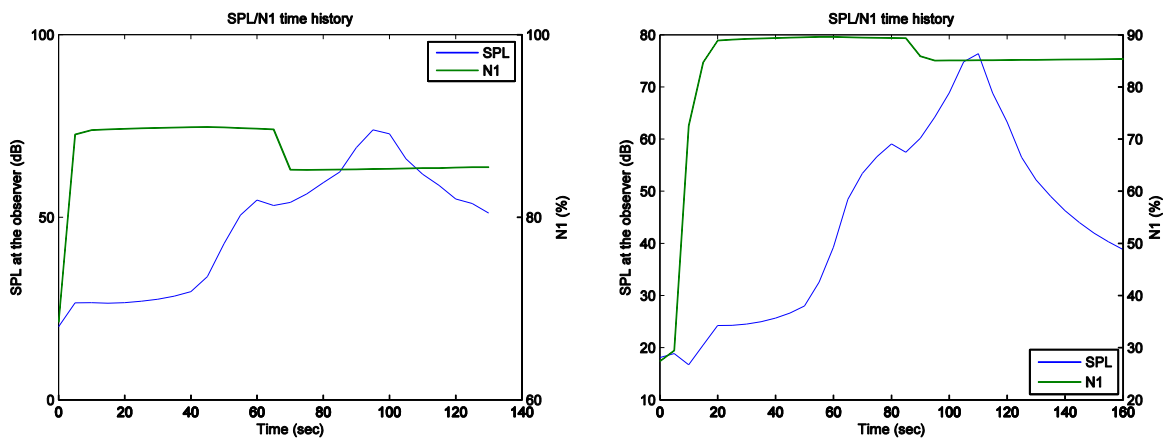


Figure 8.6 - SPL and engine thrust time history for NADP 1 (left figure) and NADP 2 (right figure) departing procedures.

The application of equation ( 1.32 ) allows the determination of the SEL values for each departing procedure and for the specified receiver location, which are presented in Table 8.10.

Table 8.10 - SEL from numerical calculations for the departing procedures.

Procedure	NADP 1	NADP 2
SEL (dB)	84.7	86.6

Table 8.10 shows that both trajectories produce equivalent values of SEL at the selected location. Additionally we may detect that the first procedure is more suitable for noise reduction at the tested receiver. Despite these conclusions, it is important to note that actual evaluations of noise exposure to aviation noise are performed by resorting to multiple ground stations as a single observer is not a sufficient indicator regarding the noise impact of aircraft operations.

Having established that the main parameters affecting the evolution of the pressure field at a generic receiver are the propagation distance and the power cutback moment, we focused on the validation of the hybrid model in departing scenarios.

In his context, we resorted to real in-flight data from a departing trajectory operated by an Airbus A320 and used these parameters to obtain the numerical noise indices from the hybrid propagation model. The results obtained using the computational tool were compared with the measurements from the monitoring ground stations installed in the vicinities of Lisbon airport at two different locations, namely at the airport itself and at Camarate (Lisboa). Table 8.11 and Table 8.12 present respectively the SEL and the maximum SPL obtained from the numerical simulations and from the monitoring equipment.

Table 8.11 - SEL (dB) from numerical calculations and experimental measurements for the departing procedure.

Location	Experimental (dB)	Numerical (dB)	Deviation (dB)
Camarate	89.8	89.5	0.3
Airport	92.4	91.0	1.4

Table 8.12 - Maximum SPL (dB) from numerical calculations and experimental measurements for the departing procedure.

Location	Experimental (dB)	Numerical (dB)	Deviation (dB)
Camarate	81.3	80.7	0.6
Airport	84.9	80.9	4.0

Analyzing the results presented in both tables, we may verify that the numerical and the experimental results are equivalent in terms of Sound Exposure Level and maximum Sound Pressure level, which is demonstrated by the low absolute deviation between these quantities. Therefore, we may conclude that the hybrid propagation model discussed throughout this dissertation is also adequate for departing scenarios as it is coherent with the data used to evaluate airport noise of real aircraft operations.

Consequently, and recovering the conclusions that resulted from the landing simulation, it can be stated the hybrid propagation model may be used to predict aviation noise in the vicinity of airports that is created by departing and arriving aircraft, as the numerical results are equivalent to experimental data obtained in both situations.

## 8.2 Review of noise abatement procedures

In this section we adopt five different noise abatement procedures for departing routes published by ICAO (2007b) as a summary of the typical trajectories adopted by air carriers for noise reduction in the vicinity of airports.

Similarly to the procedures studied in section 8.1, the simulations resorted to the conditions established in section 8.1.1.

Departing procedures are defined by three distinct moments, the first being related to thrust reduction from takeoff setting to climb thrust, and the second stage associated with flap retraction, while the last moment consists in the acceleration to climb speed. Table 8.13 presents the altitudes (in feet above ground level) for each of the three stages referred in this paragraph.

Table 8.13 - Definition of the takeoff stages (in feet AGL) for the NADP published by ICAO (2007b).

	Case 1	Case 2	Case 3	Case 4	Case 5
Thrust Reduction	800	800	1000	1500	1500
Flap Retraction	1500	800	1000	1500	3000
Acceleration	3000	3000	2500	1500	3000

Following the procedures established in Table 8.13, we may obtain the evolutions of two important parameters as functions of distance to the beginning of the takeoff roll. These quantities are the engine thrust and the distance between the aircraft and the receiver (see section 8.1.3) and are plotted in Figure 8.7.

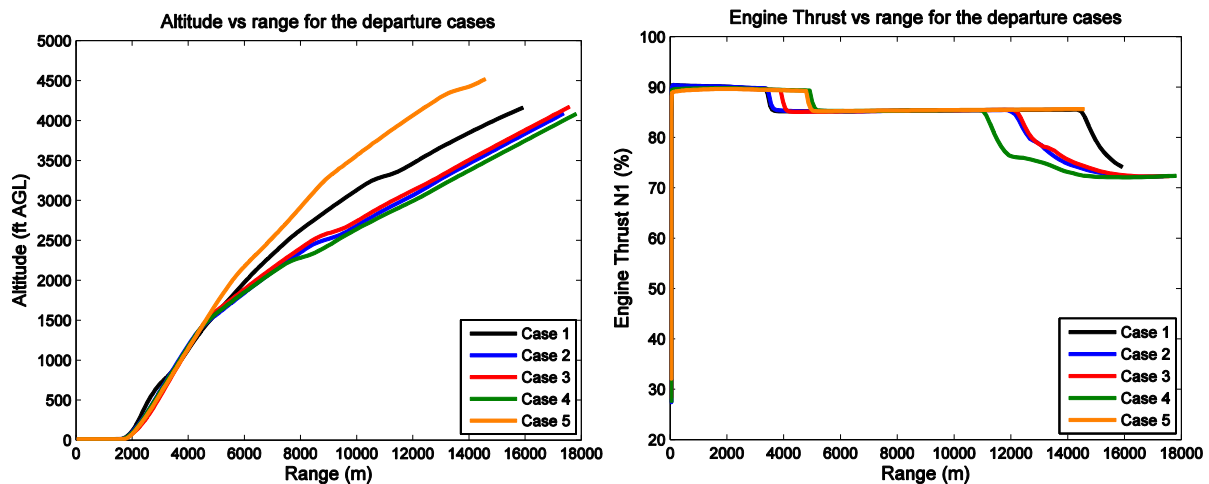


Figure 8.7 - Altitude (left figure) and engine thrust (right figure) as functions of distance to the start of takeoff roll.

Observing the right graphic of Figure 8.7 we may observe that the first thrust reduction is related to the selection of climb power, while the second reduction to a value of 70% reflects the moment when the aircraft reaches the adequate climb speed. As the initial climb segment is flown at

an indicated airspeed of  $V_2 + 10 kt$  up to the first power cutback, it can be verified that performing the thrust reduction and acceleration stages earlier corresponds to a shallower vertical profile, as in test cases 2 and 3 (see left graphic in Figure 8.7). On the other hand, if these tasks are postponed, the resulting trajectory will involve steeper climb gradients, as it can be observed for test case 5.

As these procedures involve different schedules of the major three actions when referring to noise reduction, it is important to study the overall spatial distribution of the sound levels in terms of the sound exposure level.

For that reason, we simulated the five aircraft trajectories defined in Table 8.13 and Figure 8.7 by resorting to the capabilities of the two ray model. The sound levels were computed for a grid of receivers that were defined in the global Cartesian system (which is defined in section 6.2.2). As the number of receivers may become considerable for a finer grid, the use of the two ray model is of great advantage, as it provides an estimate of the sound levels in the vicinity of airports for a multitude of receivers without penalties in the computation time required for the calculations.

Figure 8.8 represents the noise maps associated with each of the departure cases studied in this section, where the noise contours are related to different values of the sound exposure level of the trajectory. From the various noise maps, we are able to study qualitatively the distribution of sound intensity regarding two axes, the first being aligned with the runway's centerline and the second in a direction perpendicular to that direction.

At first, we may verify that in the vicinity of the airport's runway all the noise abatement procedures present similar noise contours and that major differences are only detected for larger distances to the airport. It can also be observed that before the rotation of the aircraft and the consequent beginning of flight the noise contours are parallel to the runway. From the moment the aircraft starts to fly, a lateral spreading of the noise levels is detectable, which is expected as the airplane is continuously increasing its distance to the ground surface. We can also observe that this lateral spreading of the SEL values is related to the climb gradient of each trajectory. For example, the first and last procedures (cases 1 and 5) present greater lateral spreading in the beginning of the trajectory, as seen in Figure 8.8 a) and e), when compared to the remaining test cases. Simultaneously, as test cases 1 and 5 are associated with higher climb gradients, we may detect that the noise indices for larger distances become smaller due to the larger altitudes reached in these situations. This effect is perceptible in the upper part of the maps in Figure 8.8 by noticing that the noise contours start to close for the first and last procedure, while for the other trajectories this behavior is not detected.

Although the application of the ray model provides an estimate of the noise evolution in the areas adjacent to the airport without increasing the computing time, it should be noted that the hybrid model developed in this thesis should be applied when studying the noise impact of an operational procedure for an individual location as it provides more accurate results for refracting atmospheres.

In order to assess the effect of each of the procedures established in Table 8.13 on locations close to the airport, we employed the capabilities of the hybrid propagation model to two different locations. This analysis also intends to verify the influence of the different schedules in the noise levels for each location.

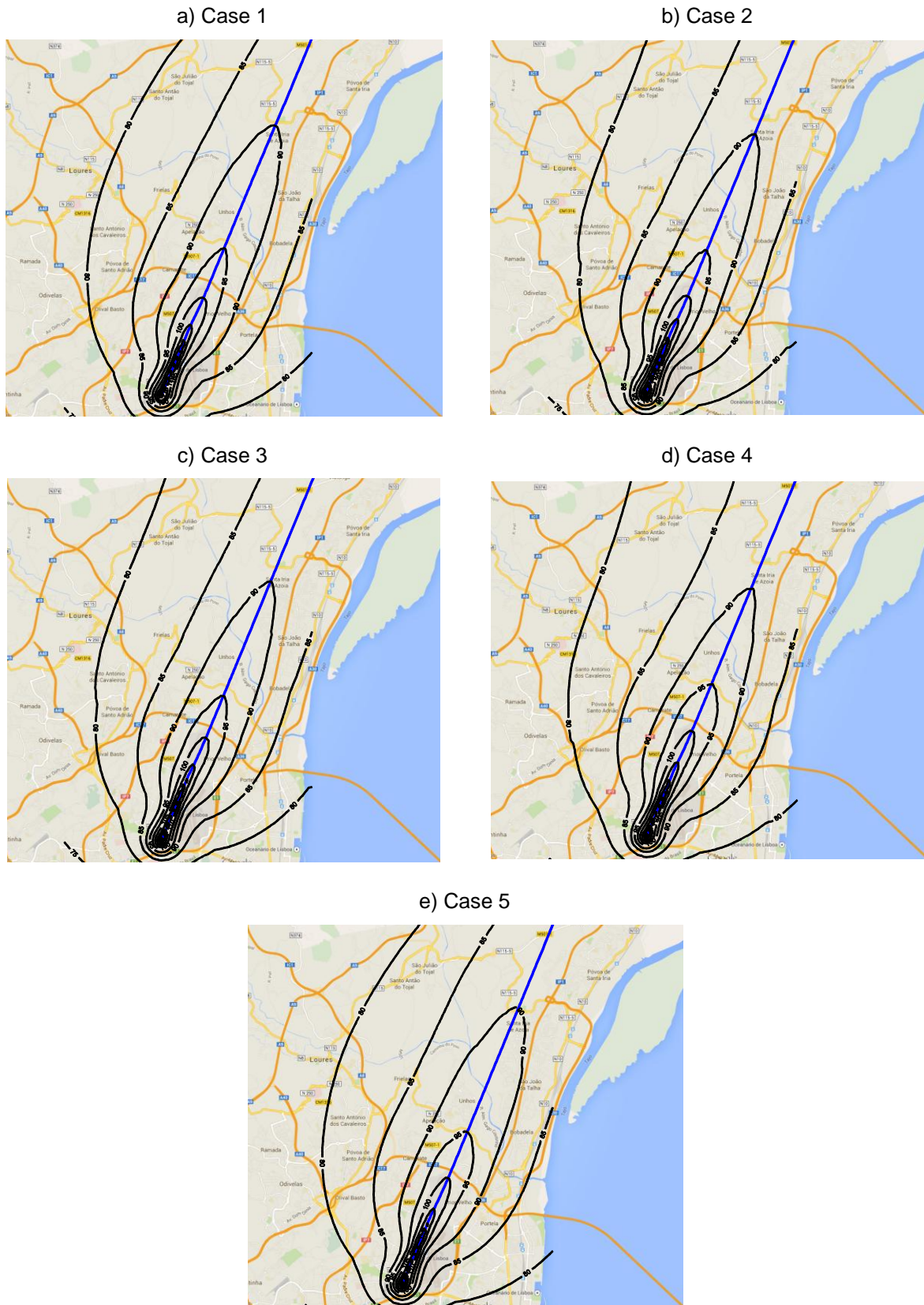


Figure 8.8 - Noise maps for the departure test cases of section 8.2, representing the aircraft's trajectory (blue line) and the SEL (in dB) contours (black lines).

By resorting to the same numerical parameters as in section 8.1, we obtained the SEL values (in dB) for two different receiver positions, presented in Table 8.14. The first receiver position is located at a distance of 6.5 km from the beginning of the takeoff roll and aligned with the runway extended centerline. In order to establish the influence of thrust reduction after passing by the receiver's location, a second observer was placed along the runway extended centerline at a distance of 5 km from the start of the ground roll. As in section 8.1, these positions are defined more accurately in appendix B.

Table 8.14 - SEL (dB) for the reviewed departing procedures and for each receiver position.

	Case 1	Case 2	Case 3	Case 4	Case 5
Receiver 1	85.7	86.2	86	86	85.5
Receiver 2	87.6	88.5	88.1	90.2	90.5

From the results obtained, we may observe two different trends regarding the minimization of aircraft noise at specific locations.

For larger distances, corresponding to receiver 1, we may observe that the SEL values are similar for all the trajectories. We can additionally verify that the highest values correspond to the procedures with minimum climb gradients, namely cases 2 to 4.

In the situation of shorter distances from the beginning of the takeoff roll, which are related to the position of receiver 2, we may detect that the SEL values are increased by 2 dB in test cases 1 to 3, when compared with the corresponding results for receiver 1. However, for the last cases, the increase in SEL is approximately 5 dB. From Figure 8.7 it can be shown that for the second receiver, procedures 4 and 5 reduce to climb thrust at a range of 6 km, i.e. after passing by the observer, while the remaining trajectories take this action before reaching the receiver. Therefore, the results suggest that observers closer to the airport are more sensitive to the schedule of thrust reduction, which is corroborated by the 5 dB penalty for the last cases and by the fact that up to a range of 5 km all the trajectories exhibit the same initial climb segment (see the left graphic of Figure 8.7).

Consequently, we may conclude that the determination of a noise abatement trajectory is closely related both to the region where the sound levels are to be minimized and the position of such zone with relation to the airport. Therefore, the results obtained for the five procedures reviewed (International Civil Aviation Organization, 2007b) suggest that in order to minimize the impact of departing aircraft near the airport, engine thrust should be reduced to climb setting before reaching the observer, as seen for the first test cases when studying the first receiver. On the other hand, when reducing the noise indices in regions that are far from the runway, it can be verified that the aircraft should adopt a trajectory that increases the minimum distance between the airplane and the receiver. To fulfill that objective, the power cutback action may be delayed to allow a longer climb segment at a higher gradient without penalties in the sound exposure level, as demonstrated in case 5 for the first receiver.

## 9 Conclusions and future developments

The increasing air traffic volume registered in recent years, which is accompanied by a growing environmental awareness, has led to a review of existing noise legislation by international aviation regulators. Therefore, it was necessary to implement noise reduction policies in different areas associated with commercial aviation, thus combining the efforts of aircraft manufacturers, airlines and airport authorities.

In this context, several noise prediction tools have been developed as an alternative approach to expensive flight experiments. As computational resources continue to evolve, these prediction tools are required to include more complex and realistic propagation models while still being able to provide the required results in the shortest amount of time, in order to enable their application in operational environments.

In this dissertation we developed a noise prediction program oriented towards aviation noise in the vicinity of airports using Matlab programming language. This computational tool includes not only physics-based atmospheric propagation methods but also adopts empirical models that allow the definition of aircraft as complex noise sources.

The numerical schemes used to calculate sound propagation in the atmosphere were the Green's Function Parabolic Equation (GFPE) method and the two ray model. These methods were combined into a hybrid model, in order to mitigate their limitations and maximize their potential. As seen in chapter 4, the limitations of both methods are related to the relative position between source and receiver. It can be shown that the ray model is well suited for higher relative positions of the sound source, while the GFPE method is more accurate in the opposite situation. Therefore, the two models were merged by resorting to a linear interpolating transition region as a means of assuring a smooth transition between the results produced by each method.

In chapter 5 we presented the procedure adopted to define the aircraft as a noise source. As the propagation methods described previously assume a harmonic monopole source, it was necessary to calculate the aircraft's sound power spectrum by using the center frequencies of the 1/3-octave band and by employing a reverse engineering procedure based on the noise certification measurements. Simultaneously, the effects of the interaction between sound waves and airframe, as well as the influence of engine directivity and aircraft's attitude, were included in the noise model by resorting to published empirical correlations that are applied as correction factors to the sound pressure level at the receiver.

The propagation methods were validated using benchmark test cases that are accepted as a standard in the verification of atmospheric sound propagation models. The adopted procedure involved three different stages described in chapter 7, namely the validation of the GFPE method, the verification of the simplified ray model and the definition of the transition region. The GFPE code was tested in three distinct atmospheric conditions and the results obtained from the simulations were consistent with the benchmark data. Using as a reference the validated GFPE results, the ray model was verified using a non-refracting atmosphere, where it should provide the analytical solution of the wave equation. The similarity between the curves obtained with both numerical models allowed us to

confirm the correct implementation of the two methods. The transition region was theoretically introduced in chapter 4. Using the same atmospheric properties from the validation process of the GFPE method, we studied the evolution of the pressure field in reference conditions using both propagation methods and, by observing the differences in all the test cases, we were able to define the boundaries of a transition region that was applicable to all the simulated atmospheric conditions. The hybrid model was tested using the defined merging zone and the results suggested its applicability to aviation noise simulations.

In chapter 8 we discussed the application of the hybrid propagation model to an airport scenario by resorting to realistic flight conditions. At first, we implemented three different trajectories, namely two standard noise abatement procedures for departing flights and one landing path. The results obtained from the approach simulation were compared with published experimental results and the agreement between the numerical values and the experimental data confirmed the adequacy of the program to actual aircraft operations. The departure simulations allowed the visualization of the evolution of several parameters and their relation to the sound pressure time history. Consequently, it was possible to verify that the distance between the aircraft and the receiver as well as the thrust setting are the main driver parameters of the sound levels at the observer. Finally, we simulated a set of five noise reduction techniques for takeoffs that are typically used by airlines. The results obtained with these trajectories indicated that noise abatement procedures should be chosen according to the region where sound levels are to be minimized. Therefore, for receivers closer to the airport, thrust reduction should be accomplished before reaching the observer, while for regions far from the runway the initial climb segment, which is characterized by a steeper climb gradient, should be extended to allow the maximization of the distance between the aircraft and the observer.

Despite the results obtained with the model proposed in this dissertation, it should be kept in mind that multiple simplifications were considered. To achieve a more realistic description of the environment in the vicinity of airports, future developments should include more complex models considering atmospheric turbulence as well as a more realistic definition of the ground surface simulating noise barriers, topographic features and different ground materials representing normalized impedances discontinuities. Additionally, aircraft dynamics may be included in the program to allow the implementation of optimization tools as a means of obtaining a realistic flight path with minimum noise impact.

## 10 References

- Airbus - Flight Operations Support & Line Assistance (2003). *Getting to Grips with Aircraft Noise*, Airbus.
- Attenborough, K. (1985). "Acoustical impedance models for outdoor ground surfaces," *J. Sound Vib.*, **99**, 521–544.
- Attenborough, K., Taherzadeh, S., Bass, H. E., Di, X., Raspet, R., Becker, G. R., Gudesen, A., et al. (1995). "Benchmark cases for outdoor sound propagation models," *J. Acoust. Soc. Am.*, **97**, 173–191.
- Boeker, E., and Rosenbaum, J. E. (2012). "Intelligent switching between different noise propagation algorithms : analysis and sensitivity," INTERNOISE 2012,.
- Butikofer, R. (2006). *IMAGINE -Default aircraft source description and methods to assess source data*, IMAGINE project.
- Cooper, J. L., and Swanson, D. C. (2007). "Parameter selection in the Green's function parabolic equation," *Appl. Acoust.*, **68**, 390–402.
- Correia, G. S. D. (2011). *Previsão de níveis de ruído aeronáutico na vizinhança do Aeroporto de Lisboa*, M. Sc. Thesis, Instituto Superior Técnico.
- Delany, M. E., and Bazley, E. N. (1970). "Acoustical properties of fibrous absorbant materials," *Appl. Acoust.*, **3**, 105–116.
- Dinapoli, F. ., and Deavenport, R. L. (1979). "Numerical models of underwater acoustic propagation," *Ocean Acoust.*, **8**, 79–157.
- Embleton, T. F. W., Piercy, P. E., and Daigle, G. A. (1983). "Effective flow resistivity of ground surfaces determined by acoustical measurements," *J. Acoust. Soc. Am.*, **72**, 1239–1244.
- Eurocontrol (2012). *Aircraft Noise and Performance (ANP) database*, Available: <http://www.aircraftnoisemodel.org>. Retrieved from <http://www.aircraftnoisemodel.org>
- European Civil Aviation Conference (2005). *Report on Standard Method of Computing Noise Contours around Civil Airports, Volume 1: Applications Guide*, ECAC.
- European Civil Aviation Conference (2005). *Report on Standard Method of Computing Noise Contours around Civil Airports, Volume 2: Technical Guide*, ECAC.
- Federal Aviation Administration (2008). *INM v7.0 Technical Manual*, FAA.
- Federal Aviation Administration (2014). *Aviation Environmental Design Tool ( AEDT ) 2a - Technical Manual*, FAA.
- Frigo, M., and Johnson, S. G. (1997). *The Fastest Fourier Transform in the West*, Massachusetts Institute of Technology.
- Gilbert, K. E. (1989). "Application of the parabolic equation to sound propagation in a refracting atmosphere," *J. Acoust. Soc. Am.*, **85**, 630.

- Gilbert, K. E., and Di, X. (1993). "A fast Green's function method for one-way sound propagation in the atmosphere," *J. Acoust. Soc. Am.*, **94**, 2343–2352.
- International Civil Aviation Organization (2005). *Annex 16 to the convention on international civil aviation: Environmental Protection, Volume I: Aircraft Noise*, ICAO.
- International Civil Aviation Organization (2007). *Environmental technical manual - procedures in the noise certification of aircraft*, ICAO, Vol. I.
- International Civil Aviation Organization (2007). *Review of noise abatement procedure research & development and implementation results*, ICAO.
- International Civil Aviation Organization (2008). *Guidance on the Balanced Approach to Aircraft Noise Management*, ICAO.
- International Civil Aviation Organization (2010). *Environmental Report 2010*, ICAO.
- International Civil Aviation Organization (2013). *Environmental Report 2013*, ICAO.
- Jensen, F. B., Kuperman, W. A., Porter, M. B., and Schmidt, H. (1994). *Computational Ocean Acoustics*, American Institute of Physics.
- Lee, S. W., Bong, N., Richards, W. F., and Raspet, R. (1986). "Impedance formulation of the fast field program for acoustic wave propagation in the atmosphere," *J. Acoust. Soc. Am.*, **79**, 628–634.
- Mcaninch, G. L., and Shepherd, K. P. (2011). "On INM 's Use of Corrected Net Thrust for the Prediction of Jet Aircraft Noise," FAA,.
- Oliveira, A. F. G. P. de (2012). *The effect of wind and turbulence on sound propagation in the atmosphere*, M. Sc. Thesis, Instituto Superior Técnico.
- Ollerhead, J. B. (1992). *DORA Report 9120 The CAA Aircraft Noise Contour Model : ANCON Version 1*, Aviation, CAA.
- Ollerhead, J. B., Rhodes, D. P., Viinikainen, M. S., Monkman, D. J., and Woodley, A. C. (1999). *The UK Civil Aircraft Noise Contour Model ANCON : Improvements in Version 2 (R & D REPORT 9842)*, CAA.
- Oppenheim, A. V., Schafer, R. W., and Buck, J. R. (1998). *Discrete-Time Signal Processing*, Prentice Hall, 2nd ed.
- De Roo, F., Salomons, E. M., Heimann, D., and Hullah, P. (2007). *IMAGINE -Reference and Engineering Models for Aircraft Noise Sources, Volume 1*, IMAGINE project.
- Rosenbaum, J. E. (2011). *Enhanced Propagation Modeling of Directional Aviation Noise: A Hybrid Parabolic Equation-Fast Field Program Method*, Ph.D. Thesis, The Pennsylvania State University.
- Rosenbaum, J. E., and Boeker, E. (2014). "Enhanced propagation of aviation noise in complex environments : A hybrid approach," *Int. J. Aeroacoustics*, **13**, 463–476.
- Rosenbaum, J. E., Boeker, E., Buer, A., Gerbi, P. J., Lee, C. S. Y., Roof, C. J., and Fleming, G. G. (2012). *Assessment of the Hybrid Propagation Model - Volume 1: Analysis of Noise Propagation Effects*, FAA.

Rosenbaum, J. E., Boeker, E., Buer, A., Gerbi, P. J., Lee, C. S. Y., Roof, C. J., and Fleming, G. G. (2012). *Assessment of the Hybrid Propagation Model - Volume 2: Comparison with the Integrated Noise Model*, FAA.

Salomons, E. M. (1998). "Improved Green's function parabolic equation method for Atmospheric Sound Propagation," *J. Acoust. Soc. Am.*, **104**, 100–111.

Salomons, E. M. (2001). *Computational Atmospheric Acoustics*, Kluwer Academic Publishers.

Society of Automotive Engineers (2006). *SAE Aerospace Information Report*, "AIR 5662: Method for Predicting Lateral Attenuation of Airplane Noise," SAE International.

West, M., Gilbert, K., and Sack, R. A. (1992). "A Tutorial on the Parabolic Equation (PE) Model Used for Long Range Sound Propagation in the Atmosphere," *Appl. Acoust.*, **37**, 31–49.

Zwikker, C., and Kosten, C. W. (1949). *Sound Absorbing Materials*, Elsevier Pub. Co.



## A. Benchmark case studies results

In this section we present the benchmark figures published by Attenborough (1995) and that are related to the test cases studied in chapter 7.

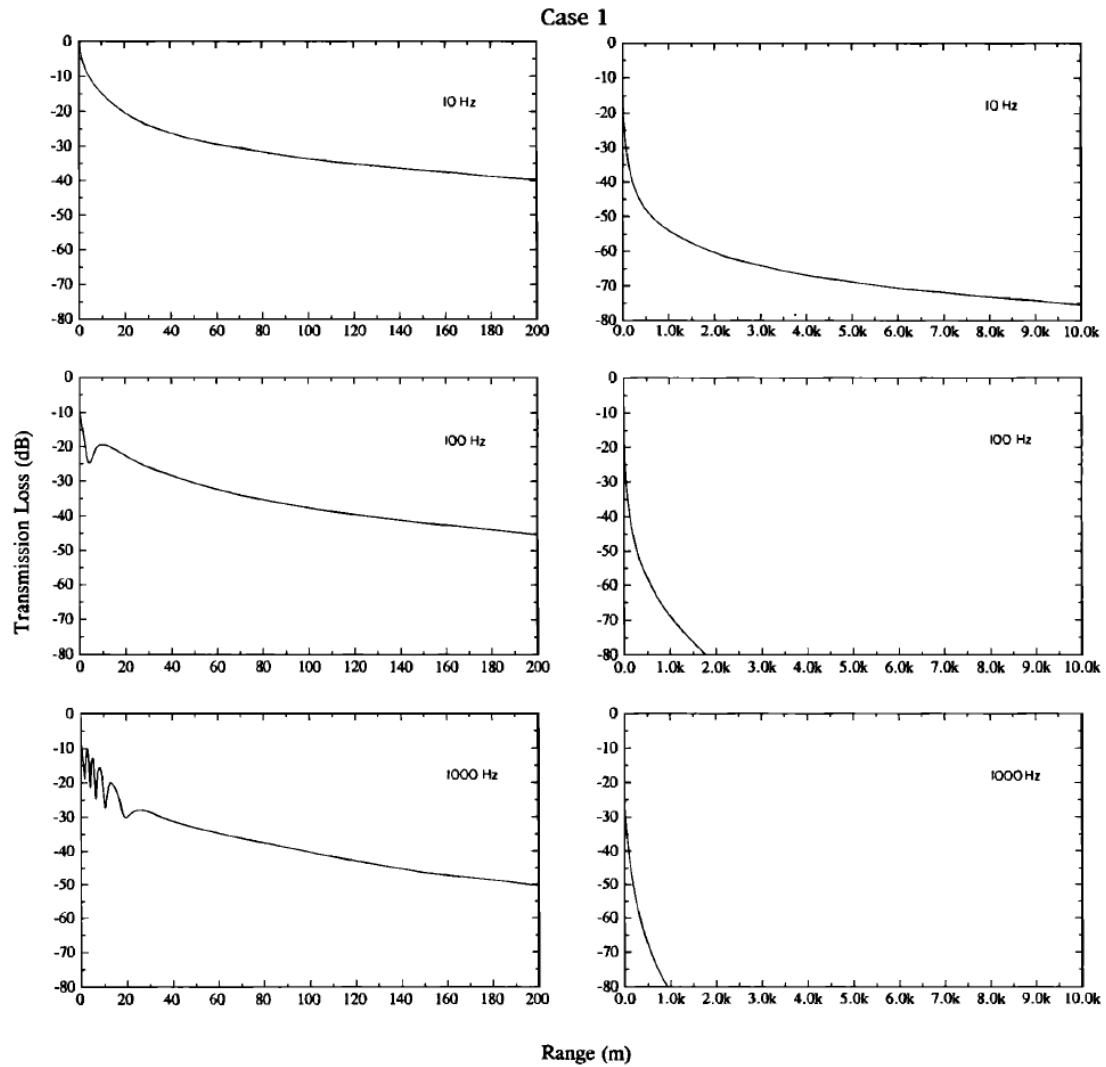


Figure A.1 - Transmission loss up to 200 m (left figures) and up to 2 km with parameters from test case 1 (Attenborough et al., 1995).

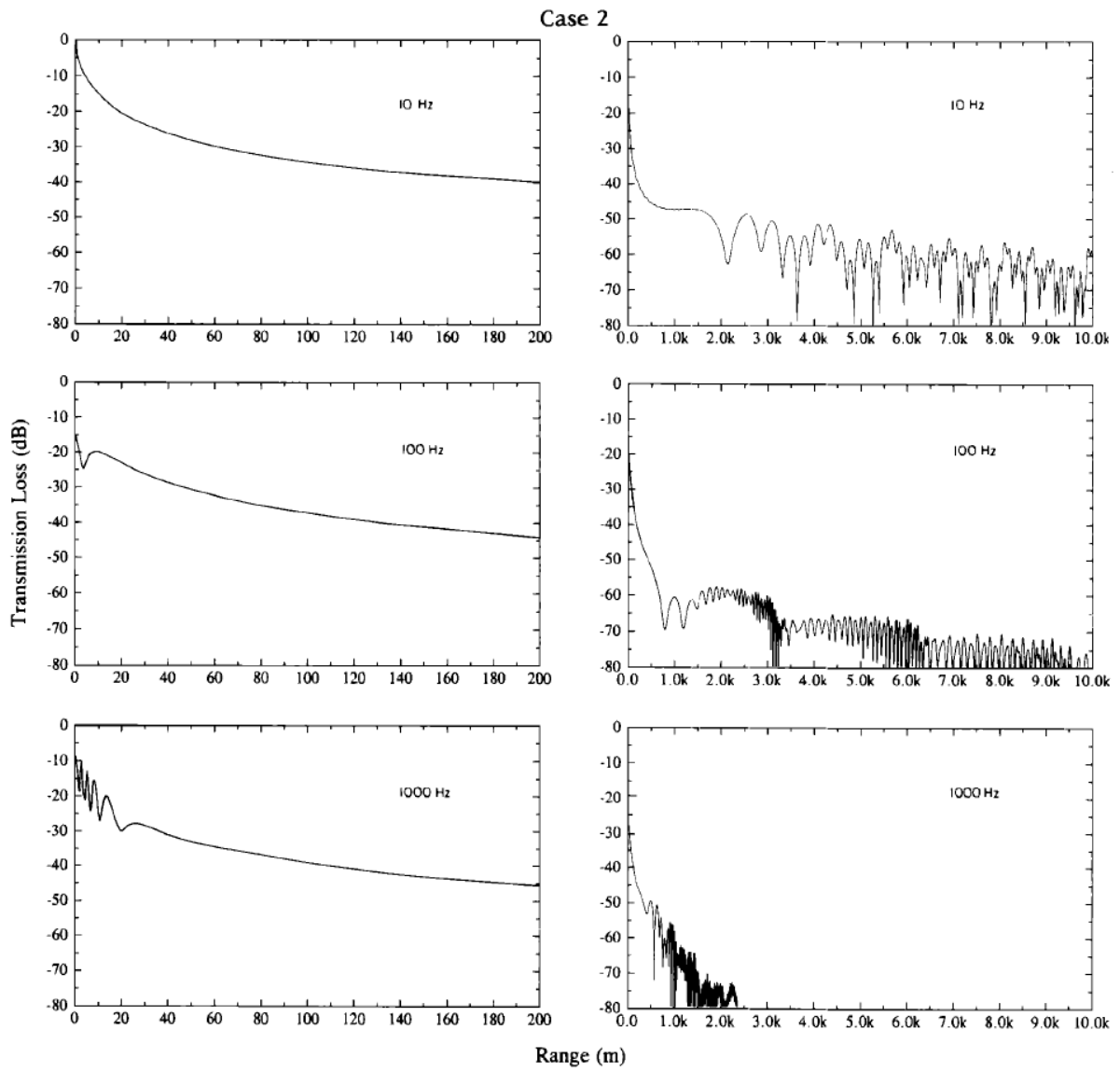


Figure A.2 - Transmission loss up to 200 m (left figures) and up to 2 km with parameters from test case 2 (Attenborough et al., 1995).

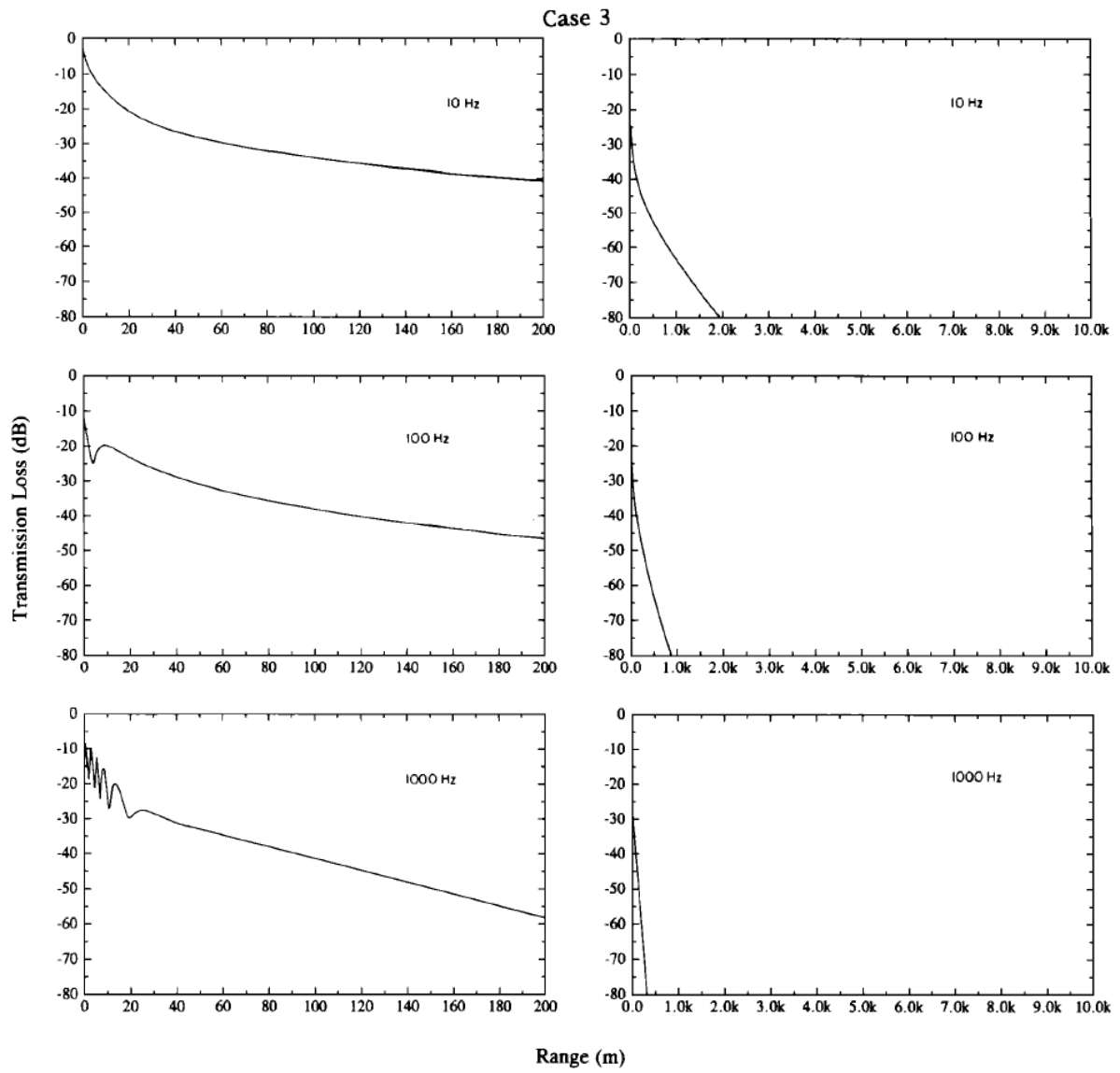


Figure A.3 - Transmission loss up to 200 m (left figures) and up to 2 km with parameters from test case 3 (Attenborough et al., 1995).



## B. Position of the receivers for the airport case studies

In this section we present the locations for each of the receivers used in the simulations of the airport scenarios discussed in chapter 8.

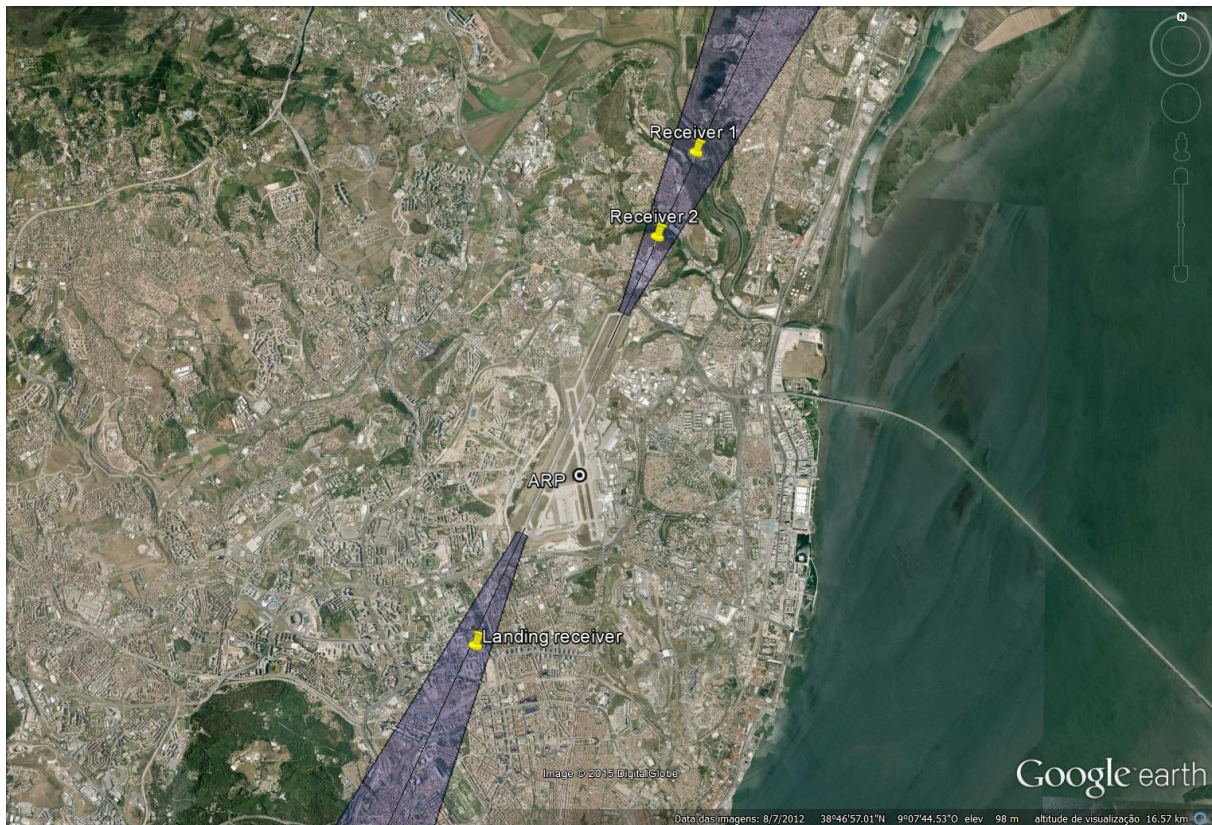


Figure B.1 - Position of the receivers for the airport simulations.

Google Earth. July 8<sup>th</sup>, 2012. April 29<sup>th</sup> 2015.

Table B.1 - Geographic (GPS) positions of the receivers for the airport simulation.

	Latitude	Longitude	Altitude (AGL)
Landing Receiver	38°44'54.00"N	9° 9'9.00"W	1.2 m
Receiver 1	38°49'10.00"N	9° 6'56.00"W	1.2 m
Receiver 2	38°48'24.98"N	9° 7'19.99"W	1.2 m